ABSTRACT

Title of Document: MODEL DEVELOPMENT FOR GADOLINIA-DOPED CERIA-BASED ANODES IN SOLID OXIDE FUEL CELLS

Lei Wang, Doctor of Philosophy, 2014

Directed By: Professor Gregory S. Jackson,
Department of Mechanical Engineering

Intermediate temperature (500 - 700 °C) solid oxide fuel cells (IT-SOFCs) with gadolinia-doped ceria (GDC) electrolytes have significant commercial potential due to reduced materials costs for seals and interconnect and improved performance with high oxide-ion conductivity at these temperatures. As an SOFC anode component in the reducing anode environments, GDC offers enhanced catalytic activity and tends to suppress carbon deposition in composite Ni/GDC anodes. The current study investigates relevant kinetics on GDC anodes for IT-SOFC applications. Simultaneous electrochemical characterization and X-ray photoelectron spectroscopy of thin-film Ni/GDC and Au/GDC electrochemical cells provide a basis for understanding pathways for H_2 and CO electrochemical oxidation as well as H_2O splitting on GDC and GDC composite electrodes. Differences in electrochemical performance of Ni/GDC and Au/GDC electrodes at temperatures below 650 °C reveal

limitations of GDC surfaces in promoting electrooxidation under conditions of low polaron (electron) mobility. These results also suggest the role of the metal in promoting hydrogen spillover to facilitate change transfer reactions at the Ni/GDC interface. Variation in OH^- concentration at the metal/GDC interface with operating temperature, effective oxygen partial pressure, and electric bias provides valuable insight into the nature of electrochemical and other heterogeneous reactions in IT-SOFC anodes.

A detailed kinetic model for the GDC surface reactions and Ni/GDC charge-transfer reactions of H_2 oxidation and H_2O electrolysis is developed based on electrochemical characterization and spectroscopic analysis of GDC surface electrochemistry. The thermodynamically consistent kinetic model is able to capture the observed chemical and electrochemical processes on the thin-film Ni/GDC electrode. A full three-dimensional IT-SOFC stack model is developed with simplified kinetics to evaluate GDC-based anode performance with H_2 and methane-derived fuels. The stack model explores the effects of operating condition on performance of stacks with GDC electrolytes and Ni/GDC anodes. The parametric study results of stack model provide essential information for optimizing performance of IT-SOFCs stack and guiding IT-SOFC design. Temperature distribution in non-isothermal model result suggests that internal CH_4 reforming can be used as an effective thermal management strategy to maintain high current densities and cell voltages and to lower risk to thermo-mechanical degradation.

MODEL DEVELOPMENT FOR GADOLINIA-DOPED CERIA-BASED ANODES IN SOLID OXDE FUEL CELLS

By

Lei Wang

Dissertation submitted to the Faculty of the Graduate School of the
University of Maryland, College Park, in partial fulfillment
of the requirements for the degree of
Doctor of Philosophy
2014

Advisory Committee:
Dr. Gregory Jackson, Chair
Dr. Bryan Eichhorn
Dr. Teng Li
Dr. Eric Wachsman
Dr. Bao Yang

Dedication

For all my loved ones

Acknowledgements

First of all, I would like to express my deepest gratitude to my advisor Dr. Jackson. I want to thank him for providing me the opportunity to work with him and conduct research, which I am really excited about. He has provided tremendous guidance and support throughout years of my PhD study.

My gratitude also goes to Dr. Bryan Eichhorn, Dr. Teng Li, Dr. Eric Wachsman and Dr. Bao Yang, for all the time and efforts of serving on my dissertation committee.

I am also grateful to Dr. Bryan Blackburn and Dave Buscher of Redox Power Systems, LLC, for the financial support for the last three years of my PhD journey and equipment used in stack experiments. Discussions with Dr. Blackburn gave me great inspirations on stack modeling as well.

Great thanks go to Dr. Chunjuan Zhang, Dr. Yi Yu, and Aaron Geller in Chemistry Department University of Maryland, for the discussions on electrochemical cell fabrication and XPS experiments.

Special thanks go to Dr. Zhi Liu, Dr. Hendrik Bluhm, Dr. Ethan Crumlin, and Baohua Mao at the Advanced Light Source at Lawrence Berkeley National Labs.

I want to thank Dr. Hee Sung Yoon at University of Maryland Energy Research Center (UMERC) for fabricating Redox 10 × 10 cm^2 cells, Dr. Bryan Blackburn (Redox) and Colin Gore (UMERC) for performing SOFC stack experiments.

Thank you to my colleagues in Dr. Jackson's research group: Dr. Steven DeCaluwe, Dr. Atul Bhargav, Dr. Will Gibbons, Dr. Rick Stroman, Siddharth Patel, Jennie Moton, Andy Oles, Jon Angle, and Josh Pearlman.

Many thanks go to Tom Loughran and John Hummel in the Nanocenter's Fablab, and Dr. Wen-An Chiou in the NISP lab at the University of Maryland.

Last but not the least, I want to thank my family for all their love and support. To Chenyu Wang, thank you so much for always being there and supporting me. I owe you so much.

Table of Contents

List of Tables

List of Figures

Chapter 1: Introduction and Background

1.1 Introduction to Solid Oxide Fuel Cells

Solid oxide fuel cells (SOFCs) are electrochemical cells that convert chemical energy of a fuel and oxidant directly into electrical energy with some amount of waste heat produced depending on the operating voltage of the cells. In each cell of an SOFC stack, a solid-state electrolyte membrane conducts oxide ions at elevated temperatures (between 500 °C and 1000 °C) from a cathode to an anode of the cell. Electrochemical oxidation of fuels occurs in the reducing environment of the anode by the incoming oxide ions. The gradient of effective oxygen partial pressure (P_{O2}) across the membrane provides the chemical potential driving force to establish the voltage for each individual cell.

At their operating temperatures, SOFCs use ceramic electrolytes and metal/ceramic (cermet) electrodes that do not require expensive precious metal catalyst used in low-temperature fuel cells. At the high operating temperatures, SOFC anodes can be designed to consume light hydrocarbon fuels directly, in part by internal reforming within the anode [1-3]. However, care must be taken to design and operate the anode in such a way as to avoid the risk of carbon deposition that can cause irreversible cell damage [2].

SOFCs have potentials for a wide variety of applications with output from 100 W devices from auxiliary power units in vehicles to several MW stationary power

generation [4, 5]. SOFCs can operate with higher efficiency and with less pollutant emissions than more conventional hydrocarbon-fueled power systems [6]. SOFCs are suitable for combined heat and power (CHP) applications, where the excess high-quality waste heat of the fuel cell is used for a heat-driven process. These inherent characteristics of SOFCs make them uniquely suitable to address concerns about environment and climate change that are associated with fossil fuel based electric power generation.

1.1.1 Working Principles of SOFCs

A single cell in a SOFC is often referred to as a membrane electrode assembly (MEA). The MEA consists of a cathode, electrolyte, and anode as shown in Figure 1.1. To minimize resistance (and voltage loss) associated with oxide-ion transport across the dense electrolyte, practical cells for high power density typically have electrolyte thicknesses well below 50 μm, and such thin layers require some sort of structural support. In most SOFC MEAs for practical devices, this support is provided by the anode, which is split between a functional layer where the electrochemical reactions occur and a porous anode support layer as shown in Figure 1.1. For planar SOFC systems (which will be the focus of this work), each MEA is sandwiched between two cell interconnects for current collection. The cell interconnects are designed to provide flow channels for feeding oxygen to the cathode and feeding fuels to and removing oxidation products from the anode. Tens or hundreds of such cells can be connected in series to form the SOFC stack that delivers desired DC electrical power at adequately high voltages for useful energy conversion.

Figure 1.1 also illustrates the chemical and electrochemical processes within an SOFC using methane (CH_4). During SOFC operation with CH_4, internal reforming (R.1.1) produces H_2 and CO in the anode support layer.

$$CH_4 + H_2O = 3H_2 + CO \qquad \text{(R.1.1)}$$

The CO can be converted into H_2 by further water-gas shift (WGS) reaction (R.1.2) in the support layer to form H_2, which is favorably oxidized in the anode functional layer [7].

$$CO + H_2O = H_2 + CO_2 \qquad \text{(R.1.2)}$$

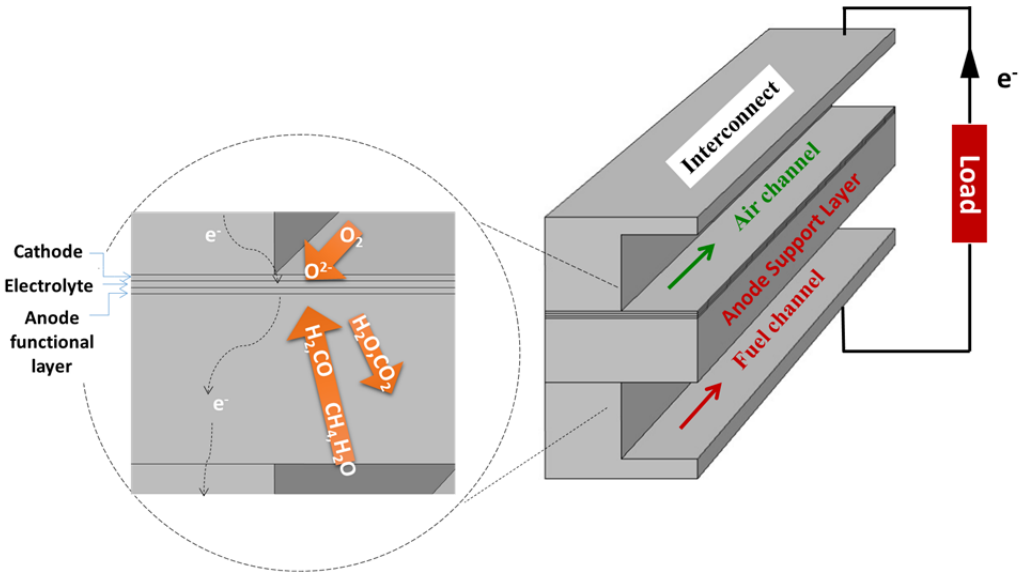

Figure 1.1. Schematic representation of fluid, chemical, and electrochemical processes in a planar SOFC section.

H_2 and CO diffuse to the anode functional layer and can react electrochemically with oxide ions (O^{2-}) diffusing across the electrolyte from the

cathode, but H_2 oxidation dominates charge-transfer reaction in SOFC anodes [8, 9] given by the global half-cell reaction in R.1.3

$$H_{2(g),a} + O^{2-}_{elec} = H_2O_{(g),a} + 2e^-_a \quad \text{(R.1.3)}$$

and CO can be directly oxidized through reaction R.1.4

$$CO_{(g),a} + O^{2-}_{elec} = CO_{2(g),a} + 2e^-_a \quad \text{(R.1.4)}$$

On the cathode side, separated from the anode by the electrolyte, O_2 reduction consumes electrons as shown in R.1.5.

$$\frac{1}{2}O_{2(g),c} + 2e^-_c = O^{2-}_{elec} \quad \text{(R.1.5)}$$

The resulting electrons produced in the anode from R.1.3 and R.1.4 and consumed in the cathode by R.1.5 deliver electrical power to an external electric circuit.

The difference in oxygen chemical potential across the electrolyte provides a driving force for the transport of oxide ions across the electrolyte membrane. The driving force is opposed by an electrical potential, which under ideal open circuit conditions is the reversible Nernst potential or theoretical open circuit voltage (OCV or $V_{ocv,th}$) expressed as follow

$$V_{OCV,th} = \frac{\bar{R}T}{4F}\ln\left(\frac{P_{O2,c}}{P_{O2,a}}\right) \quad \text{(Eq. 1.1)}$$

where $P_{O2,a}$ is effective oxygen partial pressure on the anode determined by equilibrium calculations of the reducing gas environments. $P_{O2,a}$ of a typical SOFC anode environment with H_2 and slight amount of H_2O is calculated as follow

$$P_{\mathrm{O2,a}} = \exp\left(\frac{\Delta G^0}{\bar{R}T}\right) * \left(\frac{P_{\mathrm{H2O}}}{P_{\mathrm{H2}}}\right)^2 \quad \text{(Eq. 1.2)}$$

where ΔG^0 is the free energy change for the global H_2 oxidation.

With an external load, the chemical driving force transports charged species against the electric potential gradient, and thus electrical work is extracted as electrons flow through an external circuit. The operating voltage (V_{cell}) of a fuel cell at an external current density (i) is expressed as

$$V_{\mathrm{cell}} = V_{\mathrm{OCV,th}} - \sum \eta_{\mathrm{act}} - \sum \eta_{\mathrm{Ohm}} - \sum \eta_{\mathrm{conc}} \quad \text{(Eq. 1.3)}$$

where η_{Ohm} is Ohmic loss due to electrical resistance, η_{conc} is concentration losses due to drop of reactant concentration, and η_{act} is potential difference from equilibrium to drive the charge-transfer reaction. By summing these various overpotentials (η), each of which is functions of i, the operating cell voltage is determined.

1.1.2 Conventional SOFCs

Conventional SOFCs typically operate between 750 °C and 1000 °C. The most common SOFC MEAs consists of an yttria-stabilized zirconia (YSZ) electrolyte, which offers sufficient ionic conductivity (> 0.01 S/cm) at these temperatures. The dense electrolyte membrane is stable in both reducing and oxidizing environments, and does not permit any significant electronic conductivity that would reduce cell voltages. Furthermore, well-defined sintering processes have been established such

that fully dense YSZ electrolytes can be fabricated to eliminate leakage of gaseous reactants between the two electrodes [3, 10].

In conventional SOFCs, nickel (Ni)/YSZ cermets can provide high catalytic activity for fuel oxidation in the anode. Ni/YSZ composites can also be tailored to alleviate mismatches in the coefficient of thermal expansion (CTE) between the anode and the YSZ electrolyte [11]. The composite electrode has significant porosity allowing gas transport to anode functional layer at the electrolyte interface to facilitate charge-transfer reactions. A thicker anode support layer (several hundreds of μm) with larger pores generally serves as the physical support of the SOFC and can be designed to promote internal steam reforming (R.1.1) and WGS (R.1.2) [12].

On the other side of the electrolyte membrane, perovskite-based cathode electrocatalysts are coated in thin layers to promote O_2 dissociative adsorption and oxide ion incorporation into the bulk. For conventional SOFCs, strontium-doped lanthanum manganite ($La_{1-x}Sr_xMnO_3$ or LSM) is the most common material for high temperature SOFC cathodes because of its compatibility with YSZ electrolyte. The porous LSM/YSZ composite cathode provides oxide ion mobility complementary to the electronic conductivity, and also adequate reactivity to facilitate oxygen reduction [13, 14].

To achieve reasonable power densities (1 W/cm^2), conventional SOFCs with YSZ electrolytes usually operate at 800 °C or higher temperatures for adequate ionic

conductivity [2, 15]. Such high operation temperatures result in long start-up time, thermo-mechanical stresses, and interphase reactions with seals and interconnects [12]. Moreover, a major disadvantage of the Ni/YSZ cermet anode is the propensity of Ni to crack hydrocarbon resulting in deleterious carbon deposition when using hydrocarbon fuels [12, 16]. The LSM cathode often faces chromium (Cr)-poisoning from common high-temperature alloys used for interconnects necessary at these temperatures. Cr-poisoning at the cathode degrades the electrode performance under polarization [17].

1.1.3 Intermediate Temperature SOFCs

In recent years, significant efforts have been taken to lower the SOFC operation temperatures to intermediate temperature ranges (between 500 °C and 650 °C). Operating SOFCs with comparable power densities but lower temperatures considerably increases SOFCs' applicability and cost competitiveness by reducing the costs of seals and interconnect materials. Lowering SOFCs operation temperatures can reduce system balance of plant (BOP) costs and allows faster start-up that can implement SOFCs in mobile application. In addition, lower temperatures increase SOFC systems durability by reducing thermal cycling and performance degradation problems [15].

Operating SOFCs at lower temperatures presents challenges for high performance intermediate temperature SOFCs (IT-SOFCs). One such challenge is to reduce area specific resistance (ASR) of the electrolyte without compromising

mechanical strength and gaseous impermeability. Thin-film deposition techniques may be used to fabricate thinner electrolyte to achieve relative lower ASR at lower temperatures [18], but detrimental reaction between the YSZ electrolyte and common low-temperature cathode materials during processing have been observed [19]. Thus, alternative electrolyte material with higher ionic conductivity is essential to bring down the operation temperature.

Another challenge is that polarization losses of electrodes increase at lower temperature, especially at cathode. Reduction of oxygen, incorporation and transport oxide ion to the electrolyte in the conventional LSM/YSZ cathode are much slower at these low temperatures [20]. Therefore, alternative electrodes materials with sufficiently fast kinetics are also needed.

To respond to these challenges, researchers have been implementing high conductivity electrolyte materials such as doped ceria for IT-SOFCs. Among them the most extensively studied is GDC electrolyte [21-24], which shows appreciable ionic conductivity. Figure 1.2 compares ionic conductivity of conventional YSZ electrolyte with gadolinia-doped ceria (i.e., $Ce_{0.9}Gd_{0.1}O_{1.95}$ or GDC) as a function of temperature. It is clear from the plots that GDC has the same ionic conductivity as YSZ while the temperature is brought down 200°C. For example, GDC electrolyte can achieve required ASR (0.15 Ωcm^2 for 15-μm electrolyte) at a temperature of ~500 °C, which YSZ electrolytes with the same thickness can only attain above 700 °C [22]. Other ceria-based electrolytes, such as ceria zirconia oxide, and Sm-, Y-, or Nd-doped ceria,

have also been studied as electrolytes for IT-SOFC development [25-27].

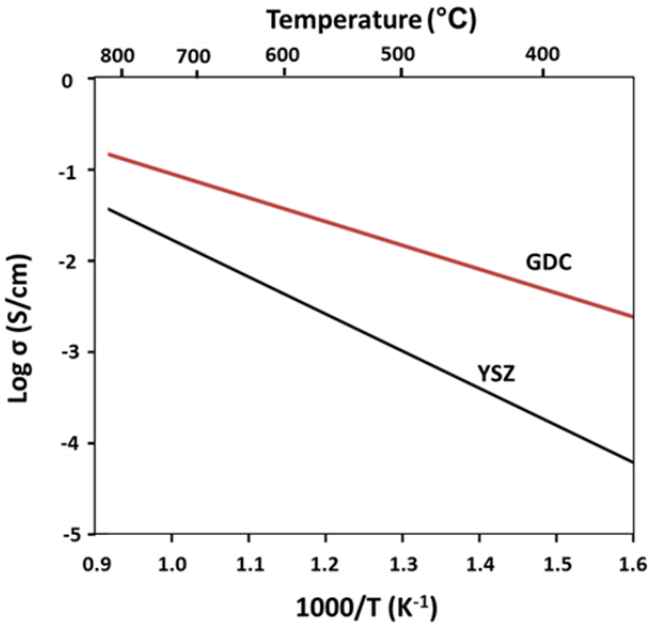

Figure 1.2. Ionic conductivity versus temperature of GDC and YSZ electrolytes.

At reducing environments ($P_{O2} < 10^{-20}$ bar) and temperatures greater than 600 °C, increased electronic conductivity of doped ceria results in internal leakage currents in the electrolyte membranes, which lowers OCV and thus the overall SOFC efficiency [2, 15, 20]. Because of this, GDC-based bi-layer electrolytes, such as GDC/YSZ and erbia-stabilized bismuth oxide (ESB)/GDC, have been studied to utilize high ionic conductivity without significantly sacrificing OCV [28-31].

For IT-SOFCs with ceria-based electrolytes, anodes incorporate metal and ceria-based composite materials. For GDC-based cells, porous Ni/GDC anodes are used which have good activity for H_2 oxidation below 650 °C. Moreover, the GDC is

more resistant to carbon deposition allowing using hydrocarbon on Ni/GDC anodes [12, 32-34]. Copper/ceria composite anode has also been explored since it does not significantly catalyze the carbon formation reaction, while maintaining electronic conductivity and electro-oxidation catalytic activity [35, 36].

For IT-SOFC cathodes, alternative perovskites to LSM have been identified which provide improved O_2 reduction activity, for example, lanthanum strontium cobalt ferrite ($La_xSr_{1-x}CO_yFe_{1-y}O_{3-\delta}$ or LSCF). The LSCF cathode, which has fast ion transport, good oxygen reduction kinetics and acceptable electronic conduction, is high-performance cathode candidate [37-42]. Also the LSCF cathode is chemical compatible with GDC electrolyte [43] and has lower tendency to the Cr-poisoning [17].

1.2 Ceria-based Materials as IT-SOFC Components

Ceria-based materials are attractive for developing IT-SOFCs, especially for electrolyte and anode, because of their relatively high oxygen ion conductivity at intermediate temperatures and their ability to promote catalytic activity for oxidation reactions [44]. At these temperatures, stoichiometry of ceria is perturbed by reversibly adsorbing and desorbing oxygen into the lattice while retains the fluorite lattice, as indicated in R.1.6 according to the Kröger-Vink notation

$$O_O^X + 2Ce_{Ce}^X \leftrightarrow \frac{1}{2}O_{2(g)} + V_O^{\cdot\cdot} + 2Ce'_{Ce} \qquad \text{(R.1.6)}$$

where O_O^X and Ce_{Ce}^X are oxygen on oxygen lattice sites, and cerium on cerium lattice sites respectively. In R.1.6, an oxygen vacancy ($V_O^{\cdot\cdot}$) is created by removing an oxygen atom from the ceria lattice; meanwhile, two negatively charged cerium sites (Ce_{Ce}') form to balance the oxygen vacancy.

1.2.1 Properties of Ceria-based Materials for SOFC Anodes

Ceria (CeO_2) is an excellent catalyst that has been applied in catalytic converters, co-catalyst water-gas shift reactors, steam reformers, and Fischer-Tropsch reactions [44]. In reducing environments, ceria can give up some oxygen to form oxide vacancies, which enhances oxide-ion conductivity. As the number of vacancy increases, the ease at which oxygen can move around in the crystal increases, facilitating reducing and oxidizing molecules or co-catalyzing on its surface.

At IT-SOFC anode environments, ceria exhibits mixed ionic and electronic conductivities (MIEC). Upon reduction of ceria, localized electrons (or polarons) can hop through the ceria lattice as an effective means of electronic conductivity, resulting in the MIEC property. Due to such a property, ceria provides an extended active surface area and additional pathways for fuel oxidation reactions, as illustrated in Figure 1.3. For H_2 oxidation, ceria-based anodes can provide either ceria/metal/gas three-phase boundary (ceria represents an ionic conductor) or at the ceria/gas interface (ceria represents both ionic and electronic conductors). This MIEC property enhances electrochemical oxidation [45].

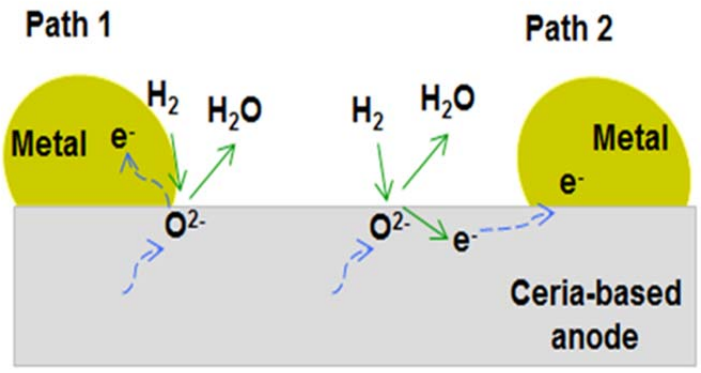

Figure 1.3. Schematic of H_2 electro-oxidation on ceria-based anode. The MIEC behavior extends reaction region distanced from pure electronic conducting metal.

1.2.2 Gadolinia-doped Ceria as IT-SOFC Anodes

Ceria doped with cations of lower valence (ex, Gd^{3+}, Y^{3+}, Sm^{3+}, and Ca^{2+}), are known to be good electrolyte candidates for IT-SOFCs. The dopant introduces extra vacancies, as exemplified by Gd_2O_3 in R.1.7.

$$Gd_2O_3 \leftrightarrow 2Gd'_{Ce} + V_O^{\cdot\cdot} + 3O_O^X \qquad \text{(R.1.7)}$$

Among doped-ceria materials, GDC has been primarily studied due to its much higher ionic conductivity [15, 22] and better chemical compatibility with high-activity cathode electrocatalysts like LSCF used in IT-SOFCs [46]. As such, GDC is attractive as potential electrolyte application in IT-SOFCs [20, 22]. In relatively high P_{O2}, the electrical conductivity is predominantly ionic, and thus the total conductivity is independent of P_{O2} [47].

In anode environments, GDC, similar to undoped-ceria, exhibits MIEC property due to redox cycling of the cerium cations (R.1.6). Reduction of ceria increases at lower P_{O2} (< 10^{-20} bar), which leads to comparable or even greater electronic conductivity to the ionic conductivity. Electronic conductivity dominates total conductivity and leads to a $P_{O2}^{-1/4}$ dependency of conductivity, as illustrated in Figure 1.4. Such MIEC behavior of GDC anode, enhances catalytic activity that impregnation of GDC particles significantly reduced the electrode interface resistance and polarization potential [48].

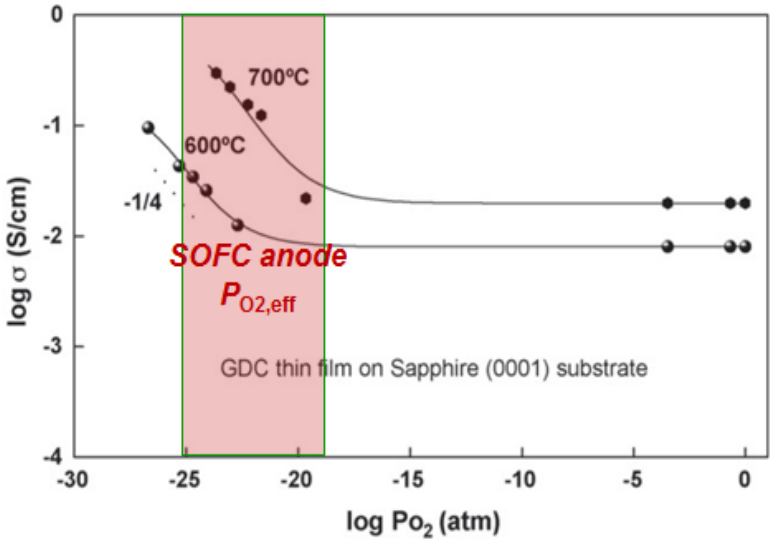

Figure 1.4. Electrical conductivity of thin-film GDC as function of oxygen partial pressure of at 600 °C and 700 °C [47].

GDC anodes have been demonstrated stable though rapid thermal and redox cycling under hydrocarbons [49]. Researchers have reported that an SOFC with a Ni/GDC anode directly operates on methane at 600 °C without carbon deposits [50].

A GDC-based SOFC has been shown to operate stably JP5 model reformate for 500 hours without degradation or carbon deposition [51].

1.2.3 Previous Test Studies for Understanding GDC Electrode Kinetics

Despite the fact that GDC is suitable as an IT-SOFC anode and its bulk transport properties are well characterized, knowledge of the surface kinetics for reactions relevant for SOFC anodes remains limited. Ionic and electronic transport properties of GDC as a function of temperature and P_{O2} has been measured many times as illustrated for one study in Figure 1.4, and such studies have established fundamental thermodynamics of GDC non-stoichiometry for both 10% Gd-doping and 20% Gd-doping [52-56]. Yet, information on how the non-stoichiometry as well as ion and electron transports impact surface reactions and fuel oxidation are limited to a few studies on the impacts of surface area on vacancy formation [55].

Recent experimental studies focused on understanding catalytic activity of GDC anode on H_2 oxidation and its interaction with carbon-based species. Electrochemical impedance measurements of H_2 oxidation indicate that impregnation of GDC particles significantly reduces the electrode interface resistance and polarization potential [48]. An impedance study of CO/CO_2 exchange reaction on GDC derived kinetic parameters such surface exchange rate coefficient and vacancy diffusion coefficient [57]. Past studies have indicated GDC electrodes have low activity for C-H bond cracking and capability to remove deposited carbon species by the lattice oxygen [58, 59]. However, many questions remain about how

carbonaceous species react on GDC-based electrodes and further how fuel species are oxidized on metal/GDC and in particular Ni/GDC cermet structures.

Better understanding of GDC electrodes kinetics will benefit from probing the GDC surface and GDC/Ni interface *in operando* during fuel oxidation. Recent progresses in ambient-pressure X-ray photoelectron spectroscopy (AP-XPS) enable extracting critical surface composition during reactions. Initial investigations of oxidation state of ceria-based fuel electrode have been taken under a variety of conditions at elevated temperatures relevant for IT-SOFCs [60-62]. These studies have shown that the catalytic activity of ceria is related to the number of oxygen deficiency in the crystal. Surface chemistry analysis of solid oxide electrochemical cells on H_2/H_2O and CO/CO_2 reaction provides an effective means to study possible reaction pathways for H_2 and/or CO oxidation [63, 64]. Another strong capability of the AP-XPS is to obtain a map of electrical potentials of the components surfaces and interfaces. Such surface/interfacial potentials mapping, directly related to the reactions, is an essential tool to derive detailed interfacial kinetics parameters of electrochemical systems.

1.3 Models of Electrochemistry in GDC-based Anodes

Even though AP-XPS experiments provide information of surface species and overpotentials associated with reactions on the MIEC electrodes, direct observation of interactions between gaseous reactants and electrode surface, as well as the charge-transfer associated with the reactions is impossible. To complement to the

experimental kinetic studies, modeling efforts are needed, so as to quantitatively simulate processes of small molecules (H_2 and CO) oxidation on GDC-based anodes. Such a model provides an effective means to understand fundamental electrochemistry of GDC-based anodes.

Detailed surface chemistry and electrochemistry of the GDC-based electrodes would provide a valuable tool for developing models with adequate functionality to optimize SOFC anode microstructures. Previous studies of H_2/H_2O reaction kinetics on Pt/YSZ interface and H_2 charge-transfer reaction mechanisms for Ni/YSZ anodes provide basic methodology for showing how such models can be used [65, 66]. However, non-Faradaic surface chemistry and charge transport on/in GDC anodes are different from those of YSZ. Reaction pathways of Ni/GDC anode are complicated by the fact that charge-transfer reactions can occur in the vicinity of the three-phase Ni/GDC/gas boundary (TPB) as well as at the GDC/gas interface. A study of H_2 oxidation reaction on doped-ceria catalyst has stated that the reaction is dominated by electrocatalysis at the oxide/gas interface with minimal contributions from the oxide/metal/gas TPB [67]. This raises questions about the role of Ni/GDC heterogeneous electrochemistry, especially when electronic conductivity of GDC decreases at lower temperatures.

Studying of Ni/GDC anode reaction kinetics requires a consistent thermodynamic basis where all relevant surface and bulk-phase species have well-defined enthalpies and entropies in order to determine the equilibrium constant used

in the rate expression from species thermodynamics. The partial free energy of formation associated with redox reaction (R.1.6) of GDC and undoped ceria has been experimentally studied and formulated

$$\Delta\bar{G}_f = \Delta\bar{H}_f - T\Delta\bar{S}_f = -\bar{R}T\ln P_{O2} \quad \text{(Eq. 1.4)}$$

where $\Delta\bar{G}_f$, $\Delta\bar{H}_f$ and $\Delta\bar{S}_f$ are Gibbs free energy, enthalpy and entropy of defect formation reaction, respectively [52, 68].

Non-ideal thermodynamics have been observed on the GDC surface. Strong compositional dependencies of thermodynamic properties arise under IT-SOFC anode conditions, and properties differ between the bulk and the surface [55, 62]. Surface reduction of ceria is significantly greater than the bulk phase at the same conditions. Furthermore, upon significant reduction of Ce^{4+} to Ce^{3+}, formation of defect complexes results in strong interaction potentials that require non-ideal thermodynamics, which complicates reversible kinetic models. Excess Gibbs free energy due to the non-ideal interactions of defects is needed to modify forward and reverse reaction rate coefficients in the mass-action kinetics rate expression [69].

1.4 Models for GDC-based SOFC Stacks

Development of a kinetic model for fuel oxidation on Ni/GDC anodes is of interest because it can be implemented in IT-SOFC stack modeling. The stack model can be calibrated with laboratory-scale SOFC studies and then be used to predict performance of larger SOFC stacks for system design and control. Most of stack

models are based on computational fluid dynamics (CFD) approaches [70-72]. The CFD approach couples electrochemistry with physical transport processes in SOFCs in three-dimensions for unit cells.

Many continuum models use electrochemistry described via a global kinetic Butler–Volmer expression for the electrode/electrolyte interfaces. In such a model, the complicated electrode structures are described as continuum using effective structural, transport, electrical and electrochemical properties [73]. However, overall performance of an SOFC stack largely relies on local conditions such as temperatures and reactant concentrations, which are not uniformly distributed in spaced stack [8]. To this end, two-dimensional and three-dimensional (3-D) models are able to resolve the porous electrode structure, and allow a more detailed correlation of local conditions with electrochemical properties [74-76].

Before this study, stack modeling for GDC-based SOFC have used fitting parameters for the Butler-Volmer expression, which has limited ability to capture complex functionality of the fuel oxidation kinetics as a function of operating conditions [77, 78]. The current study address the limited by functionality of simple oxidation kinetics by developing detailed multi-step Ni/GDC anode kinetics, which can be implemented into the stack-modeling framework. The current study develops a stack model that can be incorporated with an accurate mechanism expression to evaluate and optimize stack performances, as well as to conduct parametric study.

1.5 Objectives and Overview of Current Study

The current study develops a fundamental understanding of the relevant kinetics of GDC-based anodes and establishes a kinetic model to investigate mechanism of H_2 and CO electrochemical oxidation on the GDC. Thermodynamic and kinetic parameters are derived from the experimental studies on the electrochemical oxidation of H_2 and CO on GDC-based electrochemical cells. A 1-D kinetic model is built to validate the proposed mechanism and kinetic parameters. Then, a 3-D stack model is built and implemented with a simplified global mechanism expression to evaluate GDC-based SOFC stack performance and conduct operation optimization. The following chapters describe the experimental and modeling efforts to achieve these objectives:

Chapter 2 presents fabrication process of thin-film GDC electrochemical cells used in the study and subsequent electrochemical characterization. Surface morphology characterization of the GDC electrodes and experiment setup are described. Initial electrochemical characterization results are shown at the end of this chapter.

Chapter 3 discusses using *in operando* ambient pressure X-ray photoelectron spectroscopy to study GDC electrode kinetics under catalytic conditions. Surface species concentrations and interface overpotentials of the GDC electrodes are derived from spectroscopic measurements of reactive GDC surface during H_2/H_2O and CO/CO_2 reactions. Reaction pathways for H_2 and CO electrochemical oxidation at

metal/GDC interface and related surface species are proposed based on the acquired kinetic information.

In Chapter 4, 1-D kinetic modeling based on elementary reactions and thermodynamic properties is developed. The model uses proposed electrochemistry and initial kinetic parameters to simulate thin-film GDC electrode electrochemical cell experimentally studied in Chapter 2 and Chapter 3. The model is further validated against data collected from the experiments. Key thermodynamic and kinetic parameters for H_2 and/or CO electrochemical oxidation on GDC are then derived.

In Chapter 5, a more practical GDC-based three-dimensional IT-SOFC stack model is developed and incorporated with global kinetics of GDC-based electrodes. The stack model is used to evaluate performance of GDC-based IT-SOFCs. Parametric study results on electrolyte thickness and operation conditions are presented in this chapter. The stack model is also used to evaluate stack performance on CH_4 reformate fuel and study effects of internal reforming on the stack.

Chapter 2: Experimental Characterization of Thin-film GDC Electrodes

2.1 Introduction

Better understanding of fundamental processes on the GDC electrode will allow SOFC developers to employ GDC-based materials more effectively in IT-SOFCs. To date, mechanistic understanding of fuel oxidation reactions on the metal/GDC anodes is still unsatisfactory. The complex geometry and limited optical access of practical porous Ni/GDC composite anode structures make it hard to extract quantitative information on surface species and thus limiting processes in the oxidation mechanism. In order to understand the GDC anode kinetics, the current study investigates dense thin-film metal/GDC electrodes because the thin-film geometry provides much cleaner access for surface measurements and minimizes ambiguities associated with uncertain electrode morphology [79].

This chapter explores the electrochemical performances of electrochemical cells with thin-film Ni/GDC and Au/GDC electrodes. The thin-film metal/GDC electrodes confine the electrochemical activity to an optically accessible surface, which simplifies interpretation of the electrochemical data and allow for spectroscopic measurements of electrochemically active surfaces. The cells are electrochemically characterized under different reducing gas environments at temperatures up to 700 °C, characteristic of IT-SOFC anode environments. The results provide a basis for initially probing mechanisms for the oxidation of H_2 and/or

CO on GDC electrodes, which are fully studied using photoelectron spectroscopy for chemical analysis in Chapter 3 and developed using kinetic modeling in Chapter 4. The experimental results presented in this chapter are also employed to validate the kinetic model in Chapter 4.

Impedance and steady-state polarization measurements of GDC porous electrodes suggested that the reaction zone extends through the entire electrode thickness at 800 °C, and the rate-determining process is the surface reaction in the GDC anode [80]. Impedance measurements for CO/CO_2 exchange reactions on GDC electrodes from 700 to 950 °C suggested that nearly entire GDC electrode is electro-catalytically active and the GDC electrode limits kinetic behavior [57]. The MIEC behavior of GDC, in particular, the electronic conductivity, under reducing environments extends the region of electrochemical activity beyond the three-phase boundary regions near the metal/GDC interface. However, the electrochemical activity of the GDC surface may depend strongly on operating conditions and how they impact ionic and/or electronic conductivities. The anode/electrolyte interfacial impedance depends on anode microstructures [81], and gas-phase diffusion significantly contributes to Ni/GDC electrodes impedance [82].

Thin-film electrodes have been demonstrated for the kinetic investigation of electrode materials [60, 63, 83, 84]. Baumann and coworkers utilized thin-film LSCF cathode to study oxygen exchange reaction and use equivalent circuit to interpret impedance measurement. The studies suggested both surface oxygen exchange and

interfacial ion transferring contribute to the impedance [83, 85]. DeCaluwe et al. used thin-film ceria electrodes to characterize surface oxidation states during H_2O electrolysis and H_2 oxidation [60]. This study implied that surface reduction of Ce^{4+} relates to electrochemical performance and oxygen partial pressure (P_{O2}). Using well-defined and geometrically simplified dense thin-film electrode developed by previous scholars is suitable for the purpose of this kinetic study.

In this chapter, fabrication processes of electrochemical cells with thin-film metal/GDC working electrodes deposited on YSZ substrate are described. Surface morphologies of the GDC electrodes are characterized using microscopic techniques. Electrochemical characterization of the working electrodes with Pt/YSZ counter electrodes is taken over a range of compositions for H_2/H_2O, CO/CO_2, and CO/H_2O between 600 °C and 700 °C. Study results show effects of varying temperature and effective P_{O2} on the electrochemical performance in both the fuel oxidation and electrolysis directions for the metal/GDC electrodes. Performance of Ni/GDC and Au/GDC electrodes with the same counter-electrode is compared to identify the synergetic role of the more active Ni (relative to Au) with the partially reduced GDC in composite electrodes for both fuel oxidation and electrolysis.

2.2 Thin-film GDC Electrochemical Cell

Current section describes thin-film GDC electrochemical cells fabrication, surface morphology characterization and experimental setup. The electrochemical cell has deposited GDC thin-film working electrodes on top side of a polycrystalline

YSZ substrate and a much more active counter electrode on the bottom side. Porous metal overlayers of either Ni or Au are deposited on top of the GDC electrodes. Such one-dimensional measurement effectively reduces cross grain boundary resistance and sheet resistance for current collection [86, 87].

2.2.1 Fabrication Procedures

The electrochemical cells are fabricated by sputtering thin-film GDC on a polycrystalline YSZ-supported substrate. Before sputtering, the YSZ substrate is made of 2.8 g of YSZ powder (8% by mole Y_2O_3, purchased from Tosoh) by pressing inside a cylindrical die at 1400 bar, and the resulting pellet is cut into >10 mm × 10 mm square that is approximately 1 mm thick. One side of the YSZ is machined with grooves across the length to provide a location to deposit a porous platinum (Pt) counter electrodes (CE). The grooves are necessary for reactants to access counter electrode in the single-chamber ambient pressure XPS measurements, which relied on a ceramic contact heater on the backside of the cell to control the cell operating temperature. The YSZ substrate is heated to 1450 °C at 1 ºC/min and sintered for 3 hours to form a dense membrane. The final YSZ substrate has 1 mm thickness and 10 mm × 10 mm top-side surface area.

Two 300 nm thick GDC (20% by mole Gd_2O_3, i.e. $Gd_{0.2}Ce_{0.8}O_{1.9}$, target from Kurt J. Lesker) thin-films (2.5 mm × 4.0 mm in area) are radio-frequency (RF) sputtering (Kurt Lesker PVD 75) on the smooth side of the YSZ substrate. RF sputtering is used in this study because of the stability and capability to tune thin-film

property [88-90]. Figure 2.1 shows RF-sputter deposition of GDC on the YSZ substrate. Patterned stainless steel shielding masks (FotoFab) are used to cover the non-coated area when exposed to the sputtering target. The RF power source introduces a bias between the target and substrate held under a low vacuum (15 mTorr). The throw distance (distance between the GDC target and sputtered sample) is set to 65 mm to achieve deposition rate at 5 nm per minute. The resulting thickness is approximately 300 nm after 1 hour sputtering. After sputtering the GDC thin-films, the YSZ substrate with GDC films are heated to 800 °C at 1 ºC/min and sintered for 3 hours to stabilize the GDC film microstructure.

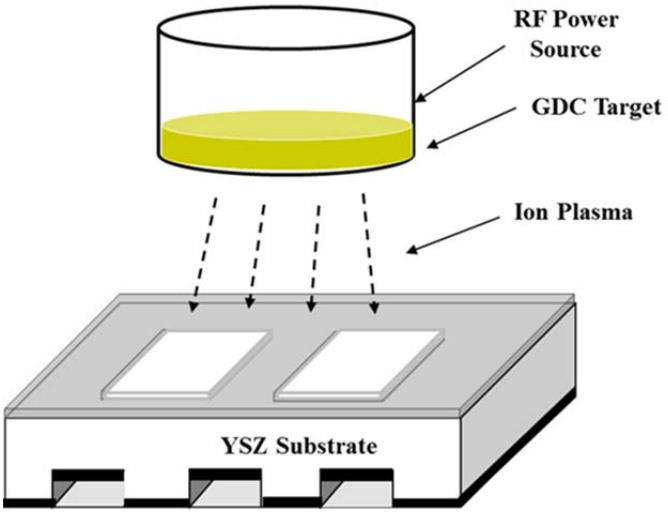

Figure 2.1. Schematic representation of the RF-sputter deposition of GDC on YSZ substrate.

Ni and Au (~300 nm thick) metal overlayers are separately sputter-deposited (AJA International, ATC 1800-V) on each of the two GDC films covered by

patterned shielding masks with a 350-μm border of exposed GDC around the edges. The deposited Ni and Au overlayers are annealed at 750 °C in 5% by volume H_2 (balance Ar) such that the overlayers form interconnected open structures exposing pockets of the GDC surface over the entire area of GDC electrode. The interconnected Ni and Au overlayers serve both as current collectors and as a means for comparison of impact of the metal interactions with the GDC electrochemistry.

Pt (~100 nm thick) is sputter-deposited (AJA International, ATC 1800-V) in the grooves on the backside of the YSZ. The grooves facilitate gas transport to the Pt surface while allowing the cell to maintain good thermal contact with the surface heater in later XPS experiments. A Pt lead wire wrapped with Pt mesh is embedded in the grove attached to the Pt CE and the wire is brought around to top of the YSZ. A Pt mesh connected to the Pt wire for electrical contact is fixed on an Al_2O_3 blocking layer pasted on the top side of the YSZ substrate to facilitate three-probe measurements of ambient pressure XPS endstation. The schematic of the thin-film GDC electrochemical cell is illustrated in Figure 2.2. Images of top and back sides of the cell before wiring are shown in Figure 2.3.

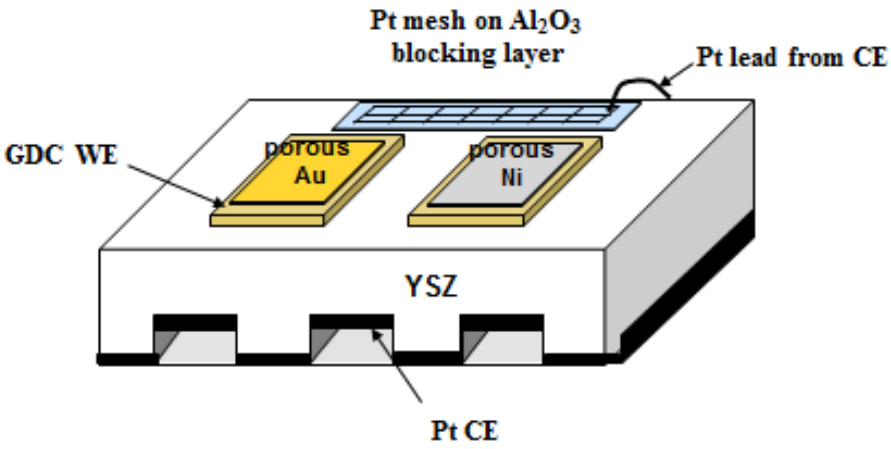

Figure 2.2. Schematic of YSZ-support electrochemical cell with two independent thin-film metal/GDC electrodes and backside Pt counter electrode.

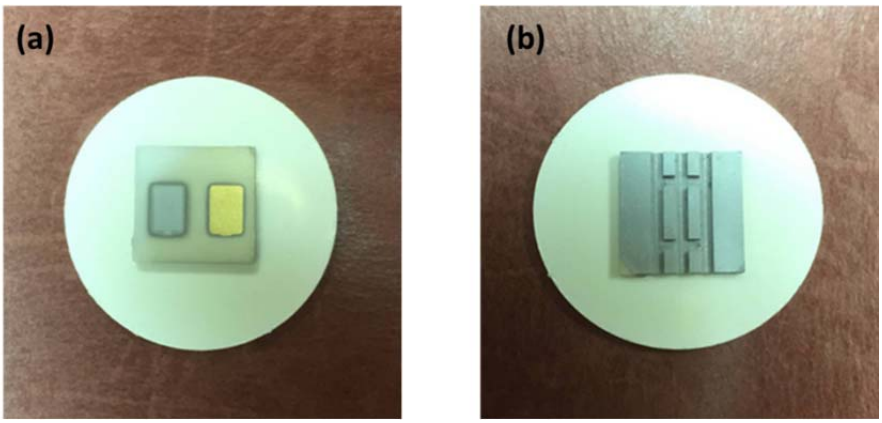

Figure 2.3. Top-side and back-side images of the electrochemical cell held by an YSZ pellet: (a) two symmetric GDC electrode on the YSZ substrate covered by Ni (left) and Au respectively; (b) Pt uniformly distribution on the back-side and in the YSZ grooves.

The electrochemical cell is connected to the potentiostat for electrochemical characterization. Either Ni or Au overlayer is disconnected to the potentiostat while the other is under electrochemical study. In the electrochemical characterization, the cell voltage bias (V_{cell}) is defined as the electrical potential difference between the Pt CE and the connected metal overlayer (Ni or Au), which is grounded ($V_{metal} = 0$). Without any bias, V_{cell} is equal to zero due to equal P_{O2} at both the WE and CE.

Depending on the sign of an applied bias, the GDC WE facilitates either H_2 oxidation or H_2O electrolysis while the opposite reaction occurs on the Pt CE. The physical and chemical processes controlling H_2O electrolysis and H_2 oxidation on the thin-film GDC electrode of the electrochemical cell are illustrated in Figure 2.4. With a positive voltage bias ($V_{cell} > 0$) applied to the cell oxide ions (O^{2-}) are driven from the GDC WE, where H_2O electrolysis occurs, to the Pt CE, where H_2 is oxidized as illustrated in Figure 2.4a. On the other hand, a negative potential bias ($V_{cell} < 0$) drives H_2 oxidation on the GDC and H_2O electrolysis on Pt as illustrated in Figure 2.4b.

2.2.2 Electrode Surface Morphology Characterizations

Scanning electronic microscope (SEM) and optical microscope are used to characterize surface morphologies of the GDC electrode as shown in Figure 2.5. Figure 2.5(a) - (c) typified for Ni/GDC WE. The images illustrate Ni overlayer on the GDC film at different length scales. Figure 2.5a shows the borders of Ni/GDC and GDC/YSZ interfaces, with 350-μm width GDC surface exposed around the edges, which facilitates XPS measurements across the interface. Figure 2.5(b) and (c) show

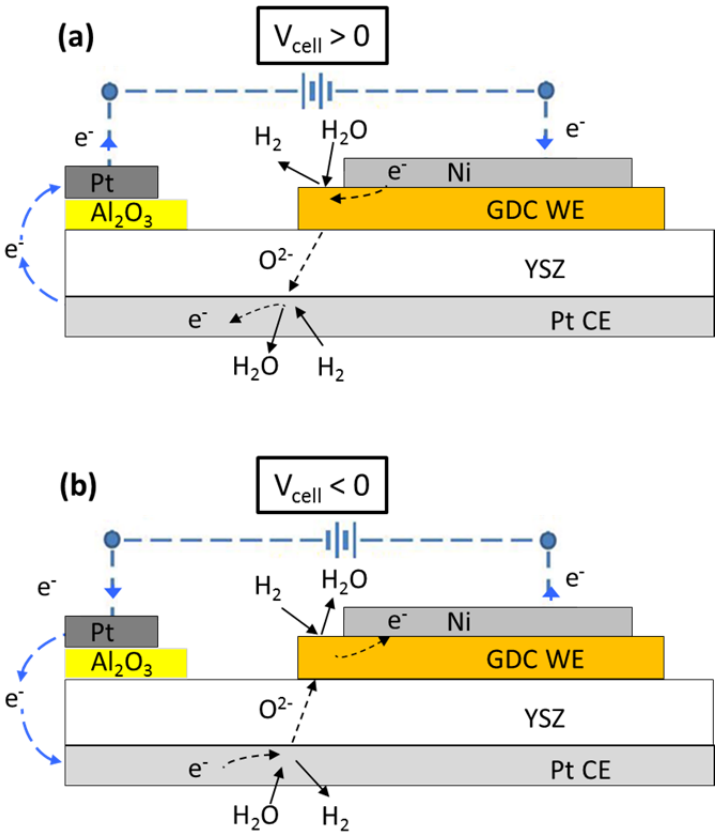

Figure 2.4. Working principles of the electrochemical cell (ex. with Ni metal overlayer): (a) when $V_{cell} > 0$, H_2O electrolysis takes place on the GDC WE, oxide ions are transported from the GDC WE to the Pt CE where H_2 oxidation occurs; (b) when $V_{cell} < 0$, H_2O electrolysis takes place on the Pt CE, oxide ions are transported from Pt CE to the GDC WE to the where H_2 oxidation occurs.

annealed Ni overlayer consisted of 1-2 μm wide structures using SEM and optical microscopy respectively. The structures provide adequate interconnection of the thin-film WE plane and good exposure of the GDC surface to increase the extent of three-phase boundary regions on the working electrode. Figure 2.5(d) shows optical

microscope image of the porous structures of Au/GDC WE. These images are used for calculation of metal/GDC TPB length in later kinetic development.

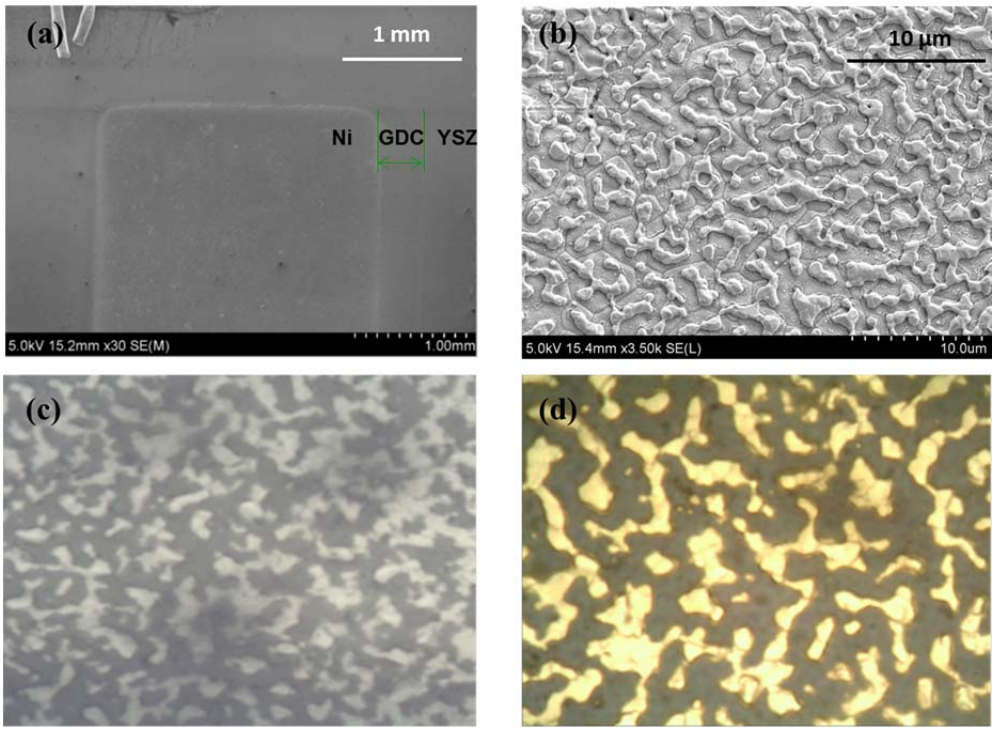

Figure 2.5. SEM images of GDC thin-film electrode with Ni overlayer of the electrochemical cell: (a) exposed GDC edge, clear border of Ni/GDC interface, (b) porous structures of Ni exposing similarly-sized areas of GDC. Optical microscopic images 150X magnitude: (c) Ni porous structures and (d) Au porous structures.

2.2.3 Experimental Test Set-up

The thin-film GDC electrochemical cells are electrochemically characterized at the University of Maryland (UMD) using single-chamber tests in a vertical tubular furnace. A broad range of tests are performed at P_{tot} = 1 bar, with P_{H2} and P_{H2O} (or

P_{CO} and P_{CO2}) ranging from 2 Torr to 20 Torr diluted by Ar between 600 and 700 °C. Testing conditions are summarized in Table 2.1. P_{O2} are calculated by running a constant temperature and pressure equilibrium calculation for the gas feed using the GRI 3.0 mechanism [91]. Ionic and electronic conductivities are estimated fitting to others' experimental studies on GDC and samaria-doped ceria (SDC) [53, 92] as

$$\sigma_{\text{ion}} = 4.2 \times 10^5 T^{-1} \exp\left(-\frac{7.37 \times 10^4}{\bar{R}T}\right) \ (\text{S/cm}) \qquad \text{(Eq. 2.1)}$$

$$\sigma_{\text{e}} = 4.52 \times 10^9 T^{-1} \exp\left(-\frac{2.417 \times 10^5}{\bar{R}T}\right) P_{\text{O2}}^{-1/4} \ (\text{S/cm}) \qquad \text{(Eq. 2.2)}$$

Table 2.1. Summary of experimental conditions for electrochemical cell tests

Temperature (°C)	P_{H2} (Torr)	P_{H2O} (Torr)	P_{CO} (Torr)	P_{CO2} (Torr)	P_{O2} (bar)	σ_{ion} (S/cm)	σ_e (S/cm)
600	2	2			1.33×10^{-24}	0.019	0.017
	10	2			5.32×10^{-26}	0.019	0.037
	20	2			1.33×10^{-26}	0.019	0.053
650	2	2			5.33×10^{-23}	0.031	0.038
700	2	2			1.47×10^{-21}	0.048	0.08
	10	2			5.86×10^{-23}	0.048	0.178
	20	2			1.47×10^{-23}	0.048	0.252
600			2	2	1.87×10^{-25}	0.019	0.027
			2	10	4.67×10^{-24}	0.019	0.012
			2	20	1.87×10^{-23}	0.019	0.009
650			2	20	1.28×10^{-21}	0.031	0.017
700			2	20	5.64×10^{-22}	0.048	0.101
600		2	2		4.99×10^{-25}	0.019	0.021

The electrochemical cell is first mounted onto a separate, dense YSZ pellet, which covers the entire alumina outer tube (22.2 mm OD, 15.9 mm ID) and thereby forms the base of an enclosed chamber on which the electrochemical cell is held. The YSZ pellet is sealed onto the bottom alumina outer tube with a zirconia-based ceramic paste (Ceramabond 571 from Aremco). A smaller alumina fuel feed tube (4.8 mm OD, 3.2 mm ID) runs down the center of the outer tube to provide gaseous reactants to the cell. The entire assembled rig is as shown in Figure 2.6, is then placed in the temperature-controlled tubular furnace.

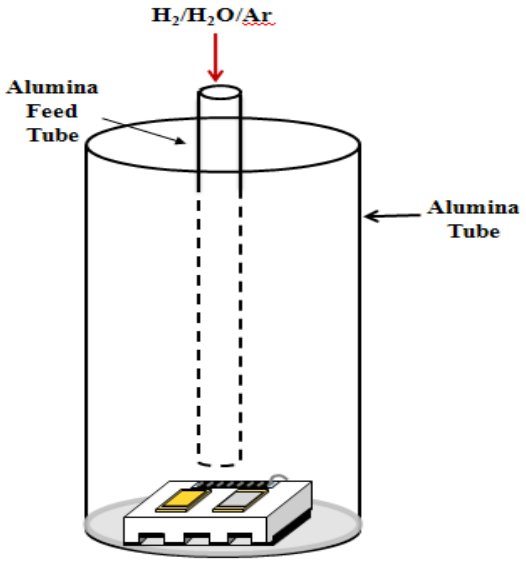

Figure 2.6. The electrochemical cell is mounted onto a dense YSZ pellet sealed with outer tube from atmosphere environment. The centered inner tube provides gas feedings.

The furnace heats the cell to operating temperatures (600 - 700 ºC) at a rate of 1 ºC/min initially under H_2/Ar mixtures, which is similar to the annealing condition,

provided by electronic mass flow controllers (MFCs – Brooks 5850E's). The reduced environment protects Ni from oxidation during the heating. Upon reaching the desired temperature, H_2O is added by sending secondary Ar through a humidity bubbler (Fuel Cell Technologies) at a controlled temperature to ensure a desired H_2/H_2O ratio for the cell. Temperatures and flow rates are monitored and controlled with K-type thermocouples and MFCs respectively using National Instruments' LabVIEW program. The entire experimental set-up diagram is illustrated in Figure 2.7. When testing CO/CO_2 mixtures, number 1 mass flow controller is fed with CO_2 and flow without going into the humidity bottle, number 2 mass flow controller is fed with CO. Electrical leads are attached to the metal overlayer and Pt using gauze mesh and metallic pastes (Sigma-Aldrich, Inc). The cell leads are connected to an Autolab workbench (Eco-Chemie), which is used to study electrochemical performance.

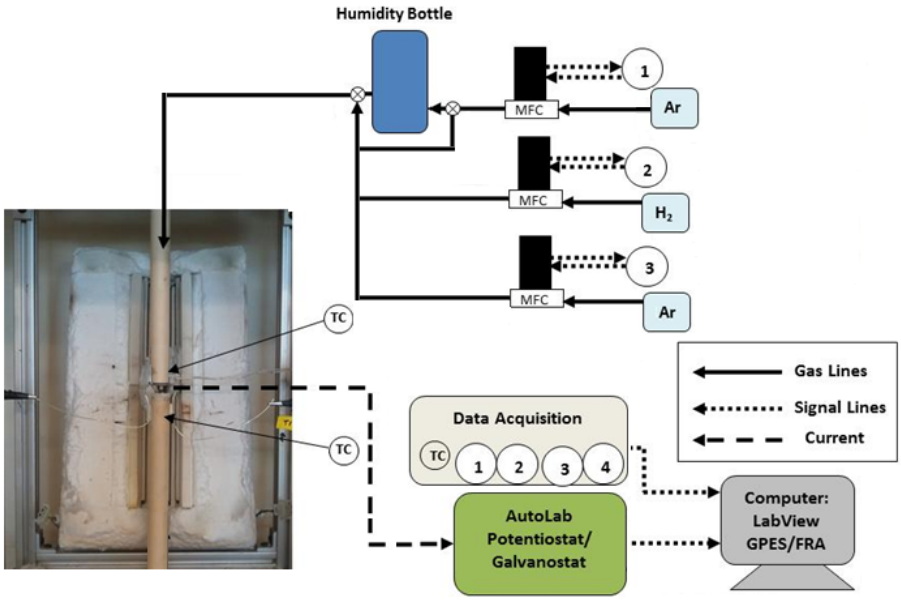

Figure 2.7. Schematic of experimental setup, gas flow, system control, and data acquisition as exemplified for H_2/H_2O/Ar feeds.

Electrochemical characterizations, including linear sweep voltammetry (LSV) and electrochemical impedance spectroscopy (EIS), are then carried out. LSV imposes a voltage bias across the electrochemical cell and sweeps across a range of user-specified voltages. In this study, the cell voltage bias ranges from -1.0 V to +1.0 V, allowing H_2 (CO) oxidation and H_2O (CO_2) electrolysis taking place on GDC electrodes. The IR_{bulk}-corrected voltages are plotted versus resulting current by subtracting Ohmic losses (IR_{bulk}) mostly attributed to oxide ion transport through the YSZ, for the purpose of analyzing contributions of GDC and Pt electrode overpotentials to LSV voltages.

The EIS measurements of complex impedance provide important information on the dynamic processes. The overall impedance is contributed by a sequence of processes, such as charge-transfer reactions, electronic and ionic conduction, surface chemistry, etc. The high-frequency intercept of the EIS Nyquist plot is also an effective mean to measure bulk resistance (R_{bulk}) and thus, estimate operation temperatures within XPS chamber where temperature measurement is unavailable. The low frequency impedance is primarily contributed by the electrode processes as it has strong dependence on P_{H2}/P_{H2O} ratios and voltage bias as discussed in the following section.

2.3 Results and Discussions

2.3.1 H_2/H_2O Electrochemistry on GDC Electrodes

Polarization and EIS experiments and analysis of H_2/H_2O reaction on the GDC WEs are carried out at a range of P_{H2}/P_{H2O} ratios at 600, 650, and 700 °C as specified in Table 2.1. The overall reaction is described as follows

$$H_{2(g)} + O^{2-}(GDC) \leftrightarrow H_2O_{(g)} + (GDC) + 2e^- \quad \text{(R.2.1)}$$

The IR_{bulk}-corrected *V-I* curves at 700 °C for GDC/Ni and GDC/Au are plotted in Figure 2.8a and 2.8b respectively. Both Ni/GDC and Au/GDC electrodes show much larger activation overpotentials on H_2 oxidation than H_2O electrolysis. Significantly more current is observed on H_2O electrolysis than on H_2 oxidation occurring on the GDC electrodes for a same bias magnitude on both Ni/GDC and Au/GDC electrodes. For example, current at V_{cell} = 0.3 V for both electrodes is approximately -1 mA, 10X magnitude of current at V_{cell} = - 0.3 V (< 0.1 mA), for $P_{H2} = P_{H2O}$ = 2 Torr.

Even though it has been suggested that activity for H_2 oxidation is higher than H_2O electrolysis on Pt/YSZ [65, 93, 94], the relatively large electrolysis currents on the GDC electrodes may be also enhanced by catalytic activity of the highly reduced GDC electrode. GDC-based electrodes increase activity during H_2O electrolysis operation [95, 96] by increasing the percentage of Ce^{3+} on the GDC surface. Higher currents at positive biases than at negative biases with the same magnitude are corroborated in similar undoped ceria studies [60, 61].

Both oxidation and electrolysis activities on the GDC are enhanced further by increasing P_{H2}/P_{H2O} ratios. Activation overpotential associated with both reactions are lowered and significantly more currents are seen at P_{H2}/P_{H2O} = 10. This is due to further reduction of Ce^{4+} and increased electron mobility on the GDC surface at lower P_{O2}, resulting in increased catalytic activity of the GDC electrodes.

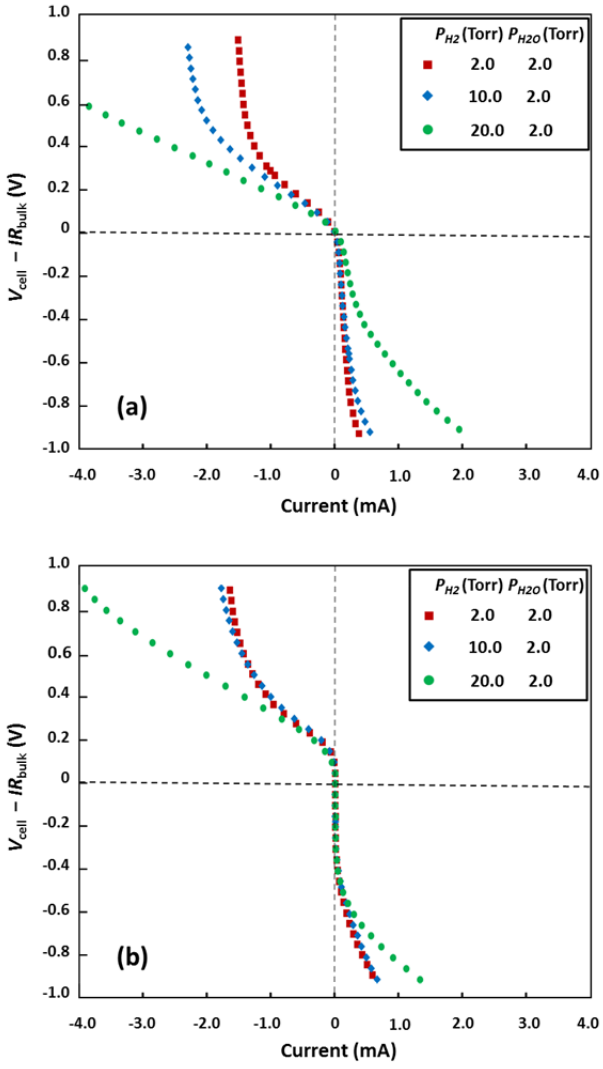

Figure 2.8. Electrochemical characterization of thin-film GDC electrochemical cell for a range of P_{H2}/P_{H2O} at 700 ºC. The IR_{bulk}-corrected *V-I* curves of thin-film GDC working electrodes with: (a) Ni overlayer and (b) Au overlayer.

In comparing Ni/GDC and Au/GDC electrode performances at $P_{H2}/P_{H2O} = 1$ between Figures 2.8a and 2.8b, similar *V-I* curve and maximum currents (1.5 mA on H_2O electrolysis and 0.5 mA on H_2 oxidation) regardless of using Ni or Au are observed. This suggests that reactions at this temperature mostly take place on the GDC surface while the contribution of metal (Ni or Au)/GDC interface is of secondary importance. The catalytically active of GDC surface at 700 ºC is due high ionic (~ 0.05 S/cm) and electronic conductivities (> 0.08 S/cm).

However, there are still synergetic effects of the active Ni (relative to the inert Au) for either oxidation or electrolysis. The significance of that activity is seen at the higher H_2/H_2O ratios in Figure 2.8 for both reactions. At $P_{H2}/P_{H2O} = 10$, current of Ni/GDC is -3.2 mA at $V_{cell} = 0.5$ V and 0.8 mA at $V_{cell} = -0.5$ V. While for Au/GDC the currents are only -2.0 mA and 0.5 mA at the same voltage bias respectively. Yet, it remains uncertain as to what drives the enhancement of the Ni electrode at the highest H_2/H_2O ratios (lowest P_{O2}).

The contribution of Ni metal overlayer to the electrochemical performance is further investigated through observing its effects at 600 ºC. Unlike 700 ºC, the enhancement of Ni/GDC over Au/GDC becomes significant at all P_{H2}/P_{H2O} conditions as compared between Figure 2.9a and 2.9b. At $P_{H2}/P_{H2O} = 1$, the maximum current of Ni/GDC electrode is -0.6 mA when doing H_2O electrolysis and 0.2 mA on H_2 oxidation. In general, the Ni/GDC electrode produces almost 2X of the current at the same potentials as the Au/GDC electrode at the same conditions at 600 ºC for all

P_{H2}/P_{H2O} ratios. Since both Ni/GDC and Au/GDC WEs use the same YSZ support and backside Pt CE, the differences between *V-I* curves at the same working condition can be attributed to differences of electrochemical behaviors of two WEs.

Ni, as an effective H_2 and H_2O dissociation catalyst [97, 98], promotes availability of intermediate species necessary for driving charge-transfer near the metal/GDC interface. At this lower temperature, ionic and electronic conductivities of GDC decrease approximately 60% and 78% respectively. Thus, vertical charge flux is more favorable than horizontal flux, because distance across GDC electrode (300 nm) is much shorter than GDC open surface (several μm). In this case, reactions are mostly limited to metal/GDC interfaces. This is consistent with the conclusion that hydrogen dissociation occurs primarily on the metallic component of the SOFC anode with very little interaction with the underlying oxide at temperature below 600 ºC [99].

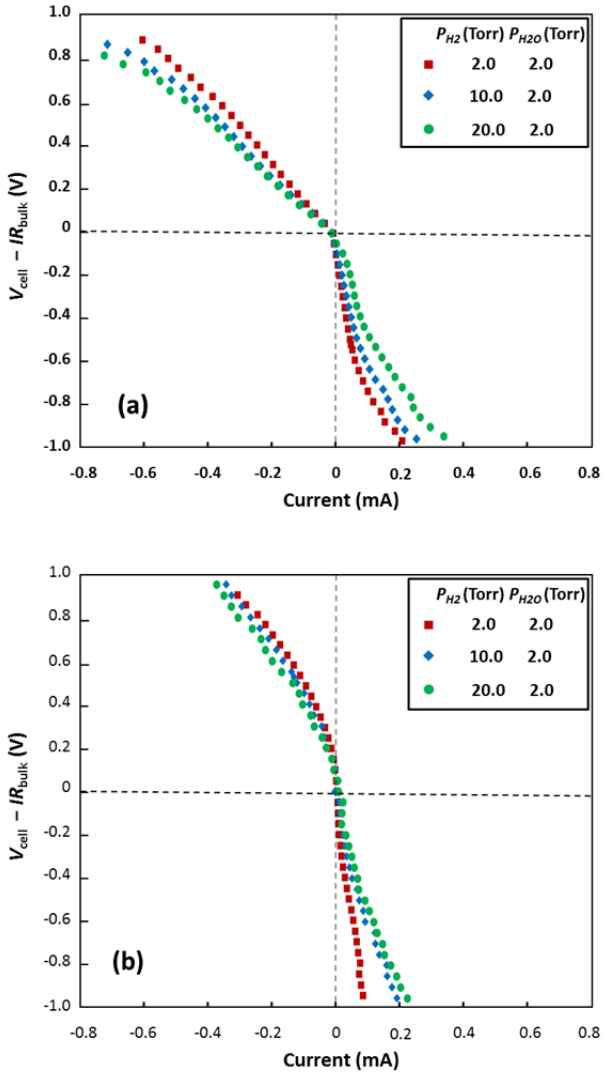

Figure 2.9. Electrochemical characterization of thin-film GDC electrochemical cell for a range of P_{H2}/P_{H2O} at 600 ºC. The IR_{bulk}-corrected V-I curves of thin-film GDC working electrodes with: (a) Ni overlayer and (b) Au overlayer.

EIS tests provide an alternative window into the electrochemical behavior. Figure 2.10a and 2.10b present Nyquist plots for Ni/GDC and Au/GDC respectively. The impedances are measured at V_{cell} = 0 V with a 10 mV sinusoidal perturbation at

P_{H2} = P_{H2O} = 2 Torr between 600 ºC and 700 ºC. The impedances, as shown in the figures, are divided into Ohmic resistance and polarization resistance. The high frequency intercepts correlate the Ohmic resistance (R_{bulk}) with the cell as a function of temperature as exemplified in Figure 2.10a. Such R_{bulk} and temperature relations are fitted in an Arrhenius form expression, as shown in Eq.2.3, which are used later for calibration of XPS measurements temperatures.

$$R_{\text{bulk}} = 3 \times 10^{-7} T \cdot \exp\left(\frac{96309}{\bar{R}T}\right) \text{ (Ohm)} \qquad \text{(Eq. 2.3)}$$

The largest polarization resistances are observed at medium and low frequency with a strong dependency on temperature. Increasing temperature not only decreases R_{bulk} but also significantly decreases low frequency impedances. The polarization impedance at 700 ºC is less than 1/3 of its value at 600 ºC as shown in Figure 2.10a.

In comparison between impedances of Ni/GDC and Au/GDC electrodes, shapes and magnitudes are close at 650 ºC and 700 ºC. However, the imaginary part low frequency impedance of Au/GDC becomes much higher than Ni/GDC at 600 ºC. The increase in impedance is attributed to the limited activity of the Au relative to the Ni at the lower temperature where limited GDC electronic conductivity limits the amount of electronic transport on the GDC. Thus, the increased Au/GDC impedance is attributed to slower charge transfer across the Au/GDC interfaces.

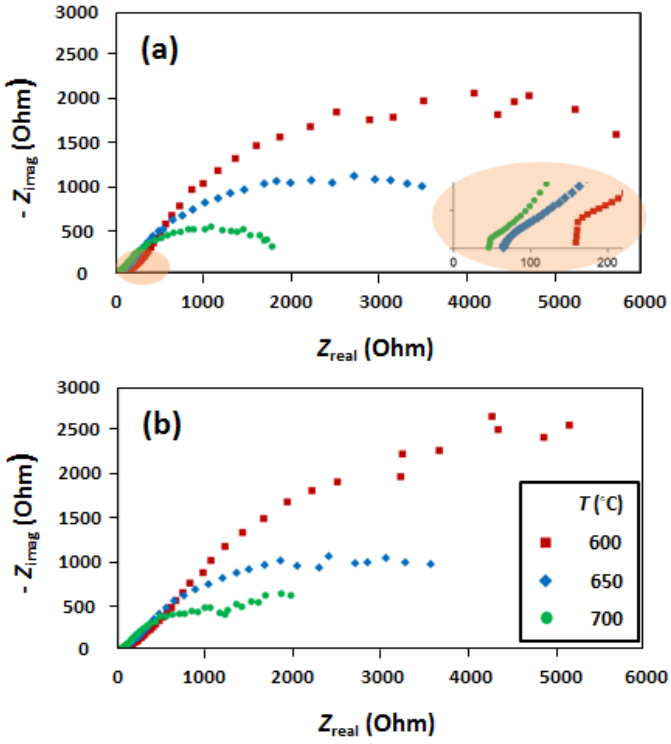

Figure 2.10. Temperature dependency of impedances and R_{bulk} at V_{cell} = 0, P_{H2} = P_{H2O} = 2 Torr: (a) Ni overlayer and (b) Au overlayer.

Figure 2.11a demonstrates impedances of Ni/GDC electrode when H_2O electrolysis occurs at 0.3 V and H_2 oxidation occurs at -0.3 V. Significantly lower resistances are observed when H_2O electrolysis takes place on the GDC electrodes. The lower resistance is partly due to faster rates for H_2 oxidation on Pt CE. Such distinct impedances on +/- V_{cell} may also due different catalytic activity of GDC electrode on each reaction. Figure 2.11a also shows that increasing P_{H2} decreases resistances of both reactions. Promotion of both reactions by increasing P_{H2} activity suggests this large impedance is likely controlled by processes associated with the catalytic activity of GDC electrode.

Examination of Bode plots in Figure 2.11b reveals higher characteristic frequency (~2 orders of magnitude) of positive voltage when H_2O electrolysis occurs than negative voltage when H_2 oxidation occurs. It is still unclear whether it is the H_2O electrolysis on GDC or H_2 oxidation on the Pt CE that dominates this faster reaction at positive voltage. Impedances of both +/- voltages are reduced at higher P_{H2} without significantly shifting characteristic frequency.

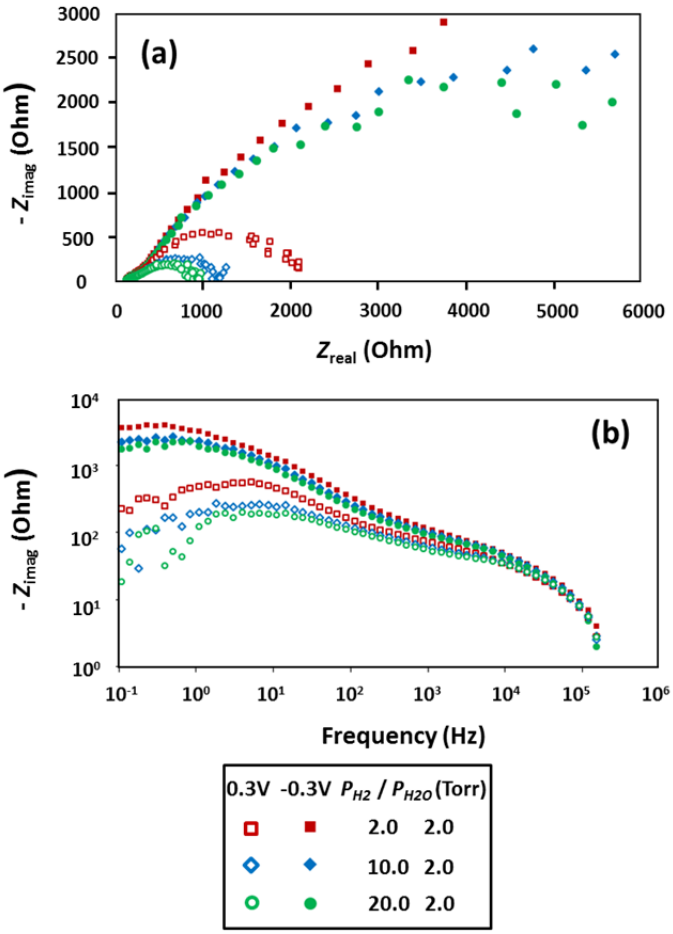

Figure 2.11. Impedance spectra of H_2/H_2O reaction on cell with Ni/GDC electrode at V_{cell} = 0.3 V (H_2O electrolysis on GDC) and -0.3 V (H_2 oxidation on GDC), for a range of P_{H2}/P_{H2O} ratios at 600 ºC: (a) Nyquist plot and (b) Bode plot of imaginary impedance showing characteristic frequencies.

2.3.2 CO/CO_2 Electrochemistry on GDC Electrodes

In this study, electrochemical tests also explore CO electrochemical oxidation using CO/CO_2 gas mixtures. Polarization and EIS measurements of CO/CO_2 reaction on the GDC electrochemical cells are carried out at a range of range of P_{CO}/P_{CO2} ratios (1.0 or lower) between 600 and 700 °C, as specified in Table 2.1. The overall reaction is described as follows

$$CO_{(g)} + O^{2-}(GDC) \leftrightarrow CO_{2(g)} + (GDC) + 2e^{-} \quad \text{(R.2.2)}$$

The limited ranges of relatively low CO/CO_2 ratios are implemented to avoid carbon build-up. Based on observations of temperature-dependent behaviors in H_2/H_2O tests, the CO/CO_2 study mainly focuses on lower temperature at 600 °C. The IR_{bulk}-corrected *V-I* curves for Ni/GDC and Au/GDC electrodes are plotted in Figure 2.12a and 2.12b respectively.

The currents for both Ni/GDC and Au/GDC on CO/CO_2 reactions are much lower than those on H_2/H_2O reaction at 600 °C. For $P_{CO} = P_{CO2} = 2$ Torr, despite the effective oxygen partial pressure ($P_{O2} = 1.87\times10^{-25}$ bar) is even lower than that of $P_{H2} = P_{H2O} = 2$ Torr ($P_{O2} = 1.33\times10^{-24}$ bar). The maximum current for CO oxidation on GDC electrode is approximately 1/10 of maximum current for H_2 oxidation. Previous research in AC impedance study on H_2–H_2O–CO–CO_2 mixtures also suggests a much slower electrochemical oxidation rate for CO than for H_2 [100]. The lower reaction rate associated with CO/CO_2 mixtures may be due to higher energy barriers of electrochemical reaction of CO or less catalytic activity of carbonaceous species on the Pt CE.

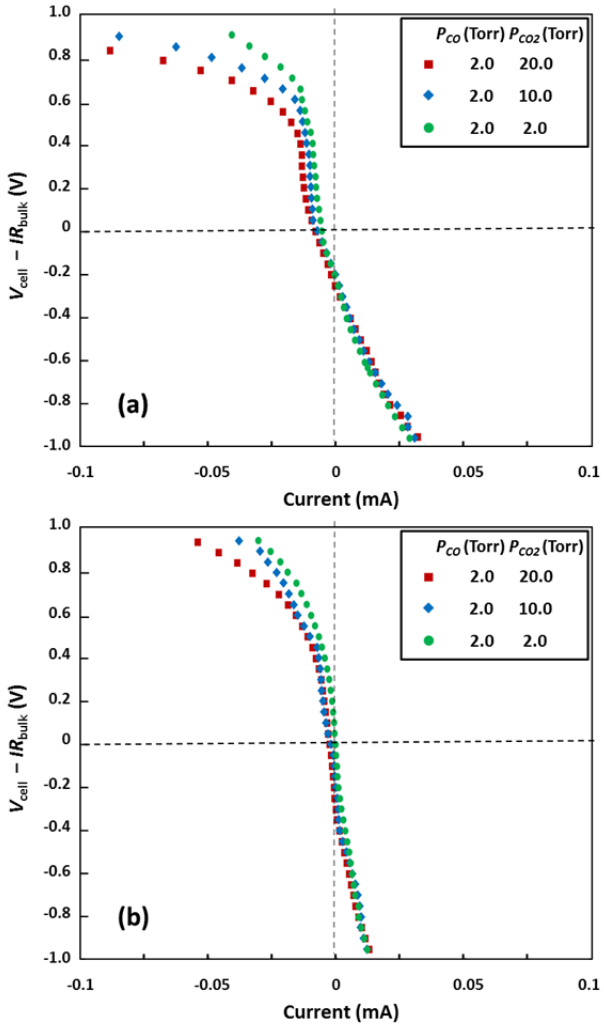

Figure 2.12. Electrochemical characterization of thin-film GDC electrochemical cell for a range of P_{CO}/P_{CO2} at 600 ºC. The *V-I* curves are plotted with IR_{bulk}-corrected V_{cell} for thin-film GDC working electrodes: (a) with Ni overlayer and (b) with Au overlayer.

Comparing Ni/GDC and Au/GDC performances in Figures 2.12a and 2.12b shows that Ni/GDC currents are 2X of Au/GDC currents for both CO oxidation and CO_2 electrolysis at 600 ºC. Significant shift on equilibrium potential (V_{cell} = 0) is

observed on Ni/GDC electrode as shown Figure 2.12a. Changes the equilibrium potentials may be due to CO_2 dissociation on the Ni surface which results in chemisorbed CO and perhaps even some dissociated C [101]. Such a thermodynamic favorable chemisorption on the Ni surface involves formation of ionic bonds Ni surface [102] as shown in R.2.3

$$\mathrm{CO(Ni)} + \mathrm{(Ni)} \leftrightarrow \mathrm{C(Ni)} + \mathrm{O(Ni)} \qquad \text{(R.2.3)}$$

At high positive biases, the role of Ni in splitting CO_2 becomes significant. At P_{CO}/P_{CO2} = 1/10, maximum current at positive potential is as high as -0.1 mA which is 3X of maximum current at P_{CO}/P_{CO2} = 1, while the Au/GDC electrode only increases 2X of the maximum current as P_{CO2} increases. This further demonstrates that chemisorption and dissociation of CO_2 on the Ni surface enhances the Ni/GDC electrode performance. Also as P_{O2} decreases, enhancement of CO oxidation is not observed as H_2 oxidation on the GDC electrode. This further implies that CO oxidation mainly depends on metal/GDC interaction rather than GDC itself.

The effects of temperature on CO/CO_2 chemistry are further studied on the Ni/GDC electrode. The P_{CO}/P_{CO2} ratio is limited to 1/10, in order to avoid carbon formation. Figure 2.13 shows IR_{bulk}-corrected *V-I* curves of Ni/GDC electrode between 600 and 700 ºC. Much lower overpotenitals and better performances are shown on both CO_2 electrolysis and CO oxidation as temperature increases form 600 ºC to 700 ºC. The maximum currents produced by CO/CO_2 reactions are approximately 1/10 of H_2/H_2O reaction at the same temperature.

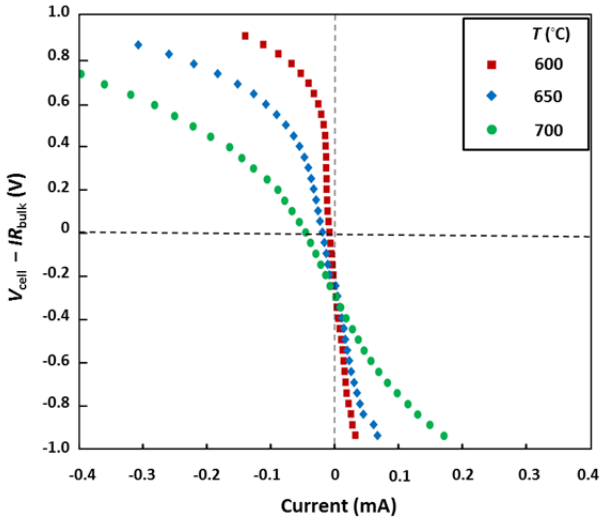

Figure 2.13. Temperature dependency of IR_{bulk}-corrected *V-I* curves of Ni/GDC electrode, at P_{CO} = 2 Torr and P_{CO2} = 20 Torr.

Compared to H_2/H_2O reaction impedances in Figure 2.10, CO/CO_2 reaction has much higher low frequency impedances at the same temperature, as shown in Figure 2.14. Ohmic resistances (R_{bulk}) are also higher than H_2/H_2O reactions Ni/GDC at the same temperature. Increase of R_{bulk} values has also been observed in experimental study of Ni/GDC anode SOFCs on reformate feeds [51]. This may be due to interactions between carbon-based species with the Ni/GDC electrode which reduces its electrical conductivity.

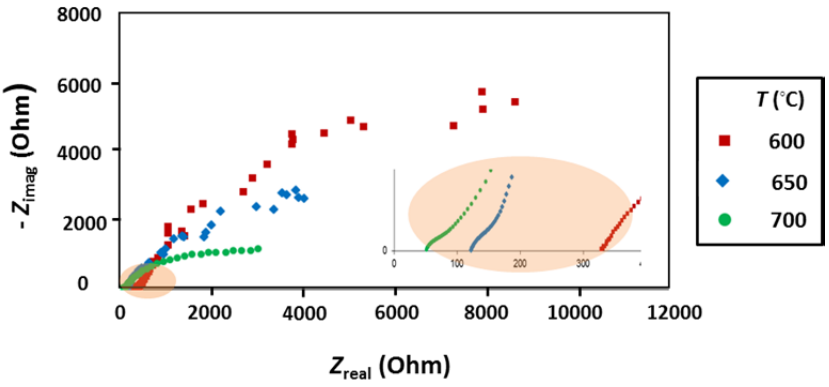

Figure 2.14. Nyquist plots of impedance spectra for Ni/GDC electrode, at V_{cell} = 0, P_{CO} = 2 Torr and P_{CO2}= 20 Torr.

In addition to H_2/H_2O and CO/CO_2 studies, CO/H_2O mixture of same partial pressure ($P_{CO} = P_{H2O}$ = 2 Torr) is also tested at 600 ºC. Much better electrochemical performance than CO/CO_2 mixture is observed on CO/H_2O mixture as shown in Figure 2.15. The enhanced performance for CO/H_2O mixture is due to relatively fast water-gas shift reaction (R.1.1) taking place that converts CO into H_2. Thus, H_2 oxidation/H_2O electrolysis dominates the GDC electrode reaction corresponding to the potential bias.

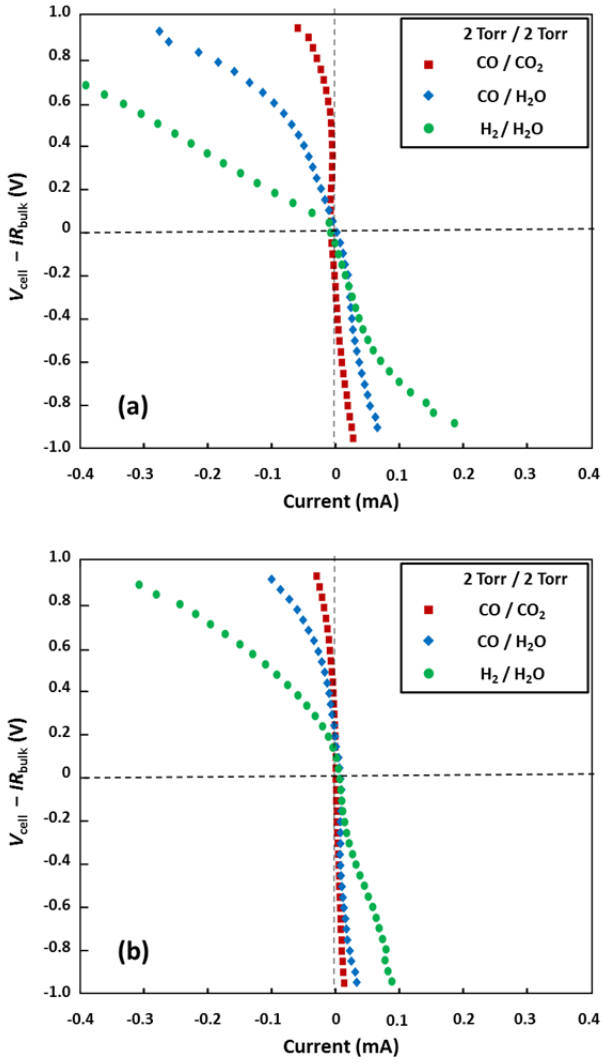

Figure 2.15. Electrochemical characterization of thin-film GDC electrochemical cell for a range of gas compositions at 600 ºC. The *V-I* curves are plotted with IR_{bulk}-corrected V_{cell} thin-film GDC working electrodes: (a) with Ni overlayer and (b) with Au overlayer.

Currents of CO/H_2O mixture are still lower than H_2/H_2O mixture at the same voltages bias. CO adsorption may reduce the Ni surface availability for any H_2/H_2O charge-transfer reaction due to its relatively high adsorption enthalpy relative to H_2 on

Ni [103]. The study of heterogeneous reaction on Ni catalysts has shown high CO coverage on the Ni surface at similar conditions [9]. Interaction between carbonaceous species and the Ni/GDC electrode may also reduce catalytic activity. Recent studies on undoped ceria have suggested formation of carbonate species (CO_3^{2-}) on the ceria surface as reaction intermediates [64, 104]. Such species are likely less mobile on the GDC surface and may inhibit ion transport along the surface and reduce the area of GDC available for electrochemical reactions.

2.4 Conclusions

Electrochemical processes of H_2/H_2O and CO/CO_2 over GDC electrode are investigated using sputter-deposited thin-film GDC electrochemical cells. Electrochemical reactions on metal/GDC electrodes are enhanced at lower oxygen partial pressures and/or higher temperatures. Increasing P_{H2}/P_{H2O} ratio from 1:1 to 10:1 at 700 °C, maximum currents are enhanced approximately 4X for H_2O electrolysis and 2-3X for H_2 oxidation. And at 600 °C, maximum currents also increase as P_{H2}/P_{H2O} ratio increases even though the enhancement is not as much as that at 700 °C.

Comparison of Ni/GDC and of Au/GDC at the same conditions, suggests significantly different electrochemical behavior of the two metal/GDC electrodes at different operation temperatures. At 600 °C, both ionic and electronic conductivities are reduced at this temperature, thus the charge-transfer reactions take place close to the metal/GDC interface. A catalytic active metal (ex. Ni) is able to synergize with

GDC electrode in promoting the charge-transfer reactions. Whereas, as temperature rises to 700 °C, further reduction of GDC surface and enhanced conductivities extend the charge-transfer reaction from metal/GDC/gas TPB to GDC surface. The role of metal catalyst is less important.

By comparing oxidation/electrolysis performance on of H_2/H_2O, CO/CO_2 and CO/H_2O, observation of much faster (~10X maximum currents at 600 °C) reactions of H_2/H_2O than CO/CO_2 on the GDC electrodes conclude electro-oxidation of H_2 dominates fuel oxidation. Fast water-gas shift reaction facilitates conversion of CO into H_2, which enables fast oxidation of H_2. Presence of carbon-based species in the gaseous environment still slows down H_2 oxidation and H_2O electrolysis possibly due to surface coverage of active site of the Ni/GDC electrode.

Experiments carried out in this chapter demonstrate the importance of charge transfer at the Ni/GDC boundary, oxidation state of GDC surface, GDC ionic and electronic conductivities, and surface reactive species. These results provide a list of possible reaction kinetics during IT-SOFC Ni/GDC anode operation environments.

Chapter 3: Ambient Pressure X-ray Photoelectron Spectroscopy Characterization of Metal/GDC Electrodes

3.1 Introduction

Electrochemical characterizations (LSV and EIS) of the GDC-based electrodes, as described in Chapter 2, leave a number of questions concerning the fuel oxidation kinetics. The chemical behavior of the GDC electrode surface during the reaction process needs to be directly observed for a richer understanding of the kinetic mechanisms. In addition, understanding the interactions of the metal overlayer with the GDC surface is crucial. Isolating these interfaces from the overall electrochemical performances is challenging as well. However, little is known about the Ni/GDC electrochemistry governing H_2 and/or CO oxidation at IT-SOFC anode working environments in order to optimize the anode microstructures for IT-SOFC applications.

X-ray photoelectron spectroscopy (XPS) enables the analysis of the chemical composition and oxidation states of solid surfaces. In XPS, irradiation of solid surface with mono-energetic x-rays emits electrons, which are collected through optical focusing at high vacuum to a detector, which separates the emitted electrons by kinetic energy. Quantitative analysis of the resulting energy spectra from the emitted electrons helps to identify the chemical states [105]. Ambient pressure XPS (AP-XPS) utilizes differential pumping stages of the electron optical path to allow the measured samples to operate at several Torr pressures. AP-XPS is an effective tool for

investigating both chemical and electrical properties. The effectiveness of ambient pressure XPS has been demonstrated by recently studies on electrochemical cells [60-62, 94, 106].

This chapter presents the use of *in operando* AP-XPS to probe GDC electrode for the purpose of understanding properties that are responsible for the catalytic activity and charge-transfer reaction. The AP-XPS measurements are performed at the Advanced Light Source (ALS) on beamline 9.3.2 located in the Lawrence Berkeley National Laboratory (LBNL). Simultaneous electrochemical characterization and XPS measurements are taken to visualize local surface potentials and interfacial overpotentials, change of surface reactive species, as well as surface oxidation state associated with H_2/CO oxidation and H_2O/CO_2 electrolysis.

3.2 Ambient Pressure XPS Measurement Techniques

Surface analysis by XPS is accomplished through irradiating a sample with mono-energetic X-rays whose photons can excite near surface electrons by the photoelectric effect, leading to emissions of electrons with binding energy (*BE*) levels below the excitation energy. The emitted electrons have kinetic energies (*KE*) given by

$$KE = h\nu - BE - \phi_s \qquad \text{(Eq. 3.1)}$$

where $h\nu$ is the energy of the source photons, *BE* is the binding energy of the atomic orbital from which the electron originates, and ϕ_s is the spectrometer work function,

which is usually a fixed value. The *KE* of emitted electrons corresponds to the emitted electron's *BE*, also regarded as ionization energy for the particular atomic shell involved [105]. Figure 3.1 gives an example of oxygen XPS corresponding the orbital and binding energy. With X-rays of a particular wavelength incident onto the sample surface, kinetic energies of emitted electrons associated with the O1s and O2s orbitals are measured. Kinetic energies are plotted as electron binding energy of each of the emitted electrons determined by Eq.3.1 above.

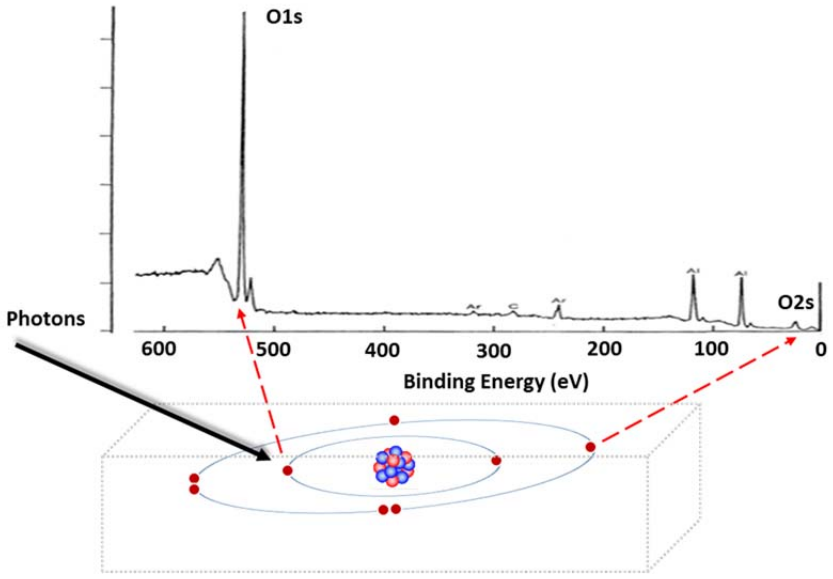

Figure 3.1. Schematic of XPS physics. X-rays with particular wavelength incident onto the sample surface, kinetic energies of emitted electrons associated with the O1s and O2s orbitals are measured and electron binding energy can be determined.

Conventional XPS requires ultra-high vacuum (UHV), but high-intensity sources at synchrotrons like ALS provided adequate fluxes of electrons from surfaces

such that they can pass through a low-pressure gas environment into a pumped electrostatic lens system [107, 108]. This so-called ambient-pressure XPS (AP-XPS) enables measurement of elemental composition and chemical states of electrochemical systems during operation (i.e. *in operando*) [108, 109]. Thus, AP-XPS is suitable for studying GDC electrode surface with presence of reactive gases.

Recent researches using AP-XPS to study electrochemical cells have shown a direct correlation between XPS measured kinetic energy of elements and electrical potential of the electrochemical cell components [60, 61, 96]. Shift of local electric potential results in a change of the local Fermi level, which corresponds to ionization energies of a core-level element. By applying external voltage bias, a shift of the emitted kinetic energy (ΔKE) spectra is observed. The magnitude of this shift is actually a shift in binding energy (ΔBE), in eV, is related to the local potential change (V) of the source as expressed in the following equation

$$\Delta KE = -\Delta BE = e * \Delta V \qquad \text{(Eq. 3.2)}$$

where ΔV is the change in voltage of the near surface and e is the charge associated with a single electron. Such a correlation between ΔKE and ΔV allows a direct, contactless measure of local surface potentials [110, 111].

In the current study of the thin-film GDC electrochemical cell using AP-XPS, the metal overlayer is grounded (fixed to zero) and various potential biases are applied to the Pt counter electrode during the experiments. When applying a positive/ negative potential bias, kinetic energy of core-level electron of electrochemical cell

component surface decreases / increases. For example, when a +1.0 V potential is applied to the Pt CE in the experiment, the kinetic energy of the photoelectrons emitted from the Pt electrode is reduced by 1.0 eV, corresponding to an equivalent 1.0 eV increase in *BE* from the Pt electrode. Therefore, local surface potential of the probed surface is acquired by analyzing the *BE* spectra in the XPS measurement.

In this study, the electrochemical cells are studied in single-chamber experiments, where working and counter electrodes are exposed to the same gas environment. Hence, thermodynamic equilibrium potential V_{cell} = 0.0 V at all locations. When applied bias, the local surface potential shifts and the difference across interfaces provides a measure of overpotentials driving the various electrochemical processes at a certain current [112]. The overpotentials associated with GDC electrodes reactions provide insightful kinetic information.

3.3 Description of Experiments

3.3.1 Ambient Pressure XPS Facilities Description

In operando AP-XPS characterizations of the thin-film GDC electrochemical cell are taken on beamline 9.3.2 at ALS. Even though AP-XPS test chamber allows elevated pressure, the X-ray source and electron analyzer must operate at UHV. The X-ray source is separated by a thin (100 nm) silicon nitride window, and the hemispherical electron analyzer is separated by differential pumping through a series of open apertures. The focused X-ray beam passes through the chamber at a shallow angle (values) and reflects off on the cell surface. The intensity of incident X-ray

beam into the experimental chamber can be selected by tuning the aperture stop at the outlet of bend magnet source (30-850 eV).

The emitted electron signal is captured in a two-dimensional (2-D) detector with electrostatic focusing optics. Data is recorded in two dimensions, one representing *KE* and the other spatial distribution. The imaging mode is able to study sample surface on the scale of hundreds of microns with a spatial resolution of ~ 16 μm. Such a capability is later used to map element *BE* across a 1-D spatial line over the metal/GDC interface, the GDC surface and the GDC/YSZ interface.

The test chamber is equipped with a four-axis motor system to precisely control sample motion. The programmed control is able to record and locate the sample to the desired areas that are identified on the edge of GDC surface and interfaces through pre-testing probing. The sample holder has an alumina heater, to heat the electrochemical cell to characterization temperatures as high as 700 °C. The main chamber is backfilled with reactant gases to several hundred mTorr at elevated temperatures to facilitate studying GDC electrode electrochemistry.

3.3.2 Test Procedures and Measurements

The thin-film electrochemical cell is specially designed to expose the GDC-based working electrodes and their interfaces of interest to the incident X-ray beam in the AP-XPS facility. The sharp and appropriate width of exposed GDC edge, shown

in Figure 2.5a, enables XPS scanning covers metal/GDC interface, GDC surface, and GDC/YSZ interface.

The electrochemical cell is clipped onto the sample holder with three spring-loaded probes [113]. The Ni and Au overlayers on the GDC WE and the Pt mesh connected to CE are placed separately under the pressured tips of each probe with Au foil for better contact. The sample holder together with the GDC cell is then transferred into the XPS chamber. Figure 3.2 shows the mounted electrochemical cell seated in the ambient pressure XPS chamber. All of the three electrodes are connected outside XPS chamber to potentiostat (Bio-Logic) for simultaneous electrochemical characterization and XPS measurements. One of the GDC WEs, either with Ni or Au, is disconnected to the potentiostat while the other is under electrochemical study.

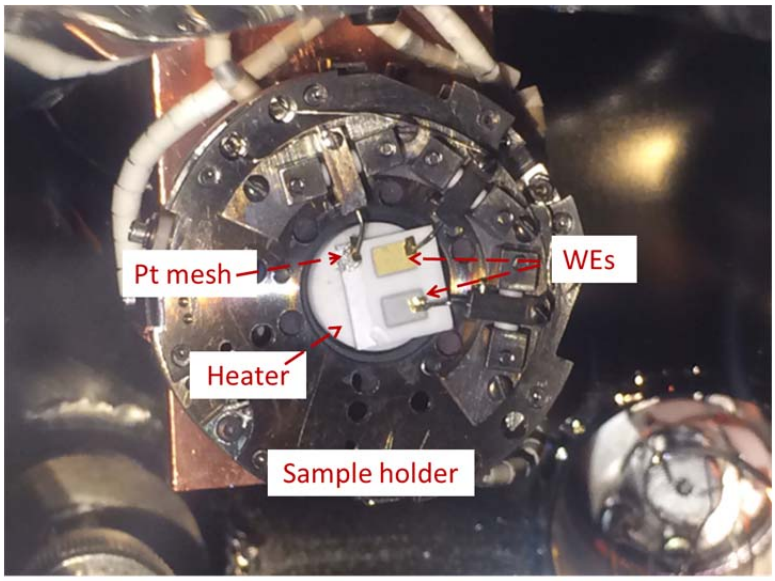

Figure 3.2. Picture of mounted electrochemical cell seated in the ambient-pressure XPS chamber at ALS.

Before increasing the chamber temperature, reactant gases (H_2/H_2O or CO/CO_2) are backfilled through leakage valves into the XPS chamber to the desired gas composition, with partial pressures monitored via mass spectrometry. Due to beamline time limitation, representative combination of gas ratios and temperature are selected for XPS characterization. Such combinations allow for kinetic studies through exploring the effects of P_{H2}/P_{H2O}, P_{CO}/P_{CO2} and their impact on effective P_{O2} on the overall activity of the working GDC electrode for H_2/CO oxidation and H_2O/CO_2 electrolysis. P_{O2} is calculated in equilibrium of the gas environments. Ionic and electronic conductivities are calculated through Eq.2.1 and Eq.2.2.

Table 3.1. Summary of experimental conditions for thin-film GDC electrode tests

Temperature (°C)	P_{H2} (Torr)	P_{H2O} (Torr)	P_{CO} (Torr)	P_{CO2} (Torr)	P_{O2} at 0 V (bar)	σ_{ion} (S/cm)	σ_e (S/cm)
570	0.2	0.2			1.18×10^{-25}	0.014	0.009
620	0.2	0.2			6.11×10^{-24}	0.023	0.023
	0.2	0.04			2.45×10^{-25}	0.023	0.053
620			0.04	0.36	8.68×10^{-23}	0.023	0.012
			0.2	0.2	1.07×10^{-24}	0.023	0.037

After stable gas pressures, the cell is heated to test temperatures at a rate of ~10 °C/min by increasing the heating coil current. Temperature is held constant for 20 min before collecting data. The electrochemical characterizations are carried out at 570 °C and 620 °C. This temperature values are determined by interpolating a temperature-bulk resistance (R_{bulk}) relation acquired at UMD tests shown in Chapter 2. Interpolation is used to estimate temperature, because the counter and reference

electrode leads consume some of the dedicated wire feeds to the low pressure XPS chamber that are otherwise dedicated to thermocouples.

Simultaneous XPS measurements are taken at constant V_{cell} = 0V, +/- 0.6V, and +/- 1.0V, at each gas composition. Table 3.2 lists core-level binding energies of specific atoms studied with setting parameters, such as estimated number of sweeps, spectral range, number of sweeps, and measurement step size.

Table 3.2. Core-level binding energies of specific atoms to be studied with setting parameters in XPS characterization.

Spectra	Excitation energy (eV)	Spectral range (eV)	Sweeps	Step Size (meV)
Survey	650	-2 to 320	1	100
O1s	650	525-545	10	50
Ni3p	490	60-70	5	100
Au4f		80-90		
Ce4d	490	100-135	12	50
Gd4d		135-175		
Zr3d		175-195		
C1s	490	280-295	6	50

The current study focuses primarily on the O1s spectra to explore hydroxyl and oxide content on GDC electrodes surfaces associated with H_2/H_2O electrochemistry [109, 114]. There are mainly two reasons to choose O1s spectra. Firstly, the O1s spectra are continuously observed across the entire length of metal/GDC/YSZ edge while Ce4d and Gd4d peaks are only observed on the GDC

surface. Secondly, strong O1s spectra peaks and better signal/noise ratio shown on the survey scanning while Ce4d and Gd4d peaks are largely affected by common surface contamination elements, such as P2p and Si2p.

Studies of the O1s spectra are primarily measured as a function of potential bias (V_{cell}) and effective P_{O2} at locations near the meatal/GDC interfaces. The grounded Ni or Au assists to calibrate binding energy of the spectra. Overpotentials extracting from changes in BE shifts of O1s primary peak across interfaces are studied at different conditions. Comparing overpotentials for the Ni/GDC and Au/GDC electrodes elucidate the impact of the metal on H_2 oxidation in metal/GDC electrodes. Additionally, concentration changes of surface reactive species on GDC associated with the charge-transfer reaction are explored to provide a basis for understanding the nature of the electrochemistry.

CO/CO_2 mixtures are also studied to elucidate simple carbonaceous species electrochemistry on metal/GDC. It should be noted that these results are relatively limited due to the minimal beam time dedicated to these experiments. In these CO/CO_2 studies, the O1s spectra are analyzed to extract relative concentrations of surface oxide species as a basis for understanding CO oxidation in composite GDC electrodes. To compare reaction rates of CO oxidation with H_2 oxidation, overpotentials are studied in similar environments.

3.4 Results and Discussions

3.4.1 AP-XPS Measurement of Metal/GDC Electrodes with H_2/H_2O

Electrochemical behaviors of the Ni/GDC and Au/GDC electrodes on H_2/H_2O reactions are studied at 570 and 620 °C. The IR_{bulk}-corrected *V-I* curves as plotted in Figure 3.3(a) and (b) on different scales for current. Electrochemical performances are consistent with observation of the 600 °C results tested in UMD as presented in Chapter 2. For both electrodes, higher overpotentials are associated with the H_2 oxidation on the GDC surface than with H_2O electrolysis at the same magnitude of current. Currents H_2/H_2O reactions of both electrodes increase when raising temperatures.

Comparing performances between Ni/GDC and Au/GDC shows that Ni/GDC delivers better performance on both the forward H_2 oxidation and the reverse H_2O electrolysis reaction at both temperatures. It should be noted that, when temperature rises from 570 °C to 620 °C, current of Ni/GDC increase 5X while current increase on the Au/GDC is not that significant. This performance enhancement must be attributed to Ni/GDC electrode, because both Ni/GDC and Au/GDC electrodes share the same YSZ substrate and Pt CE that the performance improvement of Pt/YSZ CE should be the same when raising temperature.

Comparing the overpotentials between Ni/GDC and Au/GDC electrodes at the same current magnitude at 620 °C, for example at -0.3 mA, much lower overpotential is seen on the Ni/GDC. Fast H_2 oxidation takes place on Pt CE which has much lower

overpotentials. Therefore discrepancies between cell voltage deviations must be attributed to difference between Ni/GDC and Au/GDC WEs. Further investigations using AP-XPS measurements as a measure of the local overpotentials are discussed later in this chapter.

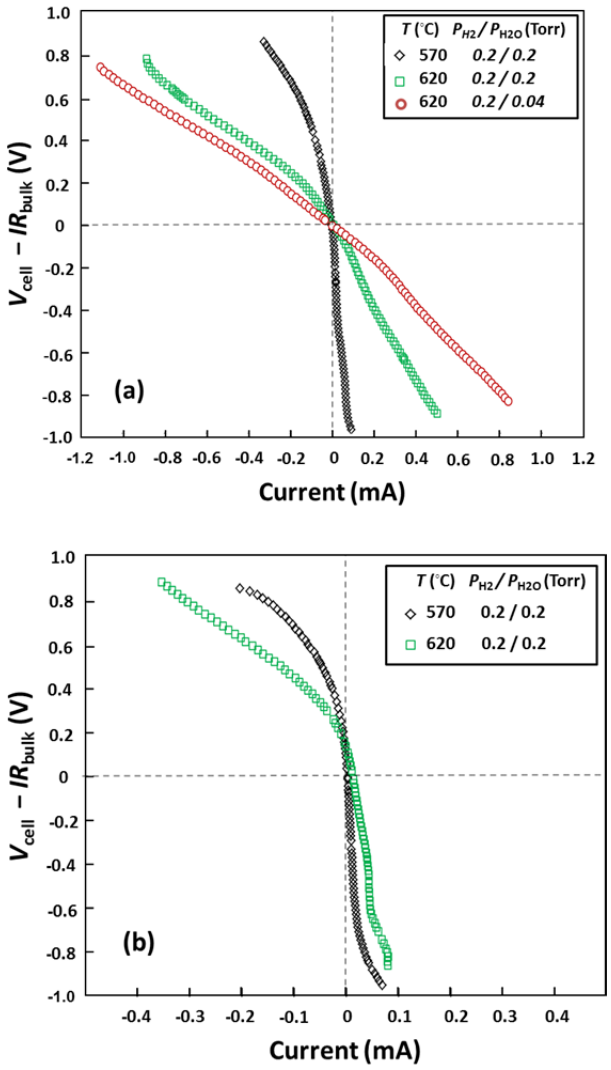

Figure 3.3. Electrochemical characterization of thin-film GDC electrochemical cell for a range of P_{H2}/P_{H2O} at 570 and 620 ºC tested at ALS. The IR_{bulk}-corrected *V-I* curves of thin-film GDC electrochemical cell with: (a) Ni overlayer and (b) Au overlayer.

Imaging mode is first used to obtain spatially resolved XPS spectra for different materials on the electrochemical cell exposed surfaces. Each core-level element appearing in binding energy plot has its corresponding position, so as to identify GDC edges with YSZ and Au (or Ni) respectively. For example, at the Au/GDC interface, as shown in Figure 3.4, the Au4f peaks start to fade, and the Zr3d peaks start to appear at the GDC/YSZ interface. In addition, strong peaks of impurity elements, such as C1s, P2p, and Si2p, appear, possibly from the fabrication process.

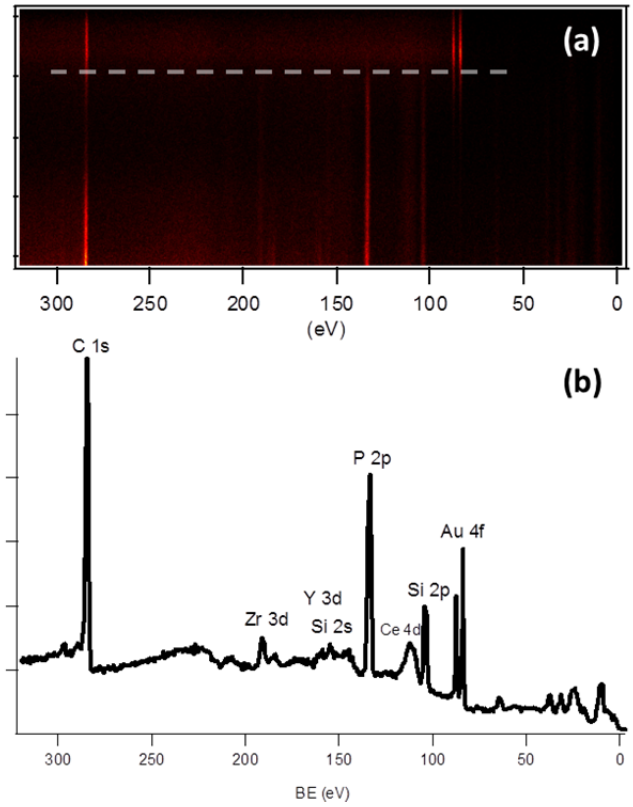

Figure 3.4. Example spatially resolved XPS spectra on GDC surface covering Au edge and YSZ edge. (a) 2-D mapping core-level elements of the electrochemical cell plotted corresponding to binding energy and position, (b) a slice of 2-D XPS mapping spectra at Au/GDC interface labeled in dash line, is plotted binding energy of each element.

The 2-D XPS images are mapped on the O1s spectra along a spatial line across the metal/GDC border and the GDC/YSZ border of the WEs. These scans are conducted at different potential biases (V_{cell}). Relative shifts of the primary local O1s peak with V_{cell} provides a basis for determining the local potential, as described in previous ambient pressure XPS studies on working solid oxide cells [60, 61].

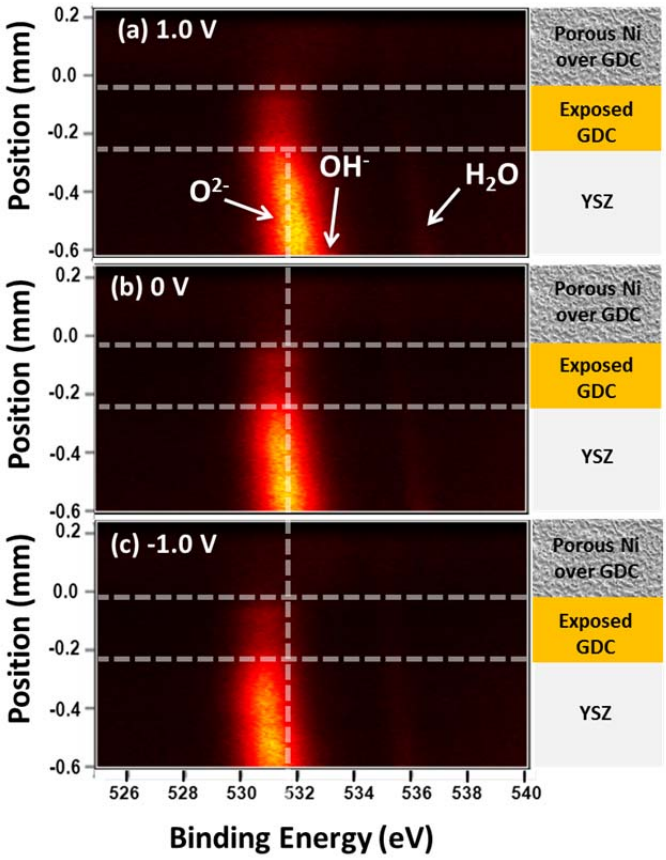

Figure 3.5. 2-D mapping of O1s spectral intensity (with brightness proportional to counts per second) as a function of binding energy and position relative to the edge of the Ni overlayer. Plots are shown for cells operating at $P_{H2} = P_{H2O} = 0.2$ Torr, 620 °C. Plots show that binding energy shift of the O1s peak is associated with local potential change across the exposed Ni/GDC/YSZ edge as a function of three cell biases (V_{cell} = -1.0, 0.0, and 1.0 V)

In Figure 3.5, the 2-D mapping of O1s spectra are plotted as binding energy versus the position along the Ni/YSZ/GDC border. The XPS spectra images are aligned with the cell edges schematic. Brightness of the images indicates intensity of the O1s spectra in unit of counts per second (CPS). As intensity of the O1s spectra on YSZ surface is at least 10 times stronger than those on Ni surface, and the XPS measurement only allows probing ~ 10 nm thickness of sample surface, the O1s 2-D image become dim at GDC surface and completely dark on the Ni surface. The intensity change of the image also provides a reference to the interface borders in the measurement.

There is also an observation of shifts of the binding energy as a function of voltage bias to cell (V_{cell}) on the 2-D mapping. Furthermore, the magnitudes of O1s spectra shifts across Ni/GDC/YSZ edge under the voltage bias are different. These differences are due to different surface potentials as described in Eq.3.2. Thus, analyzing shifts of the O1s spectra of the 2-D mapping provides a measurement for local surface potential. The surface potential differences between specific interfaces (metal/GDC or GDC/YSZ) are referred to as overpotentials associated with interfacial reactions.

By horizontally slicing the 2-D XPS mapping, the O1s spectra are plotted and fitted, as shown in Figure 3.6. The O1s spectra are fitted to Gaussian/Lorentzian line-shapes peaks with Shirley-background corrected using standard XPS data analysis techniques in CasaXPS. The fitted peaks compose of three oxygen-related species:

gas phase water (H_2O) [115], surface hydroxyl (OH^-) [116-118] and oxide ion (O^{2-}) [116, 119].

To quantify the OH^- peak at different positions and conditions, full width half maximum (FWHM) constraints are imposed that the FWHM of OH^- is set to be the same as primary O^{2-} peak. Such a setting makes sure that all the peaks are appropriately offset, and the fitting becomes less sensitive to noise in the data and returns a consistent answer for the relative intensities of the two components. The integrated percentage area for each component is then utilized for the concentration percentage analysis.

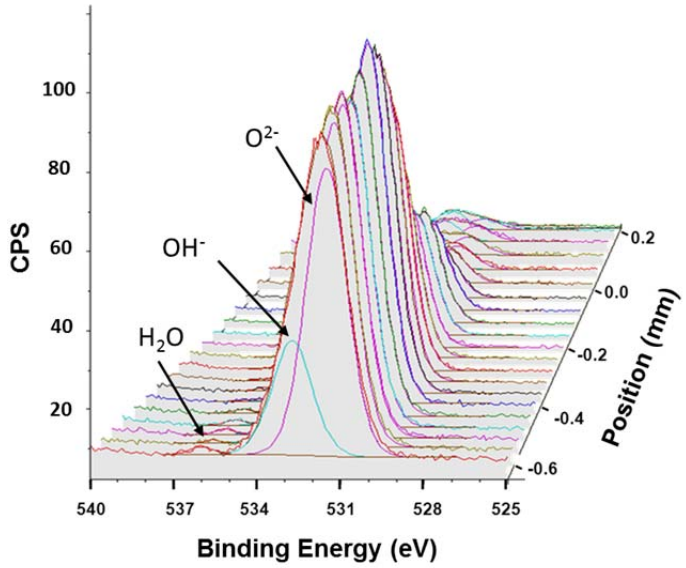

Figure 3.6. Analysis of the O1s spectra by fitting to Gaussian/Lorentzian line-shapes peaks with Shirley-background corrected in CasaXPS (ex. V_{cell} = 1.0 V). The fitted peaks compose of three oxygen-related species: gas phase water (H_2O), surface hydroxyl (OH^-) and oxide ion (O^{2-}).

Primary peak (O^{2-}) binding energies after fitting are plotted as a function of the cell position across the metal/GDC/YSZ border of different V_{cell}. Figure 3.7a and Figure 3.7b plot binding energy along Ni/GDC/YSZ and Au/GDC/YSZ edges respectively. Shift of binding energy of each surface suggests potential change of the surface associated with potential bias. As indicated in the plots, potential shift of GDC surface as well as YSZ surface relative to grounded metal are the difference of binding energies between given bias and those at zero potential state. The results indicate that resistance of charge transfer between the metal current collector and the GDC appears to be relatively small for the positive V_{cell}.

Relatively flat binding energy distribution on the GDC surface (between -0.24 mm and -0.06 mm) suggests sufficient electrical conductivity and thus uniform potential distribution on the GDC edge. Larger *BE* shifts from GDC to YSZ especially for $V_{cell} > 0$ indicate much higher potential difference between GDC and YSZ surfaces. This is possibly due to O^{2-} charge transfer across the interface and/or low O^{2-} mobility of the YSZ bulk close to the interface. The interfacial resistance, as observed, is strongly dependent upon current direction. Compared between Ni/GDC and Au/GDC electrodes, binding energy shifts are similar. Because of larger output currents associated with Ni/GDC electrode, the resistances for Ni/GDC electrode are smaller.

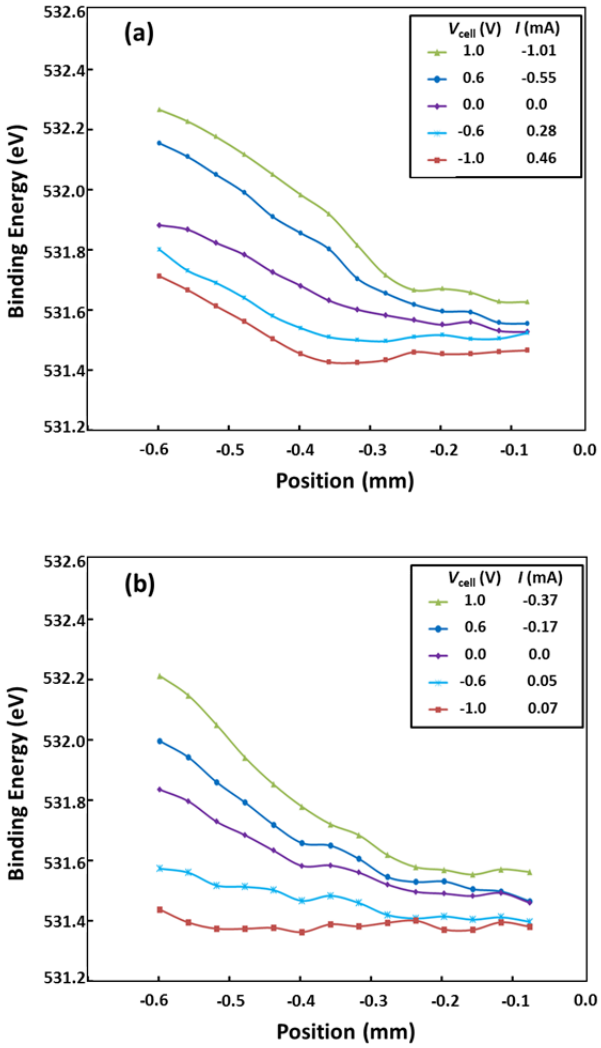

Figure 3.7. Binding energy of O1s primary peak (associated with O^{2-} on the surface) plotted along metal/GDC/YSZ at P_{H2} = P_{H2O} = 0.2 Torr, 620 °C. The shifts of the binding energy of local surface referred as a potential change relative to the OCV condition: (a) GDC with Ni overlayer, plotted from YSZ to GDC (b) GDC with Au overlayer, plotted from YSZ to GDC.

The shifts of the binding energy of each surface refer to as a potential change relative to the OCV condition. Using the binding energy shifts, average potentials of

GDC and YSZ surfaces are plotted in Figure 3.8a of Ni overlayer and Figure 3.8b of Au overlayer, with error bars determined from deviation from average potential of each surface. For Ni/GDC electrode, slightly larger potential increase of GDC surface

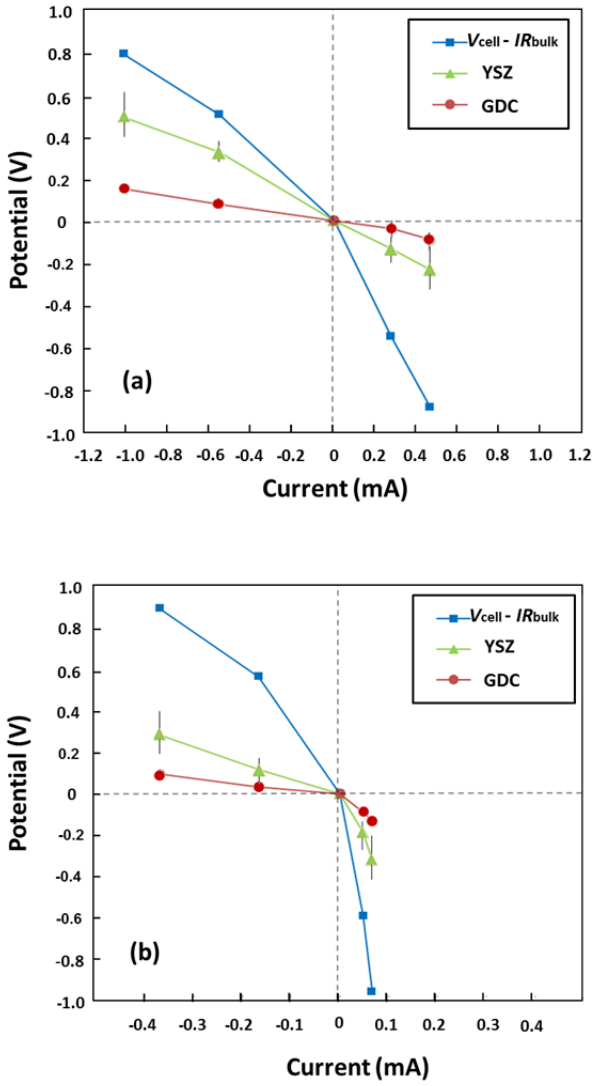

Figure 3.8. Surface electric potential of GDC and YSZ surfaces as well as V_{cell} - IR_{bulk} under the XPS mapping at V_{cell} = 0V, +/- 0.6V, +/-1V at P_{H2} = P_{H2O} = 0.2 Torr, T = 620 °C: (a) Ni-GDC-YSZ and (b) Au-GDC-YSZ. The error bars are determined from deviation from average potential of each surface.

associated with H_2 oxidation (-0.091 V) at 0.46 mA than H_2O electrolysis (0.079 V) at -0.55 mA. From the GDC surface to YSZ, the potential increase on H_2O electrolysis is more significant (~0.1 V greater than H_2 oxidation at 0.46 mA). This larger potential increase associated with H_2O electrolysis is due to relatively hard incorporating O^{2-} from bulk GDC to YSZ phase.

In comparison, potential increase of Au/GDC electrode is more significant than the Ni/GDC electrode at same currents, especially on H_2 oxidation. This suggests the Au/GDC has much lower exchange current density on H_2 oxidation that more potential shift is required to drive reaction (current). Also due to much limited rate of H_2 oxidation at the Au/GDC interface, potentials of other component surfaces are also largely increased.

The charge-transfer reactions across the metal/GDC interface as well as GDC/YSZ interface are analyzed by measuring the overpotentials associated with H_2 oxidation and H_2O electrolysis on the GDC electrode as shown in Figure 3.9. For H_2O electrolysis, interfacial overpotentials of Au/GDC electrode are slightly higher than those of Ni/GDC interface at the same current while much larger overpotentials are observed on the H_2 oxidation reactions Au/GDC electrodes.

Such significantly different behavior on H_2 oxidation is due to Ni providing significant amount of surface H to promote the following charge-transfer reactions.

$$H_{2(g)} + 2(Ni) \leftrightarrow 2H(Ni) \qquad \text{(R.3.1)}$$

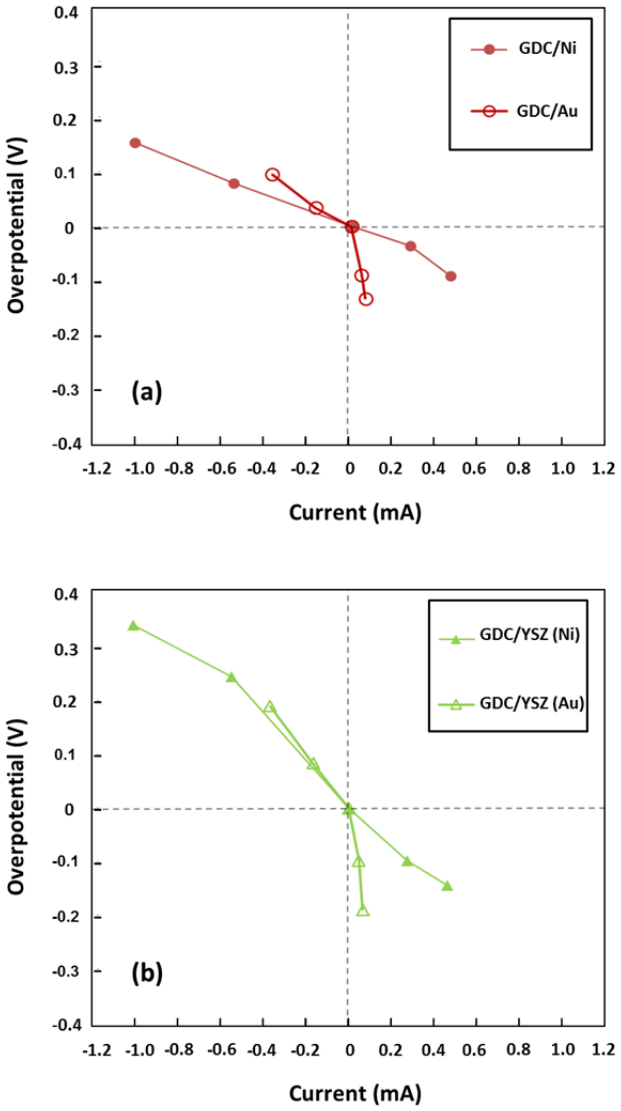

Figure 3.9. Comparison of overpotential associated with GDC interfaces between Ni and Au metal overlayer at $P_{H2} = P_{H2O} = 0.2$ Torr, $T = 620$ °C: (a) metal/GDC and (b) GDC/YSZ.

$$H(Ni) + O^{2-}(GDC) + Ce^{4+}(GDC) \leftrightarrow (Ni) + OH^{-}(GDC) + Ce^{3+}(GDC) \quad (R.3.2)$$

$$H(Ni) + OH^{-}(GDC) + Ce^{4+}(GDC) \leftrightarrow (Ni) + H_2O(GDC) + Ce^{3+}(GDC) \quad (R.3.3)$$

The overall reaction is completed by water desorption and the charge-transfer reaction, both of which are shown here

$$H_2O_{(g)} + (GDC) \leftrightarrow H_2O(GDC) \quad \text{(R.3.4)}$$

$$Ce^{3+}(GDC) \leftrightarrow Ce^{4+}(GDC) + e^{-}(Ni) \quad \text{(R.3.5)}$$

The charge-transfer reaction R.3.5 depends on the mobility of the Ce^{3+} (polaron) on the GDC surface. Different from 700 °C, at temperatures of 600 °C and lower, electron mobility drops significantly, and thus, the extent of active GDC surface will be more and more confined to the metal/GDC interface.

For the Au/GDC electrode, the relatively inactivity of Au for H_2 adsorption implies that H_2 adsorption on the GDC surface will likely play a more critical role for the forward reaction, likely take the following forms

$$H_{2(g)} + 2O^{2-}(GDC) + 2Ce^{4+}(GDC) \leftrightarrow 2OH^{-}(GDC) + 2Ce^{3+}(GDC) \quad \text{(R.3.6)}$$

$$H_{2(g)} + O^{2-}(GDC) + 2Ce^{4+}(GDC) \leftrightarrow H_2O(GDC) + 2Ce^{3+}(GDC) \quad \text{(R.3.7)}$$

Reaction R.3.5 largely depends on the extent of active GDC surface area available for the H_2 oxidation reaction rates for R.3.6 and R.3.7. Thus, the charge-transfer reaction rate is determined by the mobility of the polarons rather than the Au overlayer. The performance will be enhanced at conditions that GDC electronic conductivity is improved such as higher temperatures and lower P_{O2}.

While under positive biases (H_2O electrolysis reaction), the increased potential of the GDC surface will encourage increased oxide vacancies [60, 61]. The increased oxide vacancies likely promote the mobility of the polarons, which facilitates surface oxidation (R.3.6 and R.3.7) and charge-transfer reaction (R.3.5). This is consistent with the observations in Figure 3.9, where under the positive V_{cell} to drive H_2O electrolysis on the metal/GDC, differences of the overpotentials are relatively small between Au/GDC and Ni/GDC electrodes.

In order to identify how the Ni surface chemistry and Ni/GDC interface reaction promote the electrochemistry, a closer look at the Ni/GDC and Au/GDC interfacial species is taken, as shown Figure 3.10a and Figure 3.10b. The Ni/GDC interface has 16.8% (area percentage to the O1s spectrum) of OH^- at V_{cell} = 0 V. For Ni/GDC electrode, OH^- increases ~3.5% at V_{cell} = 1.0 V, and decreases ~ 6% at V_{cell} = -1.0 V. It is evident that OH^- is much involved in H_2 oxidation and H_2O electrolysis at Ni/GDC interface through R.3.2 and R.3.3. The spectroscopic measurements support the hypothesis that Ni/GDC electrode has faster adsorbed H creating and H hopping to GDC, thus facilitates H_2 oxidation.

Compared to Ni, the OH^- concentration on Au/GDC interface is much lower at all three potentials as shown in Figure 3.10b. Much lower OH^- content of Au/GDC interface at 0 V is clearly shown in the figure. At +1.0/-1.0 V, OH^- content increases but still much less than those at Ni/GDC interface. Production of OH^- for both H_2 oxidation and H_2O electrolysis is likely through R.3.6.

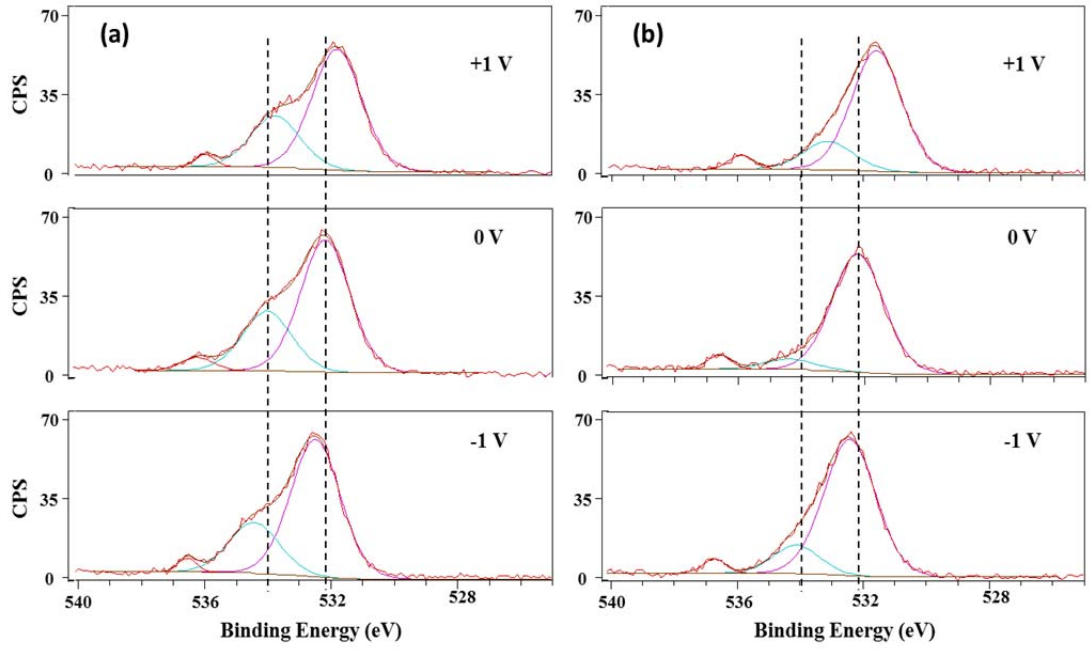

Figure 3.10. Comparison of the fitted O1s spectra at V_{cell} = 0V, +/-1V at $P_{H2} = P_{H2O}$ = 0.2 Torr, 620 °C. The fitted peaks provide surface OH^- content comparison at (a) Ni/GDC and (b) Au/GDC.

Further XPS measurements on O1s are taken at P_{H2}/P_{H2O} = 5/1, T = 620 °C and at P_{H2}/P_{H2O} = 1, T = 570 °C, in order to investigate the GDC surface at different P_{O2} and temperature. Figure 3.11a compares overpotentials of Ni/GDC interface at different temperature and P_{O2}. It is clear that increasing temperature could enhance all reactions listed above. The enhancement is also due to increased mobility of polarons, which to some extent enlarges GDC active surface area. Promotion of both H_2 oxidation and H_2O electrolysis due to increased mobility of polarons is demonstrated at lower P_{O2}, T = 620 °C. At the same temperature, overpotentials of Ni/GDC

interface are largely decreased at lower P_{O2} despite lower H_2O content is used in the test.

Effects of P_{O2} and temperature on bulk GDC are also seen at GDC/YSZ interface as plotted overpotentials versus current, in Figure 3.11b. The overpotential results from different oxide ion incorporation rate at the two oxide-ion conductive phases, simply expressed as the oxide ion charge transfer

$$O^{2-}(\text{YSZ}) + (\text{GDC}) \leftrightarrow (\text{YSZ}) + O^{2-}(\text{GDC}) \qquad \text{(R.3.8)}$$

where forward reaction is driven by the negative potential bias at which H_2 oxidation takes place on the GDC electrode.

Lower overpotential at the negative potential bias suggests that it is easier for oxide ion transport from bulk YSZ to GDC. This is due to much higher ionic conductivity in the GDC than in bulk YSZ. This is also seen when temperature rises from 570 °C to 620 °C that ionic of both phases are increased thus much lower overpotential is observed at the interface. Moreover, the overpotential associated with R.3.8 is also decreased at lower P_{O2}. The possible reason is that the increased electronic (polaron) conductivity spreads out the reaction over the GDC and thereby permits lower currents density at the YSZ/GDC interface.

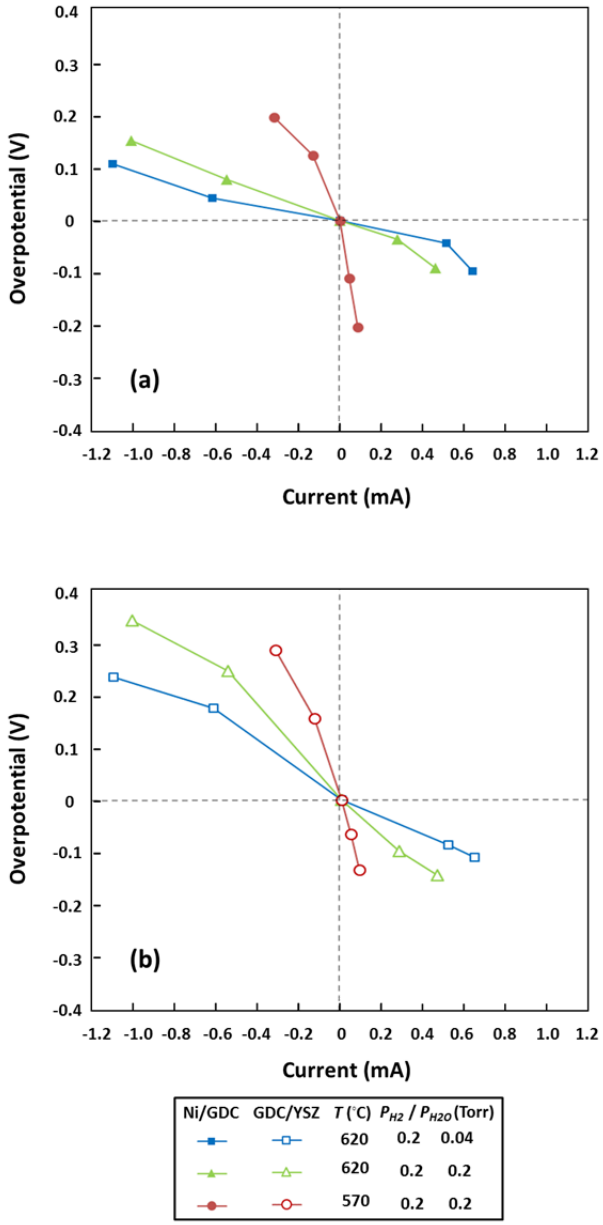

Figure 3.11. Effects of P_{O2} and temperature on overpotentials of (a) Ni/GDC and (b) YSZ/GDC interfaces.

Results on OH^- concentration changes at Ni/GDC interface according to potential bias discussed above demonstrate the importance of OH^- in the charge-transfer reaction. Therefore, OH^- content charges are further studied in order to have a

quantitative assess on how the surface active species are related to the reactions. Figure 3.12 shows dependency of OH^- area percentage at Ni/GDC interface as a function of V_{cell} at different operation conditions.

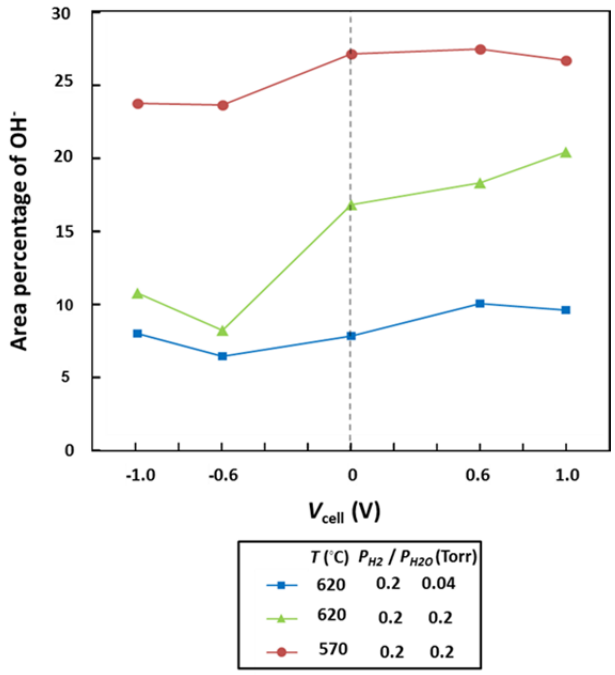

Figure 3.12. Dependency of OH^- content of Ni/GDC interface plotted in area percentage of the total O1s spectra as function of V_{cell} at different operation conditions.

The surface fractions of OH^- on the GDC at equilibrium (V_{cell} = 0) vary strongly with gas environments. Interestingly, the lower temperature case and the higher H_2O gaseous content lead to higher OH^- concentrations. The OH^- intensity changes when reactions R.3.2 and R.3.3 begin to take place under bias. The area percentage of OH^- plots show that OH^- surface fractions decrease during the H_2

oxidation reaction (V_{cell} < 0). While during H_2O electrolysis, the OH^- intensity is slightly higher or closer to V_{cell} = 0 [118]. The measurable OH^- intensity difference between H_2 oxidation and H_2O electrolysis provides evidence that reaction rates of R.3.2 and R.3.3 are different and OH^- participates in the rate-limiting reactions.

3.4.2 AP-XPS Measurement of Ni/GDC Electrode on CO/CO_2 Reactions

In addition to H_2/H_2O studies, investigation of CO/CO_2 electrochemistry on Ni/GDC electrodes is taken in order to compare CO oxidation with H_2 oxidation on the Ni/GDC electrode. The electrochemical cell is cooled down to room temperature after the H_2/H_2O tests. The main chamber is then pumped down to ultrahigh vacuum (~10^{-7} Torr) to remove absorbed water vapor from the cell surfaces and the chamber wall. After these procedures, CO_2 and CO are refilled into the chamber. The cell is reheated to 620 °C (using same heating current as H_2/H_2O at 620°C).

O1s spectra from 2-D mapping of Ni/GDC/YSZ edges are analyzed to acquire information on local surface potential and surface reactive species. Figure 3.13 shows 2-D images of the O1s spectra at equilibrium potential (V_{cell} =0), exposed to (a) 1:1 and (b) 1:9 mixtures of CO and CO_2 at 0.4 Torr total pressure, respectively. The O1s spectra compose three oxygen-related species: gas phase carbon dioxide (CO_2) [120], surface carbonate (CO_3^{2-}) [121, 122], and oxide ion (O^{2-}). Gas phase CO is only observed beside CO_2 peak [123, 124] under the 1:1 mixture environment but not under the 1:9 mixture environment.

At both CO/CO_2 ratios, CO_3^{2-} peaks are weak on the exposed GDC surface. Depletion of CO_3^{2-} in several hundred μm wide of electrochemically active region is also observed on undoped ceria electrochemical cell studies during CO_2 electrolysis [64]. The small CO_3^{2-} concentration on the surface at equilibrium potential state suggests GDC is less likely to adsorb carbon-based species. This may explain why SOFC anodes with GDC are more resistant to carbon deposition for hydrocarbon fuels.

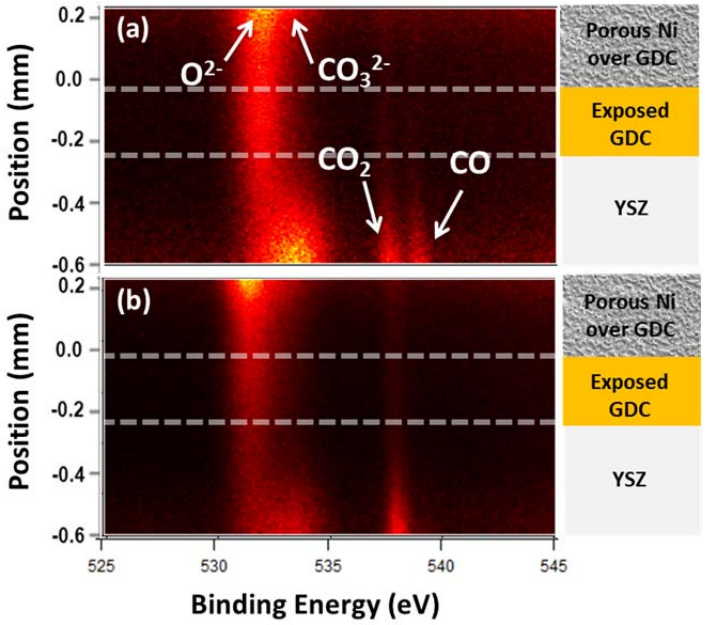

Figure 3.13. 2-D images of the O1s spectra at equilibrium potential ($V_{cell} = 0$). The cell is exposed to (a) $P_{CO} = P_{CO2} = 0.2$ Torr, and (b) $P_{CO} = 0.04$ Torr / $P_{CO2} = 0.36$ Torr at 620 °C.

In order to quantify the CO_3^{2-} peak at different positions and conditions, the O1s spectra are plotted and fitted by horizontally slicing the 2-D XPS mapping, , as

shown in Figure 3.14. Still the FWHM of CO_3^{2-} is set to be the same as primary O^{2-} peak. The integrated area percentage for each component is then utilized for the concentration percentage analysis.

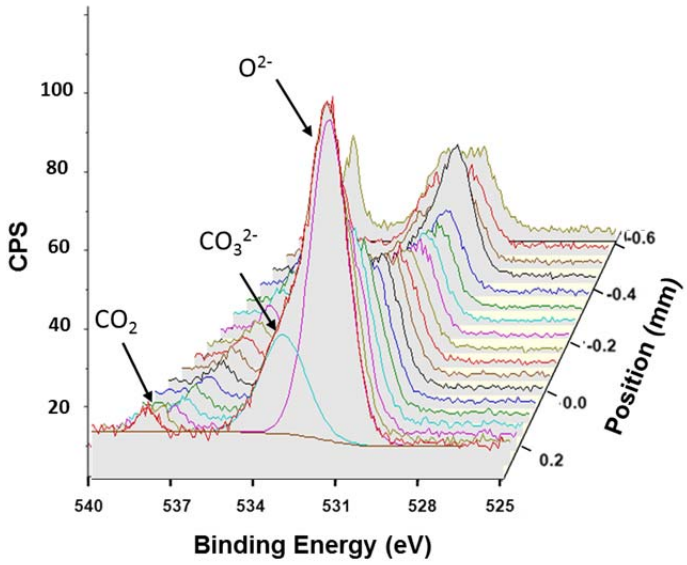

Figure 3.14. Analysis of the O1s spectra (V_{cell} = 0 V) by fitting to three oxygen-related species: gas phase carbon dioxide (CO_2), surface carbonate (CO_3^{2-}), and oxide ion (O^{2-}), at P_{CO} = 0.04 Torr/P_{CO2} = 0.36 Torr, T = 620 °C.

Considering the fact that very low CO_3^{2-} concentrations are on the GDC surface, presence of CO_3^{2} peaks at interface at Ni/GDC interface is primarily due to the interaction between Ni surface species and GDC surface. The reaction processes could be described as

$$CO_{(g)} + (Ni) \leftrightarrow CO(Ni) \qquad \text{(R.3.9)}$$

$$CO_{2(g)} + (Ni) \leftrightarrow CO_2(Ni) \qquad \text{(R.3.10)}$$

$$CO(Ni) + 2O^{2-}(GDC) + 2Ce^{4+}(GDC) \leftrightarrow (Ni) + CO_3^{2-}(GDC) + (GDC) + 2Ce^{3+}(GDC) \quad \text{(R.3.11)}$$

$$CO_2(Ni) + O^{2-}(GDC) \leftrightarrow (Ni) + CO_3^{2-}(GDC) \quad \text{(R.3.12)}$$

While direct formation of CO_3^{2-} on the GDC surface through R.3.13 may not be significant due to low intensity of CO_3^{2-} peak on the GDC surface

$$CO_{2(g)} + O^{2-}(GDC) \leftrightarrow CO_3^{2-}(GDC) \quad \text{(R.3.13)}$$

To obtain a quantitative analysis of the relative surface CO_3^{2-} coverage at Ni/GDC interface, area percentages of CO_3^{2-} relative to the total O1s spectra at different CO/CO_2 ratios are plotted as function of V_{cell} in Figure 3.15. Coverage of CO_3^{2-} increases when high CO_2 content feeding to the main chamber. Increasing P_{CO2} promotes surface absorption of CO_2 (R.3.10) thus increases CO_3^{2-} formation (R.3.12).

At the same gas environment, surface CO_3^{2-} fraction slightly increases at positive potential bias when CO_2 electrolysis takes place on Ni/GDC electrode, while significant concentration drops (~ 30- 40%) at negative potential during CO oxidation. This is consistent with the observation in CO/CO_2 kinetics study results and the interpretation of CO_3^{2-} as an intermediate surface reactive species involving with both reactions [64]. The less CO_3^{2-} concentration change during CO_2 electrolysis may be also due to enhanced mobility of GDC surface at positive potential bias. The surface CO_3^{2-} concentration change may also be affected by the overlapping SiO_2 peak which has been suggested increase with the passage of time regardless of applied biases [64].

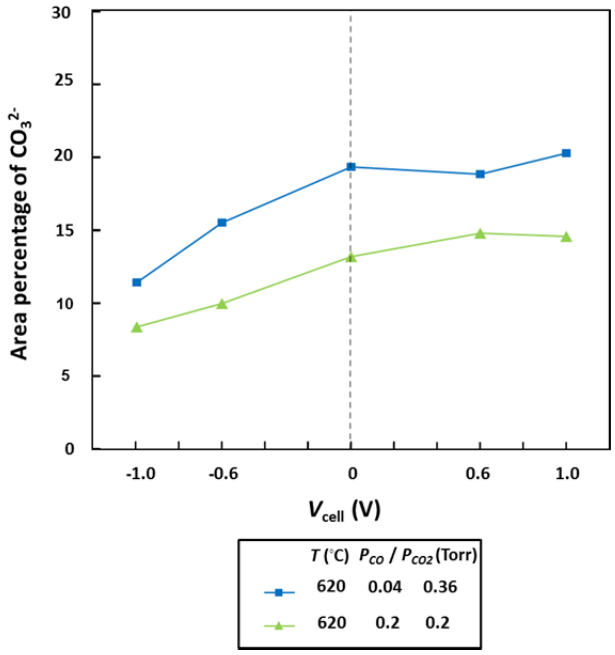

Figure 3.15. Dependency of CO_3^{2-} content of Ni/GDC interface plotted in area percentage of the total O1s spectra as function of V_{cell} at different operation conditions: P_{CO} = 0.2 Torr and P_{CO2} = 0.2 Torr vs. P_{CO} = 0.04 Torr and P_{CO2} = 0.36 Torr, at 620 °C.

Furthermore, overpotentials at Ni/GDC interface with H_2/H_2O and CO/CO_2 reactions are compared at similar conditions as shown in Figure 3.16a. Much larger overpotentials on CO/CO_2 reaction at the interfaces confirm that electrochemical oxidation of H_2 or electrolysis of H_2O is much faster. And this also confirms that for CO/H_2O mixture, H_2 oxidation/H_2O electrolysis dominates the charge-transfer reactions corresponding to potential bias.

The GDC/YSZ interface overpotentials are also significantly increased for CO/CO_2 reactions, despite lower P_{O2} at CO/CO_2 mixture. The higher overpotentials

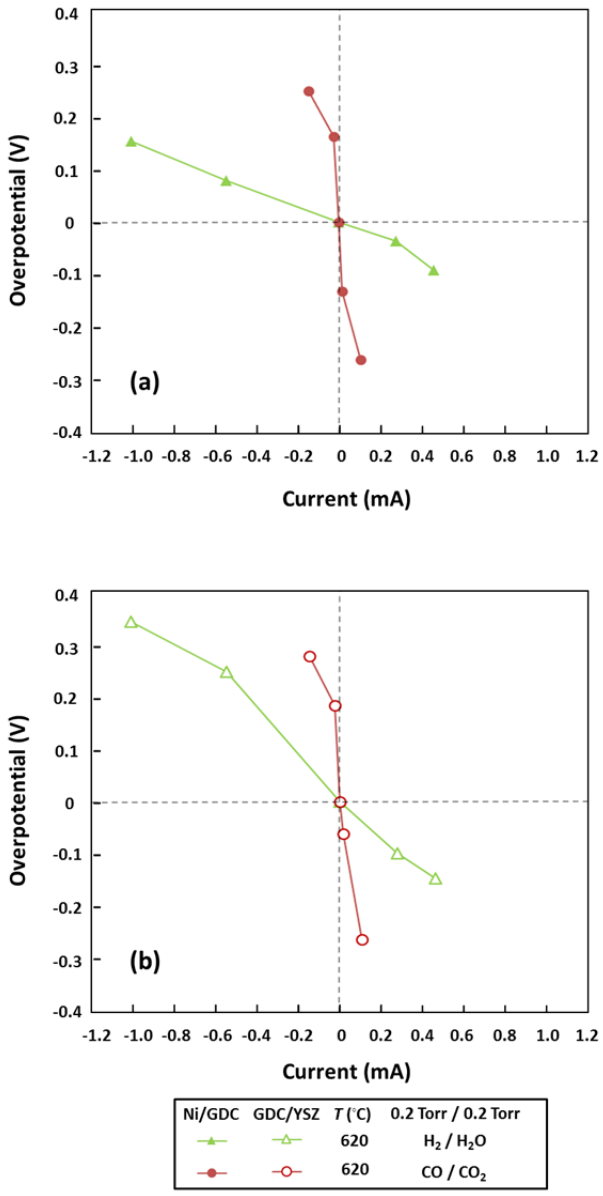

Figure 3.16. Comparison of overpotentials at (a) Ni/GDC and (b) GDC/YSZ interfaces of H_2 oxidation and CO oxidation on the GDC electrode, operating at P_{CO} = P_{CO2} = 0.2 Torr and P_{H2} = P_{H2O} = 0.2 Torr, at 620 °C.

are possibly due to slower charge-transfer reactions at the Ni/GDC interface that reduce the active GDC surface area and therefore reduce the area across the GDC/YSZ interface over which oxide ions are conducted.

3.5 Conclusions

AP-XPS measurements of active GDC electrode surface during H_2/H_2O and CO/CO_2 reactions provides a means to study local surface potential through shift of characteristic binding energy, thereby determines overpotentials of the GDC interfaces associated with charge-transfer reaction. Results reveal lower overpotentials associated with H_2O (or CO_2) electrolysis reactions than H_2 (or CO) oxidation on GDC electrodes at the same current magnitudes. Ni/GDC electrode superior to Au/GDC electrode largely promotes H_2 oxidation, and significantly decreases interface overpotentials.

Investigation of O1s core-level spectra of the GDC electrodes at H_2/H_2O atmosphere reveals that surface OH^- plays an important role in the charge-transfer reaction in H_2/H_2O electrochemistry. The increased OH^- concentration governs the reaction rate resulting in faster reaction rate of GDC with Ni overlayer than with Au overlayer. Higher OH^- content on Ni/GDC surface demonstrates that Ni promotes H_2 spillover and interacts with GDC surface. Such surface OH^- content and interfacial overpotential results associated with the charge-transfer reaction provide quantitative information on the GDC kinetic development.

CO/CO_2 reactions are also investigated by analyzing O1s core-level spectra of the GDC electrodes. Surface CO_3^{2-} is involved in the charge-transfer reaction of CO oxidation and CO_2 electrolysis that the CO_3^{2-} content is close related to the reaction direction. Carbon-based species cover on Ni/GDC interface despite the fact that most of CO_3^{2-} is depleted at reaction active region of the GDC surface. Much higher overpotentials associated with CO oxidation indicate much slower charge-transfer reaction rate than H_2 oxidation.

The experimental studies performed above demonstrate that *in operando* AP-XPS is a novel technique for studying active GDC electrode during its operation. Analyzing data collected from XPS studies provides detailed kinetic information on intermediate surface species and overpotentials associated with the charge-transfer reactions. Such quantitative measurements help on development of GDC electrode kinetic model in Chapter 4.

Chapter 4: One Dimensional Model on Electrochemistry of GDC Electrodes

Simultaneous electrochemical characterization and ambient pressure XPS measurements in the preceding sections provide quantitative kinetic information of GDC electrode in the reactions. Surface species and interface overpotentials shown in the experimental results are closely related to the surface reactions and charge-transfer reactions processes expressed in R.3.1 - R.3.7 and R.3.9 - R.3.12. The different behaviors of Ni/GDC and Au/GDC electrodes provide significant insight into the nature of the charge-transfer reactions associated with the GDC and metal surfaces as discussed in Chapter 3. Nonetheless, limited quantitative information about elementary reactions exists for the metal/GDC electrodes. The lack of fundamental mechanism of simple H_2 or CO electro-oxidation on the GDC surface motivates current modeling effort to develop an oxidation mechanism for commonly studied Ni/GDC SOFC anodes.

This chapter presents the development adequate thermodynamic and kinetic parameters to model the charge-transfer and other reactions on the Ni/GDC electrode to complement the experimental studies. A 1-D isothermal model is implemented to simulate thin-film GDC electrochemical cell in the experimental environments. The model focuses on charge transport in bulk GDC and surface and charge-transfer reactions associated with the GDC electrode. In the model, sequential reactions

described in Chapter 3 are quantified with kinetic parameters. Comparisons between model predictions and the XPS measurements provide some level of confidence in the proposed kinetic mechanism. The kinetic model provides the basis for IT-SOFC modeling efforts involving GDC-based anodes as discussed in Chapter 5.

4.1 Previous SOFC Kinetic Modeling

A number of kinetic modeling studies have been taken on MIEC cathodes. Deseure et al. used one-dimensional thin-film MIEC model to explore surface exchange and bulk diffusion of LSC electrode by fitting to polarization curves and impedance spectra. The study has suggested both solid state diffusion and incorporation of adsorbed oxygen are rate-limiting processes oxygen reduction reaction [125]. Further MIEC modeling study conducted by Mebane and others, revealed competition between surface exchange reaction and bulk processes in LSM thin-film electrodes [87]. Multi-dimensional studies of LSCF cathode current distributions have revealed the surface reaction rate of the MIEC cathode largely depends on material parameters and microstructures [126, 127]. Most of the electrochemical reaction takes place close to the LSCF/electrolyte/gas TPB, although O_2 reduction can occur on the LSCF surface further from the TPB due to the ability for the LSCF to transport electrons to the reaction site [128]. This is similar to the observation of reactions on Ni/GDC electrode in current study that higher polaron mobility extends reactions to the GDC surface while lower polaron mobility limits the charge-transfer reaction close to Ni/GDC interface.

Early kinetic models on GDC included ionic and electronic transport exposed to the P_{O2} gradient between anode and cathode. Riess derived analytic expression for ionic and electronic currents and experimentally measured potential distribution in the GDC at low oxygen pressures with a fixed concentration boundary conditions and reversible electrodes [129-131]. Chan et al. also modeled distribution of electron concentration and potential across a GDC electrolyte thickness [132]. Experiments on electronic and ionic conductivity have described their dependency on P_{O2} using an ideal-solution model [53]. Bishop et al. measured and modeled non-stoichiometry and conductivities in GDC exposed to low P_{O2} characteristic of SOFC anodes [54, 55, 133]. Charge transport formulations from these previous GDC bulk studies are utilized in the current modeling effort.

Only a few researchers have investigated GDC electrode kinetics associated with fuel oxidation reactions. Green et al. derived the CO/CO_2 exchange kinetics on GDC using exchange electrode model to fit impedance measurement data [57]. However, this approach is only applicable to a small current perturbation from electrode equilibrium. Duncan et al. used continuum-level electrochemical model to extract kinetic parameters on H_2 oxidation, such as exchange current density from experimental *V-I* curves, and provided a means to determine overpotential associated with reaction rate (current) [134, 135]. They pointed out potential-dependent defect concentration and irreversible electrode behaviors of redox reactions at reacting GDC interface. The potential-dependency of defect concentration has been observed with *in operando* XPS measurements of undoped ceria thin-film electrodes during H_2/H_2O

reactions [60, 61]. The charge-transfer reactions at metal/GDC interface affect surface species concentrations including local defect concentrations.

Goodwin et al. have made significant contributions on elucidating elementary steps in H_2 oxidation kinetics across Ni/YSZ three-phase boundaries including the charge-transfer reactions [9, 66, 136]. A similar approach is used in the current study to address the complications of the MIEC behavior of the GDC electrode. The MIEC behavior of GDC like other ceria-based electrodes provide expands charge-transfer reactions to areas on GDC surface away from metal current collectors [61, 64, 137]. The current modeling incorporates both ionic and electronic fluxes on the GDC electrode to capture the potential for extending the regions of charge-transfer reactions over the GDC surface.

4.2 Model Formulation

4.2.1 Model Description

The one-dimensional modeling of the GDC electrochemical cell assumes relatively one-dimensional charge fluxes and constant temperature as expected in the experimental studies. Figure 4.1 depicts the model geometry that attempts to capture charge transport and surface chemistry. Like the experiments, the GDC thin-film electrode (300 nm thick) sits on a 1-mm thick YSZ membrane. A porous Ni overlayer (100 nm thick) partially covers the GDC surface. The porous structures allow gas accessing to GDC thin-film surface and create three-phase boundaries (TPB) between the GDC, Ni, and gas phases.

A porous Pt CE (100 nm) on the backside of the 1-mm YSZ disk provides sufficient TPB to facilitate charge-transfer reactions as a counter electrode. The Pt/YSZ interfacial overpotential contributing to the overall cell performance is accounted. Since the cell is tested in a single-chamber, both Ni/GDC WE and Pt CE are modeled in the same gas composition, temperature, and pressure.

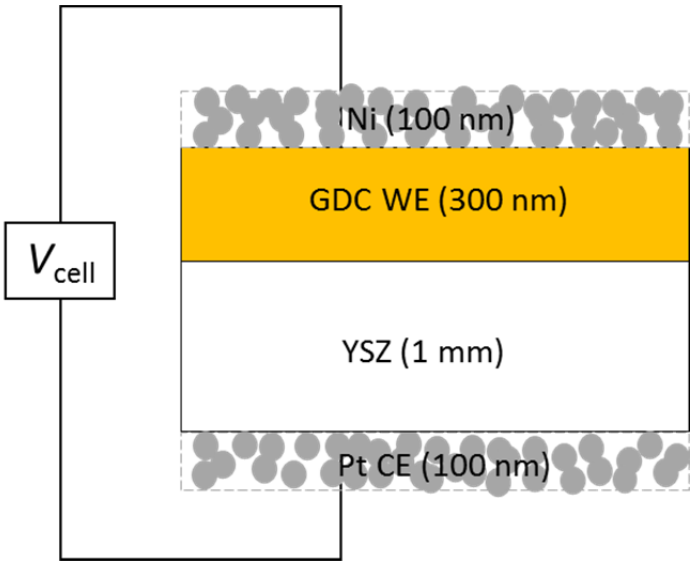

Figure 4.1. Schematic of 1-D kinetic model geometry of thin-film GDC electrochemical cell (YSZ thickness is not to scale).

The kinetic model employs physical conservation laws converted to partial-differential algebraic equations (DAE). The model equations with spatial discretizations are approximated with second-order numerical expressions using a finite volume method, and time derivatives are integrated with a stiff ode integrator. The following physical phenomena are included in the model:

- convective-diffusive transport from the test chamber to the porous medium;
- gas-phase diffusion through the porous metal overlayers;

- reversible surface reactions with thermodynamically consistent rate parameters;
- charge-transfer reactions at the GDC surface and Ni/GDC interfaces;
- charge transport in the bulk oxides.

The DAE system is solved using MATLAB with the ode15s function. Simulations integrate, with respect to time, the coupled DAE system of equations at a given external current density (i_{ext}) until the steady-state cell potential (V_{cell}) is reached. Integration over a range of current densities provides a *V-I* curve for the cell that can be compared to the experimental measurements in previous chapters. As with the experiments, the porous Ni is grounded, and V_{cell} is Pt CE potential. The spatial discretization allows the model to provide local surface potentials to compare with those acquired in the XPS measurements.

4.2.2 Governing Equations

The 1-D isothermal SOFC model is based on integrating DAE to solve state space variables relevant for each cell including a uniform boundary gas-phase cell. The state variables are as follows: ρ (gas density), Y_k (gas mass fractions), $\theta_{k,m}$ (surface species k site fraction on phase m), $X_{k,m}$ (bulk molar fraction in phase m), and Φ_m (electrical potential in phase m).

The current model incorporates surface and electrochemical reaction using elementary reaction kinetics like some previous models for Ni/YSZ [9] and

LSM/YSZ electrodes [73]. The reaction rates are represented through fundamental mass-action kinetics which are calculated with the Cantera software package [91] embedded into MATLAB. Cantera is an object-oriented suite of software tools for problems involving chemical kinetics, thermodynamics, and/or transport processes.

In Cantera, the net rate of species production per unit area $\dot{s}_k$ for gas phase species, surface catalyst species, and bulk species depends upon summing the rate-of-progress q_i over all reactions expressed as

$$\dot{s}_k = \sum_i \left(\nu_{i,k} q_i\right) \qquad \text{(Eq. 4.1)}$$

where $\nu_{i,k}$ is the stoichiometric coefficient of species k in reaction i. The rate-of-progress q_i is evaluated as

$$q_i = k_{i,\mathrm{f}} \prod_{k=1}^{K} [X_k]^{\nu_{i,k,\mathrm{f}}} - k_{i,\mathrm{b}} \prod_{k=1}^{K} [X_k]^{\nu_{i,k,\mathrm{b}}} \qquad \text{(Eq. 4.2)}$$

where $k_{i,\mathrm{f}}$ and $k_{i,\mathrm{b}}$ are forward and backward reaction coefficients respectively. For reversible reactions, backward reaction coefficients are evaluated in Cantera using forward-reaction rate coefficients and thermodynamics properties. $\nu_{i,k,\mathrm{f}}$ and $\nu_{i,k,\mathrm{b}}$ are stoichiometric coefficients of species k in the forward and backward directions respectively. The forward and backward reaction stoichiometric coefficients are defined in Cantera input file in a reaction form. $[X_k]$ is the activity of species involved in the reaction.

For gaseous species adsorption/desorption reactions, the forward reaction rate coefficients are calculated as sticking coefficients

$$k_{i,\mathrm{f}} = \frac{s^0}{\Gamma_m^v}\sqrt{\frac{\bar{R}T}{2\pi W_{k,g}}} \qquad \text{(Eq. 4.3)}$$

where s^0 is the sticking probability and Γ_m is available surface site density. And for other surface reactions, the forward reaction rate coefficients are described in Arrhenius form

$$k_{i,\mathrm{f}} = A_{i,\mathrm{f}} T^{\beta} \exp\left(-\frac{E_{a,i,\mathrm{f}}}{\bar{R}T}\right) \qquad \text{(Eq. 4.4)}$$

As for charge-transfer reactions, the anodic and cathodic rates also depend upon the electric-potential difference across the double layer at the interface [66, 136] as derived in the following relation

$$k_{\mathrm{f,ct}} = k_{i,\mathrm{f}} \exp\left(-\frac{(1-\alpha) z_k F}{\bar{R}T}\eta\right) \qquad \text{(Eq. 4.5)}$$

$$k_{\mathrm{b,ct}} = k_{i,\mathrm{b}} \exp\left(\frac{\alpha z_k F}{\bar{R}T}\eta\right) \qquad \text{(Eq. 4.6)}$$

where η is overpotential (or interfacial potential difference) associated with the charge-transfer reactions. When potential bias is applied to the electrochemical cell, interfacial potential difference increases to drive the charge-transfer reactions until charge-transfer current density satisfies external current density. The charge-transfer current density (i_{Far}) is expressed as

$$i_{\mathrm{Far}} = l_{\mathrm{TPB}}\, z_k F \left(k_{\mathrm{f,ct}} \prod_{k=1}^{K} [X_k]^{\nu_{k,\mathrm{f}}} - k_{\mathrm{b,ct}} \prod_{k=1}^{K} [X_k]^{\nu_{k,\mathrm{b}}} \right) \qquad \text{(Eq. 4.7)}$$

where l_{TPB} is length of three-phase boundary per unit area of GDC electrode in m/m^2.

Gas-phase mass and species conservation are considered in the model. The reacting gases are modeled as ideal gases [9] with the gaseous state assumed to be uniform and described by the given temperature T and the state variables ρ and Y_k. Continuity provides a differential equation for ρ

$$\varphi_g \frac{\partial \rho}{\partial t} = \sum_{k=1}^{K_{gas}} \left(-\nabla J_{k,g} + W_{k,g} \sum_{m=1}^{M} \left(a_m \dot{s}_{k,g,m} \right) \right) \qquad \text{(Eq. 4.8)}$$

where a_m is the surface area of active phase m per unit volume of porous media. $W_{k,g}$ is molecular weight of the gas species. For the Y_k of gas-phase reactants (such as H_2/ H_2O, or CO/CO_2) is given by

$$\varphi_g \rho \frac{\partial Y_k}{\partial t} = -\nabla J_{k,g} + W_{k,g} \sum_{m=1}^{M} \left(a_m \dot{s}_{k,g,m} \right) - Y_k \sum_{k=1}^{K_{gas}} \left(-\nabla J_{k,g} + W_{k,g} \sum_{m=1}^{M} \left(a_m \dot{s}_{k,g,m} \right) \right) \qquad \text{(Eq. 4.9)}$$

The sum of the Y_k is forced to 1, and thus the mass fraction of final gas-phase species is solved by Eq. 4.10

$$\sum_{k=1}^{K_{gas}} Y_k = 1 \qquad \text{(Eq. 4.10)}$$

In Eq.4.8 and Eq.4.9, $\dot{s}_{k,g,m}$ are molar production rates per unit area from surface reactions either on the Ni metal or GDC surface calculated from Eq.4.1. $J_{k,g}$ in Eq.4.8 and Eq.4.9 are the gas-phase mass fluxes to/from the surface per unit area governed by multicomponent diffusion as described in Eq.4.11

$$J_{k,g} = -W_{k,g} \sum_{k=1}^{K_{gas}} (D_{kl} \nabla [X_k]) \qquad \text{(Eq. 4.11)}$$

where $[X_k]$ is the molar concentration of gas-phase species.

Surface species determine reaction rate as formulated in Eq.4.2, and in turn, reactions produce/consume involved surface species. For example, H_2/H_2O reaction at Ni/GDC interface involves species on Ni surface (H(Ni), H_2O(Ni), OH(Ni), and (Ni)) and species on GDC surface (OH^-(GDC), O^{2-}(GDC), H_2O(GDC), and (GDC)). The active surfaces are represented by the surface species molar fractions. Therefore, the conservation equations for $\theta_{k,m}$ are integrated as

$$\frac{\partial \theta_{k,m}}{\partial t} = \frac{1}{\Gamma_{\text{surf,m}}} \left(\dot{s}_{k,m} + \frac{l_{TPB}}{a_m} \dot{s}_{k,m,TPB} \right) \qquad \text{(Eq. 4.12)}$$

where $\dot{s}_{\text{k,m}}$ and $\dot{s}_{k,m,TPB}$ represent the molar production rates of surface species through surface reactions and charge-transfer reactions, respectively. $\Gamma_{\text{surf,m}}$ is available surface site density. $[X_k]$ in Eq.4.2 represents surface site density occupied by species k, expressed as

$$\theta_{k,m} = \frac{[X_k]}{\Gamma_{\text{surf,m}}} \qquad \text{(Eq. 4.13)}$$

The $\theta_{k,m}$ sum to 1 for each phase and the final species for each phase (usually the open surface site) is solved by the summation equation.

$$\sum_{k=1}^{K_{\mathrm{surf,m}}} \theta_{k,m} = 1 \qquad \text{(Eq. 4.14)}$$

Bulk GDC properties and composition vary with both T and effective P_{O2}. Two species (O^{2-}(GDC) and (GDC)) represent oxide ions and oxygen vacancies in bulk-phase GDC. Molar fraction bulk species $X_{k,\mathrm{GDC}}$ is calculated through

$$\frac{\partial X_{k,\mathrm{m}}}{\partial t} = \frac{-\nabla J_{k,\mathrm{m}}}{\Gamma_{\mathrm{bulk,m}}} \qquad \text{(Eq. 4.15)}$$

where $\Gamma_{\mathrm{bulk,m}}$ is available bulk density, and $J_{k,\mathrm{m}}$ represents molar flux of oxygen vacancies or O^{2-} ions in the solid phase per unit geometric area. $[X_k]$ in Eq.4.2 represents bulk density occupied by species k as

$$X_{k,m} = \frac{[X_k]}{\Gamma_{\mathrm{bulk,m}}} \qquad \text{(Eq. 4.16)}$$

The $X_{k,m}$ sum to 1 solved by the summation equation

$$\sum_{k=1}^{K_{\mathrm{bulk,m}}} X_{k,m} = 1 \qquad \text{(Eq. 4.17)}$$

In bulk GDC, the charge transport is driven by electrochemical potential gradients , as described by the Nernst-Planck equation [134]

$$J_k = -D_k \nabla[X_k] - F z_k u_k [X_k] \nabla \Phi_m \qquad \text{(Eq. 4.18)}$$

where u_k is mobility, z_k is the electric charge associated with the charge carriers (ex. O^{2-}(GDC) and Ce^{3+}(GDC)). Φ_m is electric potential in phase m.

The external current density (i_{ext}) of mixed ionic and electronic conducting GDC is given by

$$i_{\text{ext}} = \sum_k F z_k J_k \qquad \text{(Eq. 4.19)}$$

And local charge neutral is maintained, assuming that electrons are localized on the cerium cations to form polaron [138, 139], given by

$$\sum_{k=1}^{n} z_k [X_k] = 0 \qquad \text{(Eq. 4.20)}$$

For pure electronic conducting metal (Ni or Pt) or oxide ion conducting YSZ in this study, the current density is expressed in Ohm's Law

$$i_k = -\sigma_{k,m} \nabla \Phi_m \qquad \text{(Eq.4.21)}$$

where i_k is current density on a per geometric area basis and $\sigma_{k,m}$ is conductivity associated charge transport (either electron or oxide ion).

At the interface, where charge-transfer reactions take place, the electric potential difference (η) between two surfaces is calculated according to the capacitance relationship. The currents in and out of a given finite volume act as charge sinks and sources, respectively.

$$C_{dl}\frac{\partial \eta}{\partial t} \pm \frac{\partial}{\partial y}\left(\sigma_{k,m}\frac{\partial \Phi_m}{\partial y}\right) = l_{\mathrm{TPB}} i_{\mathrm{Far}} \qquad \text{(Eq. 4.22)}$$

where C_{dl} is the double layer capacitance per unit volume, i_{Far} is the Faradaic current per unit TPB length crossing the phase interface from Eq.4.7. The $\pm$ sign on left hand side of Eq.4.22 depends on anodic or cathode current in phase m.

4.2.3 Thermochemistry Model for Phases

Thermokinetic model formulation of reactions in Eq.4.2 makes use of mass-action kinetics, and thermodynamic properties are defined in NASA polynomials as a function of temperature. The mass-action kinetics assumes relatively dilute solid solutions and no interaction between defect species. The change of partial Gibbs free energy is only contributed by variations in species concentration in terms of configurational entropy. This is computationally convenient and accurate at low degrees of reduction of Ce^{4+} in GDC. However, previous studies have shown significant non-ideal defect interactions between defects in GDC as degree of ceria reduction increases [54, 55]. Thermodynamics investigations of oxygen exchange reaction (R.1.6) on pure ceria and GDC have been carried out to study oxygen deficiency related to P_{O2} at a range of SOFC operation temperatures [52, 68].

In order to accurately calculate for GDC-related reactions, thermodynamics of the non-ideal defect interactions must be included. The difference between ideal and non-ideal calculations of partial free energy of formation (per mole O) is defined as

excess free energy in the following equation. To get excess free energies specifically for the GDC electrode, the following free energy relationship is used

$$\Delta\bar{G}_O = 0.5\bar{R}Tln\left(\frac{P_{O2}}{P^0}\right) = -\left(\bar{G}_{\mathrm{Ce}'_{\mathrm{Ce}}} - \bar{G}_{\mathrm{Ce}^{\mathrm{x}}_{\mathrm{Ce}}} + 0.5\bar{G}_{O_{2@P^0}} + \bar{G}_{\mathrm{ex}}\right) \quad \text{(Eq. 4.23)}$$

where $\Delta\bar{G}_0$ is partial free energy of formation (per mole O), $\bar{G}_{\mathrm{Ce}'_{\mathrm{Ce}}}$, $\bar{G}_{\mathrm{Ce}^{\mathrm{x}}_{\mathrm{Ce}}}$, are Gibbs free energy of reduction state and oxidation state respectively, $\bar{G}_{O_{2@P^0}}$ is standard ideal gas Gibbs free energy of O_2, and $\bar{G}_{\mathrm{ex}}$ is excess free energy defined for non-ideal thermodynamics correction.

Adler et al. have studied oxygen exchange on MIEC cathodes, and discussed non-configurational contributions to the Gibbs free energy when mass-action no longer applies at large displacements from equilibrium [69]. Excess free energy due to non-ideal interactions of defects is thus incorporated into the mass-action kinetics rate expression (Eq.4.2) in a modification form

$$q = k_{\mathrm{f}}\prod_{k=1}^{K}[X_k]^{\nu_{\mathrm{f}}}\exp\left(-\frac{-(1-\beta_{\mathrm{ex}})}{\bar{R}T}\bar{G}_{\mathrm{ex}}\right) - k_{\mathrm{b}}\prod_{k=1}^{K}[X_k]^{\nu_{\mathrm{b}}}\exp\left(\frac{\beta_{\mathrm{ex}}}{\bar{R}T}\bar{G}_{\mathrm{ex}}\right)$$

(Eq. 4.24)

Such a modification captures the shifts in transition state and product energies due to non-ideal interactions.

For studying the Ni/GDC electrode kinetics, contributions of other components should be well isolated. While H_2 oxidation/H_2O electrolysis occurs on Ni/GDC WE, reverse reaction takes place on the Pt/YSZ CE. Kinetics of Pt/YSZ

electrode on H_2/H_2O reactions is derived from others' researches, as specified in Table 4.1 [65, 140]. YSZ surface chemistry proposed by Goodwin [66], is also shown in this table.

Table 4.1. Pt and YSZ surface kinetic and thermodynamic parameters [66, 140].

Reaction	A or γ_0	E_a (kJ/mol)	ΔG^0 (kJ/mol)
$H_{2(g)} + 2(Pt) \leftrightarrow 2H(Pt)$	0.129	0.0	5.45
$H_2O_{(g)} + (Pt) \leftrightarrow H_2O(Pt)$	0.108	0.0	1.37
$OH(Pt) + (Pt) \leftrightarrow H(Pt) + O(Pt)$	7.8×10^{20}	-79.5	56.5
$H_2O(Pt) + (Pt) \leftrightarrow H(Pt) + OH(Pt)$	3.8×10^{21}	74.5	-18.2
$H_2O(Pt) + O(Pt) \leftrightarrow 2OH(Pt)$	1.7×10^{19}	36.8	60.5
$H_2O_{(g)} + (YSZ) + O^{2-}(YSZ) \leftrightarrow 2OH^{-}(YSZ)$	1.2×10^{-4}	86.8	38.9
$O^{2-}(YSZ) + (YSZ\_b) \leftrightarrow O^{2-}(YSZ\_b) + (YSZ)$	7.3×10^{12}	80.1	8.6

The charge-transfer reactions pathway at Pt/YSZ interface in current modeling is set similar to the elementary charge-transfer reaction steps at Ni/YSZ interface proposed by Goodwin et al. [66]. The associated kinetic parameters are fitted to the kinetic experimental study of Pt/YSZ electrode at 800 °C from Mizusaki's work [65]. Initial fitting parameters are listed in Table 4.2 and Results comparing model predictions in current study with Mizusaki's experimental work are shown in Figure 4.2.

Table 4.2. Initial kinetic parameter for Pt/YSZ charge-transfer reactions (at 800 °C)

Reaction	A (mol, cm,s)	α
$H(Pt) + O^{2-}(YSZ) \leftrightarrow OH^{-}(YSZ) + (Pt) + e^{-}$	5×10^{12}	0.5
$H(Pt) + OH^{-}(YSZ) \leftrightarrow H_2O(Pt) + (YSZ) + e^{-}$	3×10^{13}	0.2
$H(Pt) + OH^{-}(YSZ) \leftrightarrow H_2O(Pt) + (YSZ) + e^{-}$	1×10^{11}	0.8

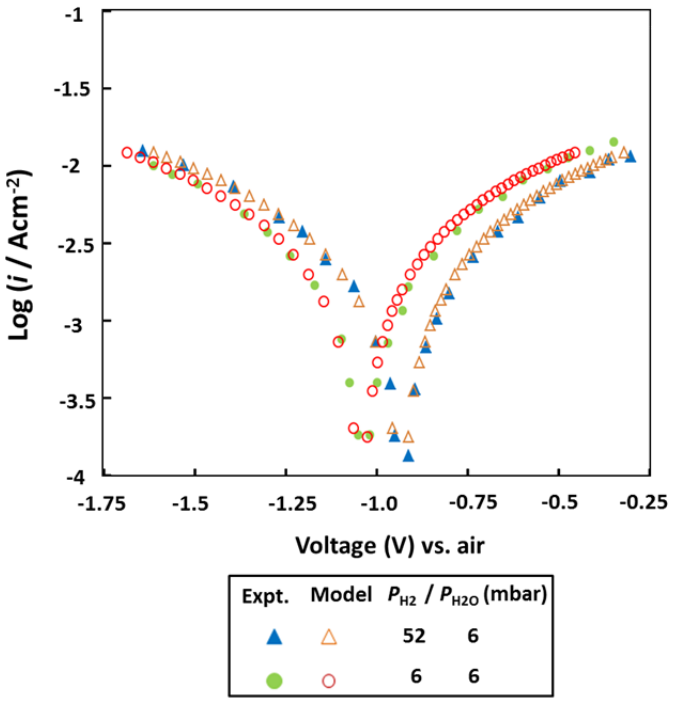

Figure 4.2. Comparison between kinetic model result and experimental study of thin-film Pt electrode on YSZ substrate for H_2/H_2O reaction, at P_{H2} = 52 mbar / P_{H2O} = 6 mbar and P_{H2} = P_{H2O} = 6 mbar, T = 800 °C, demonstrates the modeling is able to capture Pt CE electrode behavior in current thin-film GDC electrochemical cell modeling.

Figure 4.2 compares thermochemistry model results on Pt/YSZ electrode with the experimental study. The figure shows anodic (right part of the curve) and catholic (left part of the curve) currents as a function of potential bias. Anodic currents resulting in H_2 oxidation has a dependency on hydrogen partial pressure (P_{H2}), while effects of P_{H2} on H_2O electrolysis from cathodic current are negligibly small, as stated in Mizusaki et al. [65]. Overpotentials for H_2 oxidation on Pt/YSZ electrodes are smaller than those for H_2O electrolysis. Consistency of model prediction with experiment measurements demonstrates that the Pt/YSZ thermochemistry is valid for isolating Pt/YSZ CE contribution in the thin-film GDC electrochemical cell, thus to study the kinetics associated with the GDC WEs.

For temperature-dependent kinetic parameters such as forward rate coefficients, activation energy E_a = 1.39 eV for Pt/YSZ is used in this study [141], to calculate rate coefficient changes relative to 800 °C in Table 4.2.

As discussed in Chapter 3, charge-transfer reactions at GDC electrodes between 570 and 620 °C are largely limited to the Ni/GDC interface due to low mobility of the polaron (σ_e < 0.03 S/cm) of the GDC surface at these temperatures. Thus, the role of Ni surface in promoting H_2 dissociative adsorption and spillover to the GDC surface is important. For the purpose of studying interaction between Ni and GDC surfaces, reaction pathways and related kinetic parameters on Ni surface are extracted from Goodwin's study [66] as listed in Table 4.3.

Table 4.3. Heterogeneous reaction mechanisms on a nickel surface (700°C)

Reaction	A or γ_0	E_a (kJ/mol)	ΔG^0 (kJ/mol)
$H_{2(g)} + 2(Ni) \leftrightarrow 2H(Ni)$	0.01	0.0	-1.62
$H_2O_{(g)} + (Ni) \leftrightarrow H_2O(Ni)$	0.1	0.0	41.47
$H(Ni) + O(Ni) \leftrightarrow OH(Ni) + (Ni)$	5×10^{22}	97.9	34.83
$H(Ni) + OH(Ni) \leftrightarrow H_2O(Ni) + (Ni)$	3×10^{20}	42.7	-32.83
$2OH(Ni) \leftrightarrow H_2O(Ni) + O(Ni)$	3×10^{21}	100	-67.66

4.3 Results and Discussions

Exchange current density of Ni/GDC electrode on H_2/H_2O reactions is initially studied by fitting the Butler-Volmer equation using overpotential / current relation from the XPS study results in Figure 3.9a and Figure 3.11a at 570 °C and 620 °C respectively. The exchange current density parameters A_i, $E_{a,i}$, and α in Eqs.4.5 and 4.6 are used to fit the experimental results using nonlinear least squares method. The fitted exchange currents are plotted in Figure 4.3, which shows Arrhenius behavior with an activation energy $E_{a,f}$ = 3.2 eV. The fitting curve is consistent with exchange current density of GDC10 and GDC20 at 600 °C documented in Duncan's work [134], but the activation energy is much higher than the 1.1 eV shown Duncan's continuum-level electrochemical model result [135]. A possible explanation on the higher activation energy value is that increased mobility of polaron on the GDC surface at higher temperature extending the reaction from Ni/GDC interface to part of GDC surface.

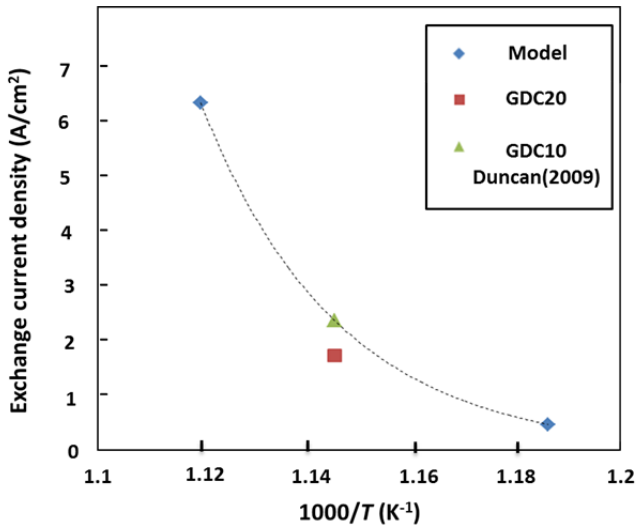

Figure 4.3. Exchange current density of Ni/GDC electrode plotted *vs.* 1000/*T*, in the XPS studies at 570 and 620 °C, in comparison with Duncan's study at 600 °C.

Based on the discussion of reactions on GDC surface and Ni/GDC surface in the previous chapter, fundamental reaction steps associated with H_2/H_2O reaction are set up as listed in Table 4.4.

Table 4.4. Initial GDC reaction mechanism and baseline kinetic parameters (570°C)

Reaction	A or γ_0 (mol, cm,s)	α	ΔG^0 (kJ/mol)
$H_2O_{(g)} + (GDC) \leftrightarrow H_2O(GDC)$	0.01	0.0	-19.2
$(GDC) + O^{2-}(GDC\_sb) \leftrightarrow O^{2-}(GDC) + (GDC\_sb)$	1×10^{13}	0.0	-9.2
$H_{2(g)} + O^{2-}(GDC) \leftrightarrow H_2O(GDC) + 2e^-$	1×10^{9}	0.4	-18.48
$H(Ni) + O^{2-}(GDC) \leftrightarrow OH^-(GDC) + (Ni) + e^-$	2×10^{9}	0.3	-9.66
$H(Ni) + OH^-(GDC) \leftrightarrow H_2O(GDC) + (Ni) + e^-$	4×10^{9}	0.3	3.5

The reactions involve both H_2 electro-oxidation on GDC surface and charge-transfer reactions at Ni/GDC interface. This allows the reaction to occur over a finite region of the GDC electrode surface beyond the TPB. Initial kinetic parameters are acquired by fitting the overpotentials / currents relation at 570 °C, provided in Table 4.4. It should be noted that the activation energy (E_a) is set to 0, thus the forward reaction rate coefficients (k_f) values are equal to A in the table. At 620 °C, the best fitting for A is 12.5 time of values at 570 °C, which is consistent with the ratio calculated based on activation energy (E_a = 3.2 eV) of the Ni/GDC charge-transfer reactions obtained from the fitting in Figure 4.3.

Preliminary simulation results are presented below with the proposed GDC mechanism and kinetic parameters. The simulation results are compared with experimental data presented in the previous chapters. Figure 4.4 shows overpotentials of Ni/GDC interface as function of currents at $P_{H2} = P_{H2O} = 0.2$ Torr, $T = 570$ and 620°C and $P_{H2} = 0.2$ Torr/$P_{H2O} = 0.04$ Torr, $T = 620$°C.

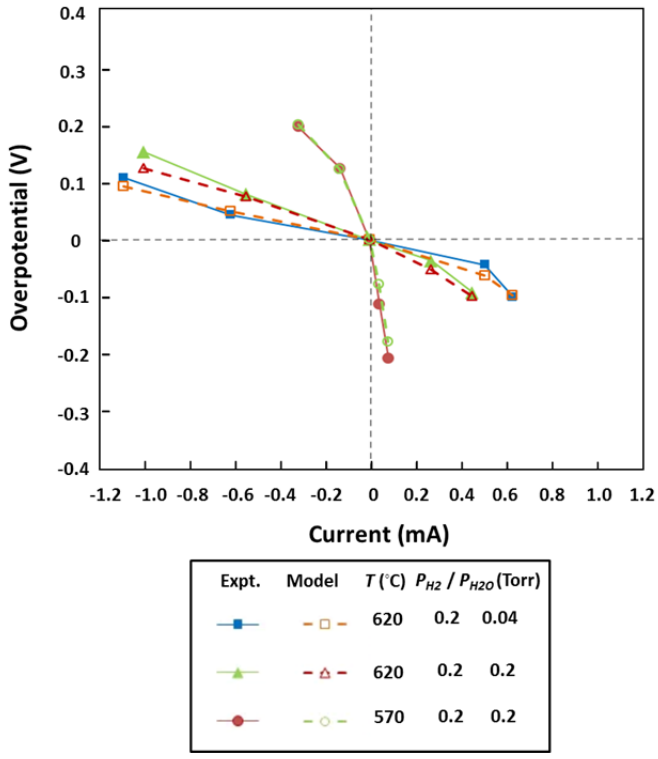

Figure 4.4. Comparison of model results on Ni/GDC interface overpotentials as function of currents with XPS mapped surface electric potentials at different temperatures and P_{O2}.

Consistent with the experiment observations, the model results further confirm better performance of GDC electrode on H_2O electrolysis. At baseline condition (P_{H2} = P_{H2O} = 0.2 Torr, T = 620 °C), the model results show 0.079 V overpotential at electrolysis current -0.55 mA, while overpotential on H_2 oxidation current at 0.46 mA is 0.098 V. At high P_{H2}/P_{H2O} ratio, both H_2 oxidation and H_2O electrolysis reactions are enhanced at the Ni/GDC surface that overpotential is approximately half of those at baseline condition at the same current. At the lower T = 570 °C, overpotentials of the Ni/GDC electrode for both reactions are significantly increased.

The enhanced performance at more reducing environments (lower effective P_{O2}) and higher T is partly due to further reduction of Ce^{4+} on the GDC surface. Experimental studies have shown increase in Ce^{3+} polaron concentration change as function of current and/or oxygen partial pressures on undoped ceria electrode [60, 61]. In addition, the concentration of Ce^{3+} increases with higher positive voltages and may explain the lower overpotentials on the GDC electrode for H_2O electrolysis than H_2 oxidation at the same current magnitudes.

The model with elementary reaction steps is able to capture all species involved in the reactions. Figure 4.5 depicts the surface vacancy model fraction as a function of current density for varying temperature and $P_{O2.}$ The GDC surface is dominated by vacancies at much higher concentrations than observed in bulk thin-film GDC at similar temperature and P_{O2} [55]. Study on thin-film $Sm_{0.2}Ce_{0.8}O_{1.9}$ (SDC) under similar environment has revealed that the surface partial molar enthalpy and entropy are elevated from bulk values by 96.5 kJ/mol and 115.8 J/mol-K, respectively [62]. XPS study on undoped ceria with similar electrode design has also suggested that the free energy of reduction at the ceria near-surface region is 2.09-2.20 eV lower than in the bulk. Also, observed surface Ce^{3+} are more than two orders of magnitude larger than the bulk equilibrium values [60].

GDC surface vacancy concentrations change with reaction direction (oxidation or electrolysis) or cell bias (V_{cell}) as demonstrated in Figure 4.5. The vacancy concentrations increase as H_2O electrolysis current increases, and decrease

as H_2 oxidation current increases. In general, the vacancy concentrations change more significantly with current at higher T and/or lower P_{O2}. This may be due to the increased electrochemical activity of the GDC surface with the higher electron mobility at these conditions.

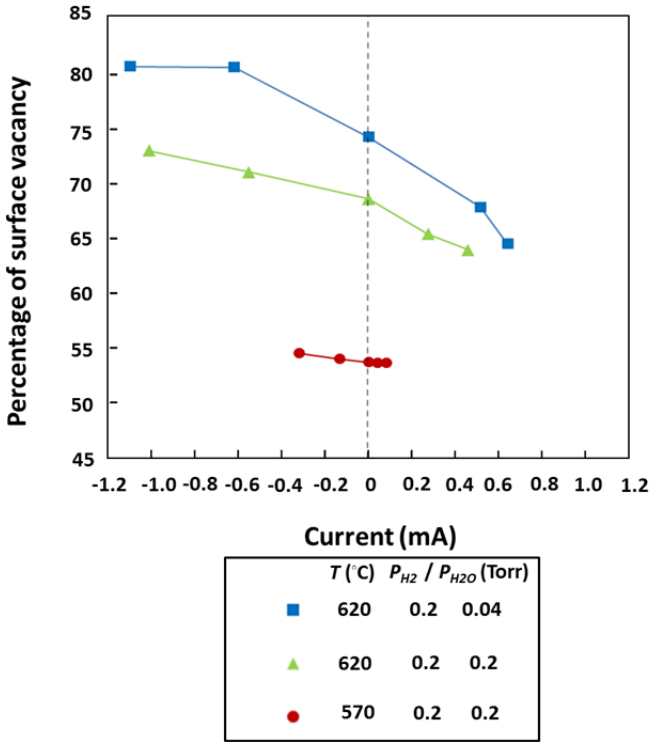

Figure 4.5. Model predictions on GDC surface vacancy percentage as a function of temperature and P_{O2}. The figure also show surface vacancy percentage change as a function of current at each working environment.

The model predictions on vacancy concentrations are not yet calibrated against experimental data on ceria spectra due to limited access to XPS facilities at

ALS. Further study and comparison the change of vacancy concentration could improve the model's accuracy.

Intermediate surface species (OH^-) associated with the H_2/H_2O reaction is further compared between model prediction and information extracted from XPS measurement as shown in Figure 4.6. During the H_2 oxidation reaction ($V_{cell} < 0$), the OH^- concentration on is smaller than at equilibrium ($V_{cell} = 0$). Measurable decrease/increase in OH^- concentration for H_2 oxidation/H_2O electrolysis suggests that OH^- participates in the rate-determining step for both directions. As illustrated in

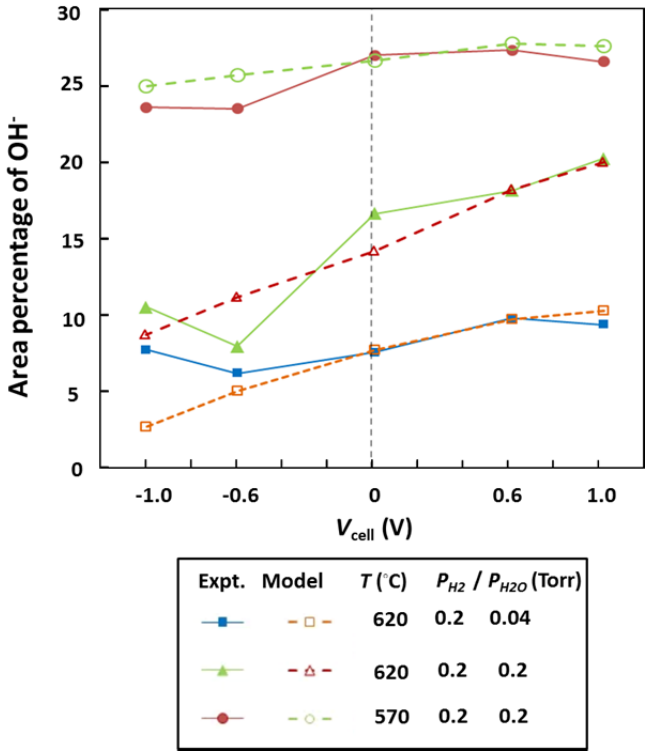

Figure 4.6. Comparison of model predictions on surface OH^- concentration of Ni/GDC interface plotted in area percentage of the total O1s spectra with XPS results as function of V_{cell} at different operation conditions.

Table 4.4, the two-step charge-transfer reactions at the Ni/GDC interface create and destroy surface OH^-. Specifically, the production rate of the OH^- (GDC) is slower in the first step of the reaction, but consumed rapidly in the second step.

The relation between OH^- concentrations and the reaction rates is further studied. OH^- area percentages from model prediction are plotted versus current in Figure 4.7. Slopes of OH- concentration change on H_2 oxidation are sharper than changes on H_2O electrolysis. The most significant drop at the same current magnitude is observed on $P_{H2} = P_{H2O} = 0.2$ Torr at $T = 570$ °C. Lower vacancy concentrations and mobility at GDC surface limit charge transfer at the Ni/GDC interface.

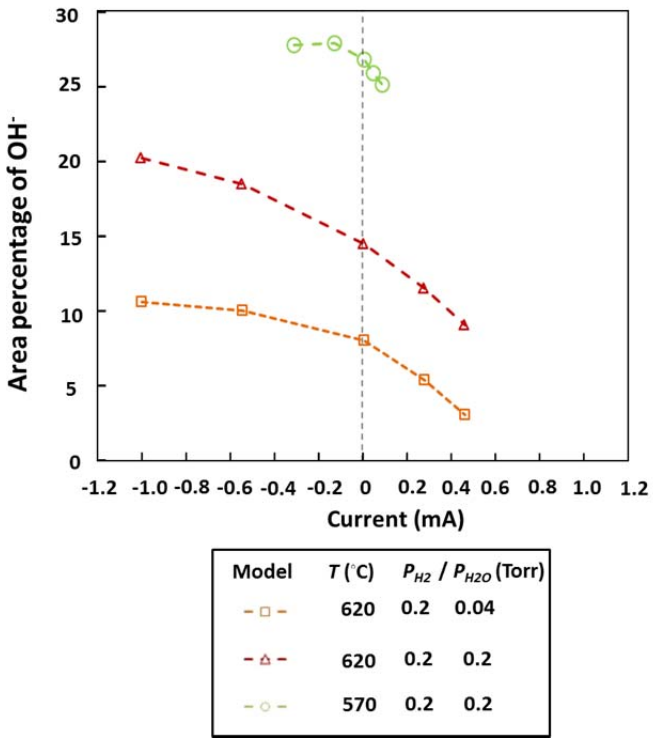

Figure 4.7. Comparison of surface OH^- concentration as a function of reaction rate from model results at tested P_{H2}/P_{H2O} ratio and temperatures.

Overpotenitals across the GDC/YSZ interface result from the oxide ion exchange at the two phases interface, and these overpotentials must be captured in a model. The oxide ion exchange is modeled simply as a single-step O^{2-} charge transfer at the two-phase interface with reaction parameters shown in the Table 4.5. Initial forward reaction rate coefficient (A) is given in Table 4.5 for fitting the GDC/YSZ overpotential at 570 °C. For higher temperatures, ratios of forward reaction rate coefficient are used with E_a = 1.53 eV fitted from GDC/YSZ overpotential results in Figure 3.11b.

Table 4.5. Initial GDC reaction mechanism and baseline kinetic parameters (570°C)

Reaction	A (mol, cm,s)	α	ΔG^0 (kJ/mol)
$O^{2-}(YSZ) + (GDC) \leftrightarrow (YSZ) + O^{2-}(GDC)$	2×10^{-5}	0.6	-97.4

The model results on GDC/YSZ interface overpotential are similar to the analysis from the XPS O1s spectra as compared in Figure 4.8. Setting the charge-transfer coefficient α = 0.6 can get the best fit to experimental data. This confirms that incorporating oxide ion from YSZ to GDC is relatively easier than in the opposite direction. It is clearly shown on the figure that slightly larger GDC/YSZ overpotential associated with H_2O electrolysis at the same current magnitude, despite better overall electrolysis performance. Furthermore, slope of the overpotential curve of P_{H2O} = 0.04 Torr is lower than that of P_{H2O} = 0.2 Torr at 620 °C. Even though effect of P_{O2} on

YSZ chemistry is minimal, further reduction of GDC bulk according to the lower P_{O2} results in lower overpotentials on both directions.

Information derived above provides a means to model the entire electrochemical cell performance. One of uncertainties of the GDC/YSZ overpotential fitting is that significant voltage jump from the GDC surface to the YSZ surface as shown in Figure 3.7. It is unclear how much the voltage change between two phases contributes to the charge-transfer reaction associated with the GDC/YSZ interface.

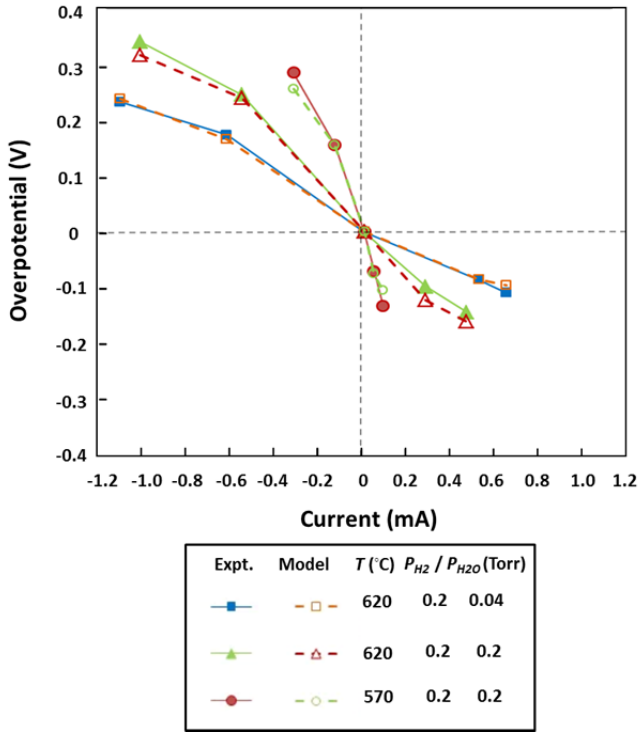

Figure 4.8. Comparison of model results on Ni/GDC interface overpotentials as function of currents with XPS mapped surface electric potentials at different temperatures and P_{O2}.

Simulation results of thin-film GDC electrochemical cell performance are further compared to electrochemical characterization results in the experimental studies, as shown in Figure 4.9. The model result is able to capture effect of temperature on the overall electrochemical performance.

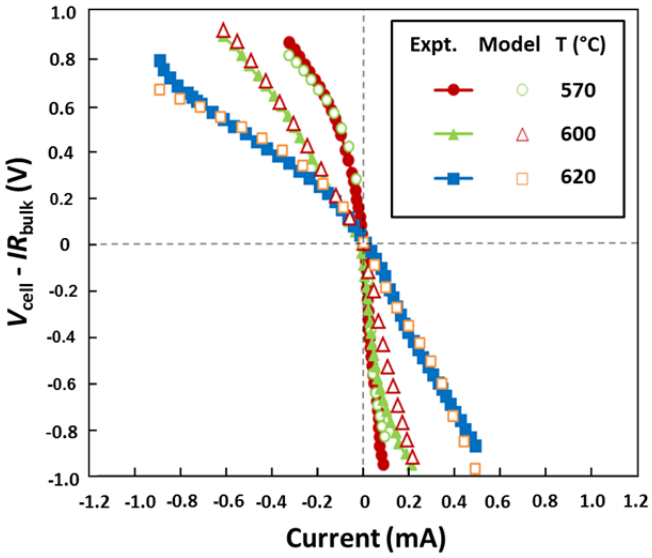

Figure 4.9. Comparison of full thin-film SOFC model results with experimental IR_{bulk}-corrected *V-I* curves at $P_{H2} = P_{H2O} = 0.2$ Torr, at 570, 600 and 620 °C.

In addition to Ni/GDC kinetic model on H_2/H_2O electrochemistry, effect of presence of carbonaceous species on the H_2 oxidation rate is further studied below. The CO oxidation/CO_2 electrolysis reaction rates are much slower than H_2 oxidation/H_2O electrolysis as observed and discussed in the experimental sections, that H_2 oxidation/ H_2O electrolysis dominates the charge-transfer reactions.

Presence of CO/CO_2 lowers H_2 oxidation or H_2O electrolysis reactions rate because carbon-based species cover the active surface site for the reactions. In the XPS measurement, it is observed that CO_3^{2-} is much depleted on the GDC surface while significant amount exists at the Ni/GDC interface. Thus, it can be deduced that stronger interaction of Ni with CO and CO_2 mainly contributes to the decrease rate. In order to account for the competitive surface adsorption on the Ni surface, heterogeneous reaction mechanisms of CO and CO_2 on Ni surface are further incorporated in addition to the H_2/H_2O kinetic model, as described in Table 4.6.

Table 4.6. Heterogeneous reaction of CO and CO_2 on Ni surface 600 °C [9].

Reaction	A or γ_0	E_a (kJ/mol)	ΔG^0 (kJ/mol)
$CO_{(g)} + (Ni) \leftrightarrow CO(Ni)$	0.5	0.0	-50
$CO_{2(g)} + (Ni) \leftrightarrow CO_2(Ni)$	1×10^{-5}	0.0	52.9
$CO_2(Ni) + (Ni) \leftrightarrow CO(Ni) + O(Ni)$	3.2×10^{23}	86.5	-61.1

Similar to Ni surface heterogeneous chemistry, CO/CO_2 reactions on Pt surface involve elementary reaction steps. A comprehensive surface reaction mechanism on Pt has been studied by Mhadeshwar and Vlachos describing H_2 oxidation, CO oxidation, and water-gas shifts reaction on the Pt catalyst [140]. The current study assumes H_2/H_2O reactions dominate the Pt/YSZ charge-transfer reaction and presence of CO/CO_2 mixture only competitively adsorbs on the Pt surface, which lower the charge-transfer reaction rates at Pt/YSZ listed in Table 4.2. Surface heterogeneous reactions are incorporated, as described in Table 4.7.

Table 4.7. Heterogeneous reaction of CO and CO_2 on Pt surface at 600 °C [140].

Reaction	A or γ_0	E_a (kJ/mol)	ΔG^0 (kJ/mol)
$CO_{(g)} + (Pt) \leftrightarrow CO(Pt)$	1	0.0	-42.6
$CO_{2(g)} + (Pt) \leftrightarrow CO_2(Pt)$	0.195	0.25	69.8
$CO_2(Pt) + (Pt) \leftrightarrow CO(Pt) + O(Pt)$	1.68×10^{19}	110.5	34.2

Figure 4.10 shows the model predicted results on CO/H_2O reaction at 600 °C considering surface coverage effect on the charge-transfer reactions. Discrepancies between model predictions and experimental results are observed at large overpotentials. Discrepancies may be due to the model not capturing the WGS reaction. Other explanations may include contributions of the Pt/YSZ interface, but limited data does not provide adequate measures for these phenomena.

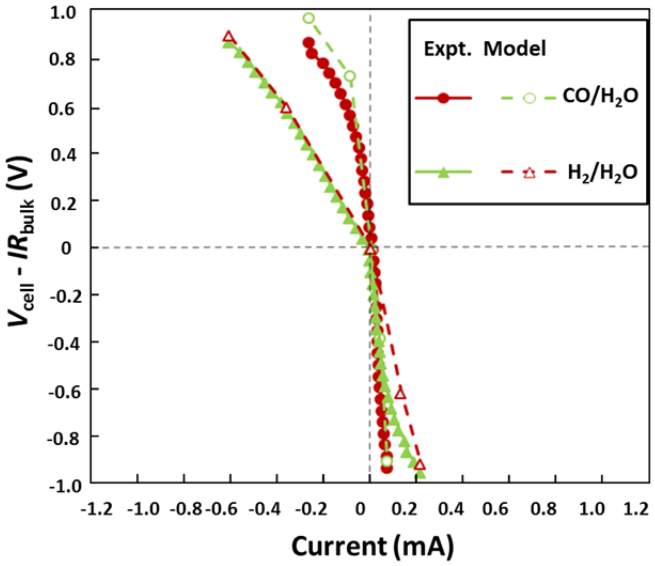

Figure 4.10. Comparison of initial model results with experimental IR_{bulk}-corrected *V-I* curves at $P_{H2} = P_{H2O} = 2$ Torr and $P_{CO} = P_{H2O} = 2$ Torr, $T = 600$ °C.

4.4 Conclusions

In this chapter, elementary charge-transfer reaction pathways of H_2/H_2O reaction on the Ni/GDC electrode are established in order to understand the fundamental behavior of the GDC anodes in the IT-SOFC environments. A 1-D kinetic model based on elementary reactions is developed with incorporated thermodynamics properties and initial kinetic parameters. Results on both GDC surface species concentration and interfacial overpotentials are compared with experimental measurements. Consistency of model prediction with experimental result demonstrates that the kinetic model with proposed reaction pathways and fitted kinetic parameters is able to describe H_2 oxidation and H_2O electrolysis on GDC electrode between 570 °C and 620 °C.

Effect of surface coverage carbon-based species on the H_2 oxidation/H_2O electrolysis is also studied. The model incorporated with the surface coverage of small carbon species predicts similar performance as in the experiment. Conclusions drew from this initial study is limited due to the small data sample, but a preliminary model for CO electrochemical oxidation developed in this chapter provides a framework for further exploring GDC electrode kinetics on CO oxidation. However, the slow CO electrochemical oxidation rates, which are around an order of magnitude slower than H_2 electrochemical oxidation on GDC at temperatures of interest, may not be critical for multi-dimensional SOFC modeling where significant H_2 is available either through direct H_2 feeds or internal reforming of hydrocarbon feeds.

Chapter 5: Three-dimensional Modeling of SOFCs with Ni/GDC Anodes

The previous chapters investigated the fundamental kinetics of H_2 oxidation on an idealized thin-film GDC electrode at typical IT-SOFC operation temperatures. The results suggest that the role of hydrogen spillover from the active Ni catalyst to GDC promotes charge-transfer reactions under low-temperature conditions when electron mobility of the GDC surface is low. In practical Ni/GDC SOFCs, the anode functional layers (AFLs) employ porous Ni/GDC composite structures that provide sufficient gas/Ni/GDC TPB to enhance fuel oxidation. The path through the porous anode support structures to active Ni/GDC AFLs supplies the fuel reactants and allows the removal of the oxidized products. The thicker porous support layer masks the electrochemically active functional layer from visual or spectroscopic measurements. Nonetheless, information on both the anode support and functional layers can be used to build multi-scale SOFC models that incorporate the physical transport in the gas and solid electrolyte phases and the chemical processes on various electrode surfaces.

This chapter focuses on the development of and results from a three-dimensional, non-isothermal SOFC model using computational fluid dynamics based in the COMSOL Multiphysics platform. The model utilizes simplified anode fuel oxidation kinetics based on Butler-Volmer expressions derived from the studies

presented in the previous chapters for the Ni/GDC composite electrodes. The performance of IT-SOFC with Ni/GDC-based anodes operating on H_2 and CH_4 reformate fuels is evaluated. Effects of operating conditions, electrolyte thickness, and CH_4 internal reforming on the cell performance are explored by studying a unit cell incorporating a single anode and cathode channels around an MEA with a porous Ni/GDC anode, a dense GDC electrolyte, and a porous LSCF/GDC cathode. Simulation results are used to evaluate stack performance by providing detailed local information such current density, temperature, and gas composition. Modeling studies on the GDC-based stack provide essential information for designing IT-SOFCs stacks [142].

5.1 Stack Model Development

3-D stack model for a planar anode-support SOFC is developed and implemented in COMSOL Multiphysics (version 4.3a). The model simultaneously solves mass, species, momentum, electric charge, and energy balances in the porous anode and cathode, the dense electrolyte, and the gas-flow channels.

To make the 3-D GDC-based SOFC simulation computationally efficient, a unit cell for the model domain, as illustrated in Figure 5.1, is defined which consists of single channel flows in each electrode with symmetry planes on the side surface. For the current study, the anode and cathode flows are arranged in co-flow. Some common assumptions are made for the model as listed here

- external heat loss limited to the inlet and outlet planes;

- ideal gas behavior;
- uniform porous structures for the anode functional layer, the anode support layer and the cathode;
- electrochemical reactions confined to anode functional layer and cathode;
- electrochemical reactions modeled with single Butler-Volmer expression.

5.1.1 Model Geometry

The modeling for the GDC-based IT-SOFC stack used 10-20 μm thick GDC10 ($Ce_{0.9}Gd_{0.1}O_{1.95}$) electrolytes which are effective for operation up to 650 °C. The model cell has Ni/GDC-based anode, and an LSCF/GDC composite cathode, schematically shown in Figure 5.1. A porous metal mesh layer is added between each electrode and interconnects in order to model stack in the experimental study using metal mesh for better current collection. In this study, the co-flow channel length is fixed at 100 mm equivalent to an actual stack size (10 cm × 10 cm). The channel length/width and length/height ratios are a typical size for an SOFC stack. Table 5.1 provides information on key geometric parameters for both cathode and anode that are used in this study. Microstructure parameters are chosen from multi-dimensional SOFC modeling studies [143-145].

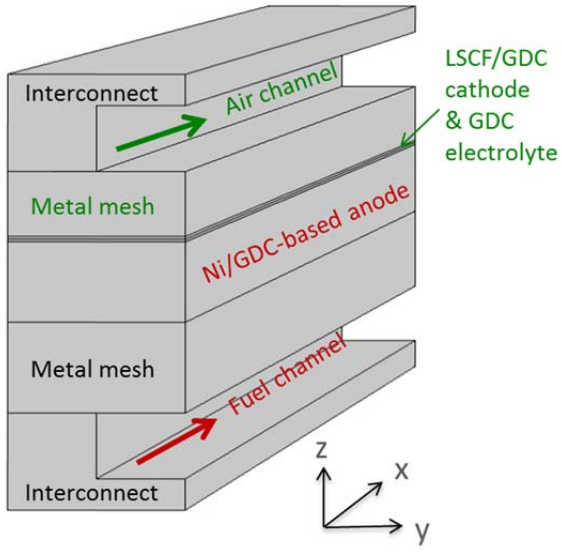

Figure 5.1. Schematic of the single channel model used in current modeling study.

Table 5.1. Geometric properties of the model cell electrodes.

Geometric Parameters	Anode	Cathode
Total porous electrode thickness	600 μm	20 μm
Functional layer thickness	15 μm	N/A
Porosity	0.35	0.35
Pore tortuosity	3.5	3.5
Average pore radius	0.5 μm	0.5 μm
Specific catalyst area	1×10^{5} m^{-1}	1×10^{5} m^{-1}
Interconnect rib height	0.75 mm	0.75 mm
Interconnect rib width	1.2 mm	1.2 mm
Channel width	1.2 mm	1.2 mm
Channel height	0.6 mm	0.6 mm
Metal mesh thickness	0.7 mm	0.5 mm

5.1.2 Model Equations and Key Parameters

In COMSOL modeling, the governing partial differential equations for species, momentum, charge and energy balances are applied to each subdomain. Each set of equations are solved numerically by applying appropriate boundary conditions.

Gas transport and mass conservation

The Maxwell-Stefan equation is used to describe mass diffusion and convection of the gases inside the fuel cell as follows [78, 146].

$$\nabla\left(-\rho \cdot Y_k \sum D_{kj} \cdot \left(\nabla X_j + \left(X_j - Y_j\right)\frac{\nabla \mathrm{p}}{p} \cdot \boldsymbol{u}\right)\right) + \rho \cdot (\boldsymbol{u} \cdot \nabla) Y_k = \dot{s}_k \qquad \text{(Eq. 5.1)}$$

where Y and X are gaseous species mass fraction and molar fraction respectively. D_{kj} is binary diffusion coefficient [147, 148]. $\dot{s}_k$ is the source term. For H_2 fuel, the source term is coupled with charge-transfer reaction in the AFL and the cathode, respectively. When CH_4 reformate is fed to anode, the source term also attributed to internal reforming and water-gas shift reactions.

In porous SOFC electrodes, the transport of gaseous reactants is also governed by porous microstructure properties. The effective binary diffusion coefficients in the porous media $\left(D_{kj}^{e}\right)$ are related to ordinary binary coefficient in the bulk as [149]

$$D_{kj}^{e} = \frac{\phi_g}{\tau_g} D_{kj} \qquad \text{(Eq. 5.2)}$$

Momentum equations

Momentum balance is considered in the flow channels and electrodes to account for depletion and generation of gaseous species during the reaction. The momentum equation is solved at these domains as follows [77, 78]

$$\rho \boldsymbol{u} \cdot \nabla \boldsymbol{u} = \nabla \cdot \left(-p\mathbf{I} + \mu(\nabla \boldsymbol{u} + (\nabla \boldsymbol{u})^T) - \frac{2\mu}{3}(\nabla \boldsymbol{u})\mathbf{I} \right) + \rho \boldsymbol{g} \qquad \text{(Eq. 5.3)}$$

In the electrode, the momentum equation is modified in the form of the Brinkman equation, in order to account for transport phenomena in the porous media.

$$\frac{\mu}{K}\boldsymbol{u} = \nabla \cdot \left(-p\mathbf{I} + \mu(\nabla \boldsymbol{u} + (\nabla \boldsymbol{u})^T) - \frac{2\mu}{3}(\nabla \boldsymbol{u})\mathbf{I} \right) + \rho \boldsymbol{g} + \boldsymbol{F} \qquad \text{(Eq. 5.4)}$$

where K is permeability of the electrode. $\boldsymbol{F}$ is the volume force vector applied to the fluid due to the generation and depletion of the species during reactions.

Heat transfer and energy balance

During SOFC operation, some of the chemical energy is released as thermal energy during the electrochemical reactions in the electrode functional layers. Also non-electrochemical reactions such as internal reforming of methane in the anode support layer result in non-isothermal cell conditions, and thus thermal energy balances are necessary to solve the distribution of temperature T through the cell. Solving for T throughout the cell allows for the model to assess the effect of heat transferred through the cell boundaries to the environment. The general heat conduction equation is established to calculate the temperature distribution as follows

$$\rho c_{p,\text{eff}} \boldsymbol{u} \cdot \nabla T = \nabla \cdot (k_{\text{eff}} \nabla T) + Q \qquad \text{(Eq. 5.5)}$$

where $c_{p,\mathrm{eff}}$ and k_{eff} are effective specific heat and thermal conductivity respectively of heat transfer media. Q is heat source within the cell.

Heat generated during the fuel cell operation due to Ohmic, reversible and irreversible losses is referred as a source term in the heat equation. Regarding the negligible radiation heat exchange at IT-SOFC temperatures [150], the heat source is given to the anode functional layer, electrolyte, and cathode as

$$Q = \left(\frac{\overline{H}_{\mathrm{f,H2O}}}{2F} - V_{\mathrm{cell}}\right) i_{\mathrm{ext}} \qquad \text{(Eq. 5.6)}$$

where $\overline{H}_{\mathrm{f,H2O}}$ is the formation enthalpy of global H_2 oxidation reaction. When CH_4 reformate is fed to anode, the heat source term also involves endothermic internal reforming and exothermic water-gas shift reactions.

In the porous electrode, effective thermal properties are evaluated as

$$k_{\mathrm{eff}} = \phi_g \cdot k_{\mathrm{g}} + \left(1 - \phi_g\right) \cdot k_{\mathrm{s}} \qquad \text{(Eq. 5.7)}$$

$$c_{p,\mathrm{eff}} = \phi_g \cdot c_{p,\mathrm{g}} + \left(1 - \phi_g\right) \cdot c_{p,\mathrm{s}} \qquad \text{(Eq. 5.8)}$$

where g and s represent gas and solid phase respectively. Thermal parameters such as c_p and k are adapted from modeling studies on tubular SOFC and single-chamber SOFC [77, 147].

Electrochemical reactions

During SOFC operation, H_2 oxidation (R.1.3) and O_2 reduction (R1.5) occur at the anode functional layer and cathode respectively. Concentration independent exchange current density expressions are derived from fitting button cell data [51]. The exchange current density expression are shown in Eq.5.9 and Eq.5.10 for anode and cathode respectively,

$$i_{0,a} = k_{0,a} * \exp\left(-\frac{E_{a,a}}{\bar{R}T}\right) \quad \text{(Eq. 5.9)}$$

$$i_{0,c} = k_{0,c} * \exp\left(-\frac{E_{a,c}}{\bar{R}T}\right) \quad \text{(Eq. 5.10)}$$

The kinetics parameter for Eq. 5.9 and 5.10 are listed in Table.5.2. Exchange current densities from above expression and kinetic parameters are consistent with those in Duncan's work ($i_{0,a}$ = 2.4 A/cm^2 and $i_{0,c}$ = 1.05 A/cm^2 at T = 600 °C) [134].

Table 5.2. Kinetics parameter of exchange current density expression

Kinetic Parameters	Anode	Cathode
Exchange current density coefficient (A_0)	3.76×10^9 A/m^2	3.52×10^{13} A/m^2
Exchange current density activation energy (E_0) [135, 151, 152]	0.9 eV	1.65 eV

In the stack model, H_2 and O_2 concentrations decrease along the channel due to the electrochemical reaction at each electrode. Both catalyst surface heterogeneous chemistry and charge-transfer reactions depend on reactant concentration in the mass-

action kinetic [9]. Exchange current densities on anode and cathode are rate-limited by the surface species at each electrode. Therefore, the exchange current densities are modified as concentration-dependent expression as follows for the anode [78, 150]

$$i_a = i_{0,a}\left(\frac{P_{\mathrm{H2}}}{P_{\mathrm{H2,ref}}}\right)^{1.25}\left(\frac{P_{\mathrm{H2O}}}{P_{\mathrm{H2O,ref}}}\right)^{0.25}\left[\exp\left(\frac{1.5F\eta}{\bar{R}T}\right)-\exp\left(-\frac{0.5F\eta}{\bar{R}T}\right)\right] \quad \text{(Eq. 5.11)}$$

and cathode

$$i_c = i_{0,c}\left(\frac{P_{\mathrm{O2}}}{P_{\mathrm{O2,ref}}}\right)^{0.25}\left[exp\left(\frac{0.5F\eta}{\bar{R}T}\right)-exp\left(-\frac{0.5F\eta}{\bar{R}T}\right)\right] \quad \text{(Eq. 5.12)}$$

Steam reforming and WGS reactions

When SOFCs are fed with small hydrocarbons – most notably CH_4 as part of a reformate feed, internal reforming of the CH_4 (R.5.1) inside SOFC porous anodes enables the conversion of CH_4 into H_2 and CO. The CO can further react with H_2O to form CO_2 and H_2 in the water-gas shift (WGS) reaction (R.5.2)

$$\mathrm{CH_4 + H_2O = 3H_2 + CO} \quad \text{(R.5.1)}$$

$$\mathrm{CO + H_2O = H_2 + CO_2} \quad \text{(R.5.2)}$$

Ni catalytic activity for the reforming reaction is well known, but the role of GDC on the steam-reforming and WGS reactions remain an active area of research. Study of the CO/CO_2 reaction on thin-film Ni/GDC electrodes in Chapter 3 suggests that CO electrochemical oxidation is significantly slower than H_2 oxidation. With the fast rates of WGS expected on Ni-containing catalysts, it is expected that CO will be

converted via WGS, and thus H_2 oxidation will be the dominant electrochemical reaction in the Ni/GDC electrode.

In this initial modeling, the anode internal reforming rate and forward reaction rate constant for R.5.1 are given in Eq. 5.13 and Eq.5.14. The reverse reaction rate constant can be determined from the equilibrium constant, which is defined as function of temperature [153]. The reforming rate can be expressed as

$$r_{\mathrm{SR}} = k_{f,\mathrm{SR}} * \left(P_{\mathrm{CH4}} P_{\mathrm{H2O}} - \frac{P_{CO} P_{\mathrm{H2}}^3}{K_{\mathrm{eq,SR}}} \right) \qquad \text{(Eq. 5.13)}$$

where forward reaction rate coefficient $(k_{f,\mathrm{SR}})$ is

$$k_{f,\mathrm{SR}} = 2359 * \exp\left(\frac{-231266}{\bar{R}T}\right) \qquad \text{(Eq. 5.14)}$$

and equilibrium constant is

$$K_{\mathrm{eq,SR}} = 1.027 \times 10^{10} \exp(-0.251Z^4 + 0.367Z^3 + 0.581Z^2 - 27.134Z + 3.277) \qquad \text{(Eq. 5.15)}$$

where

$$Z = \frac{1000}{T\,(K)} - 1 \qquad \text{(Eq. 5.16)}$$

And the WGS reaction (R.5.2) is also modeled with a forward rate and a reverse process based on the equilibrium constant

$$r_{\mathrm{WGS}} = k_{f,\mathrm{WGS}} * \left(P_{\mathrm{CO}} P_{\mathrm{H2O}} - \frac{P_{\mathrm{H2}} P_{\mathrm{CO2}}}{K_{\mathrm{eq,WGS}}} \right) \qquad \text{(Eq. 5.17)}$$

where forward reaction rate coefficient $(k_{f,\mathrm{WGS}})$ is

$$k_{f,WGS} = 0.0171 * \exp\left(\frac{-103191}{\bar{R}T}\right) \quad \text{(Eq. 5.18)}$$

and equilibrium constant is

$$K_{\text{eq,WGS}} = \exp(-0.294 * Z^3 + 0.635 * Z^2 + 4.179 * Z + 0.317) \quad \text{(Eq. 5.19)}$$

The experimental study of CO/H_2O reaction in Chapter 2 suggests that electrochemical oxidation of H_2 slows with the presence of carbon-based species. Relatively slow CO oxidation on Ni surface results in significant surface site fractions of carbon species (ex. CO(Ni), CO_2(Ni)) [103, 143]. The presence of carbon-based fuel, can lead to carbon deposition on the Ni catalyst surface although the presence of ceria-containing materials around the Ni has been shown to significantly mitigate this risk [154-156].

Although little is known about how surface carbon species affect H_2 oxidation rate, it is clear that charge-transfer reaction for H_2 oxidation on Ni strongly depends on surface coverage of hydrogen, H(Ni). The availability of active catalyst surface as shown in Janardhanan and Deutschmann‘s work suggests a multi-step heterogeneous reaction mechanism for Ni catalysts. Most of the expressions are expressed in Arrhenius rate form and are dependent on the surface coverage [143]. Therefore, in this study, anode exchange current density is modified as

$$i_{a,0} = \theta_H * A_a * \exp\left(-\frac{E_{a,a}}{\bar{R}T}\right) \quad \text{(Eq. 5.20)}$$

where θ_H is surface coverage of H on the Ni surface.

The surface coverage of H on the Ni surface can be calculated through elementary heterogeneous reaction mechanism as described Zhu et al [9]. In order to capture the surface coverage while maintaining computational efficiency, the model uses a simplified empirical expression by fitting the elementary heterogeneous chemistry predictions over the relevant range of experimental conditions given as follow

$$\theta_H = \frac{K_1^{1/2} x_{H2}^{1/2}}{\left(1 + K_1^{1/2} x_{H2}^{1/2} + K_2 x_{CO}\right)} \qquad \text{(Eq. 5.21)}$$

where K_1 and K_2 are fitting parameters. The expression values are consistent with full CH_4 chemistry results shown in Figure 5.2 with fitted parameters in Table 5.3.

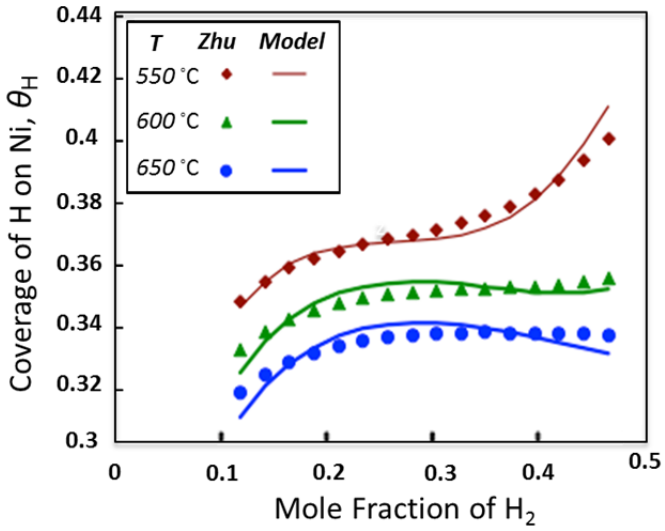

Figure 5.2. Comparison of simplified expression fitting to full CH_4 chemistry in Zhu et al. [9].

Table 5.3. Fitting parameters K_1 and K_2 in empirical expression for H surface coverage on the Ni surface.

Temperature (°C)	K_1	K_2
550	4.050	38.000
600	3.026	22.826
650	2.649	17.856

5.1.3 Leakage Current Modeling

Although as an electrolyte material, GDC has good ionic conductivity between 550 °C and 650 °C, GDC also shows significant electronic conductivity at these temperatures when exposed to SOFC anode environments with $P_{O2} < 10^{-20}$ bar. The electron flux through the GDC from the anode toward the cathode short circuits the oxidation reaction and drops the open-circuit voltage (OCV), thereby decreasing the cell efficiency [92, 157-159]. Modeling studies on the OCV drop with GDC electrolytes calculated the OCV drops with overpotentials from anode and cathode [134, 135]. Additionally, recent experimental studies have observed that H_2 oxidation occurs with this internal circuit even at OCV conditions (i_{ext} =0) [160].

The mixed ionic and electronic transport in bulk GDC impacts the voltage drop from theoretical OCV as well as electrochemical reactions. The model in this work captures the leakage current phenomena. Specifically, at OCV condition (i_{ext} =0), oxide ion fluxes from cathode to anode in the GDC phase while charge-transfer reactions take place at both anode and cathode and resulting electron (polaron) fluxes in the opposite direction as shown in Figure 5.3.

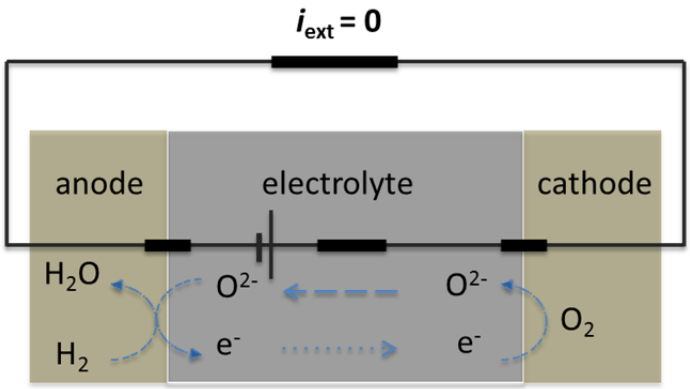

Figure 5.3. Schematic of the leakage current model: charge-transfer reactions take place at anode and cathode, oxide ion and electron flux internally at i_{ext} = 0.

Oxide ion and electron transports within GDC electrolyte phase are governed by Nernst-Plank equation, which is the species conservation in the solid phase,

$$\frac{\partial C_i}{\partial t} + \nabla \cdot (-D_i \nabla C_i - z_i F u_i C_i \nabla \phi) = S_i \qquad \text{(Eq. 5.22)}$$

where C_i is concentration of three charge carrier $V_{\ddot{O}}$ (+2), Ce'_{Ce} (-1) and Gd'_{Ce}(-1) in the GDC electrolyte. S_i is the source term due to charge-transfer reaction at anode/electrolyte (R.5.3) and cathode/electrolyte (R.5.4), respectively

$$H_{2(g)} + 2Ce^{X}_{Ce} + O^{X}_{O} \leftrightarrow H_2O_{(g)} + V_{\ddot{O}} + 2Ce'_{Ce} \qquad \text{(R. 5.3)}$$

$$2Ce^{X}_{Ce} + O^{X}_{O} \leftrightarrow \frac{1}{2}O_{2(g)} + V_{\ddot{O}} + 2Ce'_{Ce} \qquad \text{(R. 5.4)}$$

In Eq.5.22, D_i is diffusion coefficient (m^2/s) and u_i is mobility (m^2/V-s). D_i and $u_{m,i}$ are related as follows:

$$u_i = \frac{D_i}{\bar{R}T} \qquad \text{(Eq. 5.23)}$$

Mobilities of ion and electron within GDC bulk phase are given by [53]

$$u_{m,\mathrm{V_{\ddot{O}}}} = T^{-1} * 10^{\left(-1.5338-\frac{3405}{T}\right)} \quad \text{(Eq. 5.24)}$$

$$u_{m,\mathrm{Ce'_{Ce}}} = T^{-1} * 10^{\left(-0.2211-\frac{4320}{T}\right)} \quad \text{(Eq. 5.25)}$$

Charge neutrality of the electrolyte phase is maintained at each electrolyte location by

$$\sum_{i=1}^{3} z_i C_i = 0 \quad \text{(Eq. 5.26)}$$

Oxygen vacancies $\mathrm{V_{\ddot{O}}}$ are created in conjunction with the ceria redox reaction in reducing environments, as indicated in R.5.3. Boundary condition of non-stoichiometry of GDC is given by Eq.5.27 fitting to the bulk oxygen non-stoichiometry data in Bishop's work [55].

$$\Delta G^0_{\mathrm{reac}} + \bar{R}T\ln\left(\delta^{\mathrm{a}} P^{\mathrm{b}}_{\mathrm{O2}}\right) = 0 \quad \text{(Eq. 5.27)}$$

where ΔG^0_{reac} is calculated based on the NASA polynomials calculated from enthalpy and entropy values. a and b are fitting parameters. The fitted expression is shown as follows

$$\log(\delta) = -0.28\log(P_{\mathrm{O2}}) - \frac{\Delta G^0_{\mathrm{reac}}}{4.11\bar{R}T} \quad \text{(Eq. 5.28)}$$

Initial results are compared with Bishop's non-stoichiometry study, shown in Figure 5.4. The fitted expression is able to capture the oxygen deficiency at the boundary of GDC electrolyte. The slight difference from the experimental results may due to defect interaction when degree of Ce^{4+} increases.

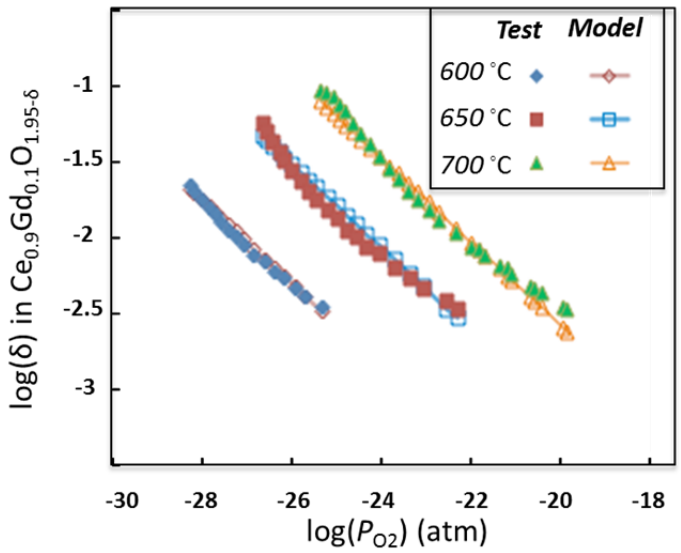

Figure 5.4. Comparison GDC non-stoichiometry from fitted expression for boundary condition with experimetnal result from Bishop's wok.

Modeling studies are performed for H_2 fuel (97% H_2 and 3% H_2O) and CH_4 reformate (46.1% H_2, 35.2% H_2O, 4.4% CO, 8.3% CO_2, and 6% CH_4) at IT-SOFC operation temperature range (550 - 650 °C). The simulations study steady-state *V-i* relation, i.e. for a given external current (i_{ext}) through the boundary, a cell potential (V_{cell}) is calculated.

Model simulations are performed in COMSOL MULTIPHYSICS using stationary solver to solve state space variables. The state variables include Y_k (gas mass fractions), $\boldsymbol{u}$ (velocity field), P (gas pressure), T (temperature), ϕ_m(electrical potential in phase m), and C_i (concentration of charge species in the GDC).

Computational meshes are built up from 5 discretizations for each layer in the vertical y-direction, 10 discretizations across the width of domain in z-direction, and 50 in the axial x-direction (coordination shown in Figure 5.1), all of which results in 267518 state variables to solve. The computations are performed on a Windows Sever (24 GB RAM, 2.67 GHz, 64 bit, 8 processors). Total computation time for is approximately 1 h for each operating point (i.e. i_{ext}).

5.2 Model Results on H_2 Fuels and Discussions

5.2.1 Initial Results and Discussions

Initial simulations with 97% H_2 / 3%H_2O under excess flow and isothermal conditions simulated button cell electrochemical performance at 550, 600, and 650 °C [51]. Model results on measured voltages at a selected external current density, shown in Figure 5.5, are consistent with the button cell tests at these conditions. The *V-i* curves for these conditions can largely be modeled as a straight line, but with OCV varying significantly at test conditions. Figure 5.5 demonstrates that the charge-transfer reaction rate expression and proposed kinetic parameters is adequate to characterize GDC-based IT-SOFC performance.

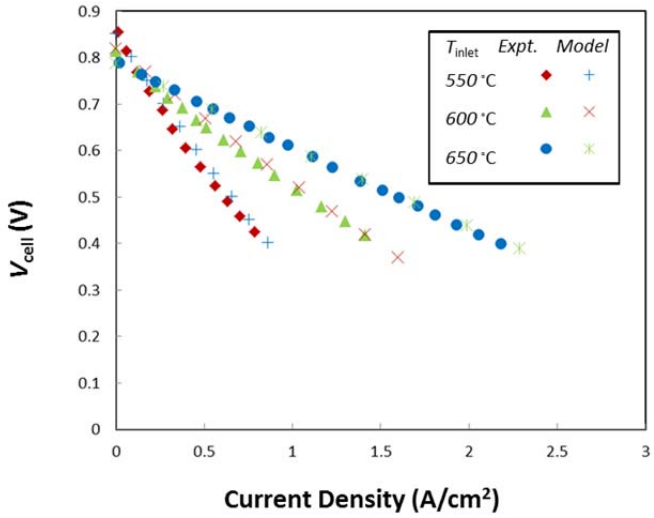

Figure 5.5. Comparison of electrochemical performance of the stack model with experimental *V-i* curves, at button cell conditions using excess H_2 and air flows.

The model further performs isothermal condition studies on OCV at 550, 600, and 650 °C to verify that the leakage current model is able to capture the electronic flux and OCV drops. The model inlet temperature, fuel composition and fuel utilization are listed in Table 5.4.

Table 5.4. Baseline inlet condition of model simulation on H_2 fuel

Temperature	550 - 650 °C
Composition	97% H_2 and 3% H_2O
Stoichiometry	Anode: 70% fuel utilization, Cathode: $\lambda_{air} = 4$ at 1.0 A/cm^2

3-D modeling results with H_2 fuel are compared with detailed analysis of the GDC electrolyte OCVs as shown in Figure 5.6. The results suggest OCVs are

significantly lower than those of conventional YSZ-based high temperature SOFCs (>1.0 V), because the undesired leakage current in the GDC. The OCV of GDC cells exponentially decreases as the electrolyte gets thinner. Thinner electrolyte results in larger electrochemical potential gradient, driving oxide ion from cathode to anode, and electrons in the opposite direction. Increasing internal charge fluxes further increases overpotentials thus OCV drops.

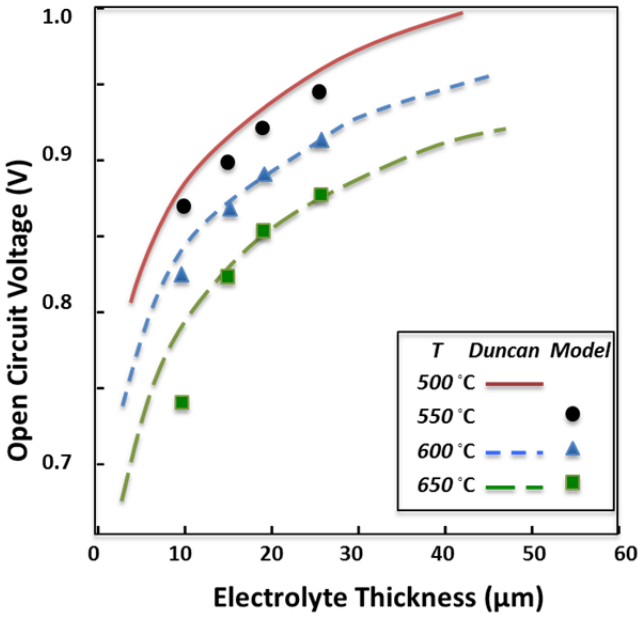

Figure 5.6. The leakage model is able to capture the open circuit voltage dope compared to Duncan's work [135].

For constant electrolyte thickness, higher temperature lowers OCV. This is because mobility of charges in the GDC bulk is largely enhanced by higher temperature, resulting in larger charge fluxes and higher degree of reactions at OCV. Another reason is that non-stoichiometry of GDC exposed to the anode increases, which further increases the electron flux.

Ionic current density (A/m^2) vertically through the electrolyte is plotted in Figure 5.7. The study models GDC cell with 20 μm-thickness electrolyte at 600 °C at OCV condition. An average of 0.3 A/cm^2 current density is shown on the electrolyte even with zero external load. OCV is thus lowered due to this Ohmic loss on ionic current as well as overpotential on the interface.

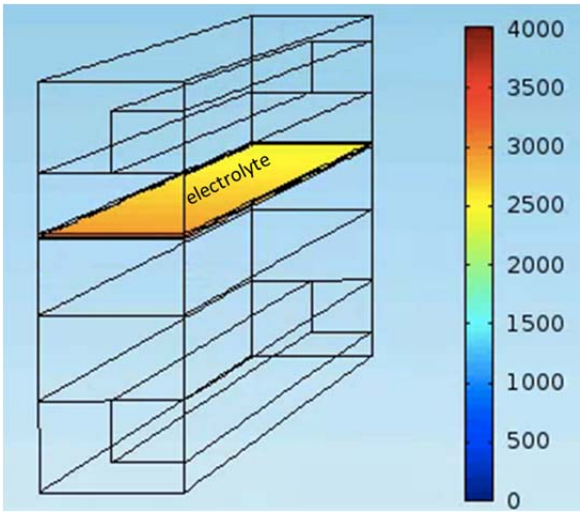

Figure 5.7. Ionic current density (A/m^2) across the electrolyte membrane, at OCV, T = 600 °C in the isothermal condition on H_2 fuel.

In addition to a lower OCV resulting in lower stack efficiency, the SOFC efficiency is deteriorated further by fuel consumption due to the leakage current. Figure 5.8 shows H_2 molar fraction distribution along the cell and transverse the anode. Consumption of H_2 is observed at the anode/electrolyte interface in the model prediction. Although there is no direct observation of H_2 oxidization, measurable amount of water generation still evidences that the H_2 consumption after nickel oxide is fully reduced.

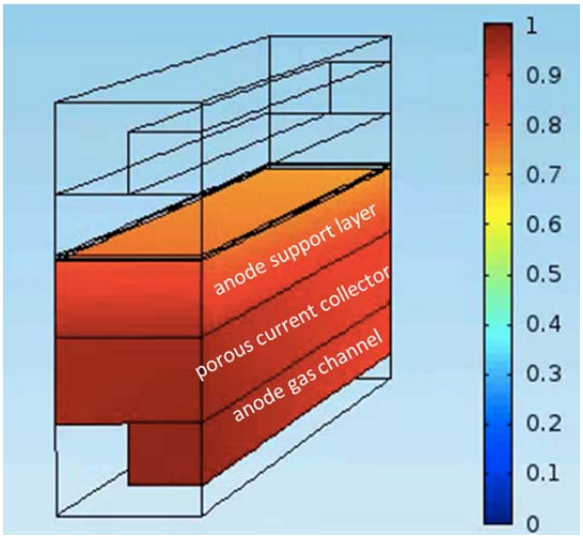

Figure 5.8. 3-D plot of H_2 molar fraction distribution in the stack anode, at OCV, T = 600 °C in the isothermal condition on H_2 fuel.

The study is furthered to non-isothermal conditions in order to explore how both exothermic and endothermic reactions impact the temperature distribution and thus the stack performance. In addition to the reactions, the non-isothermal model also explores the effect of external heat transfer with an external heat-transfer coefficient h_{surf} up to 100 W/cm^2/K at the channel ends. The non-isothermal model starts at inlet temperature T_{in} = 600 °C with H_2 fuel. Again H_2 molar fraction is plotted in Figure 5.9 at OCV condition. In comparison with the isothermal case (Figure 5.8), ~15% of H_2 is consumed close to the electrolyte interface, which is much larger than the isothermal condition. Increasing H_2 consumption suggests higher leakage current at non-isothermal condition, as shown in Figure 5.10.

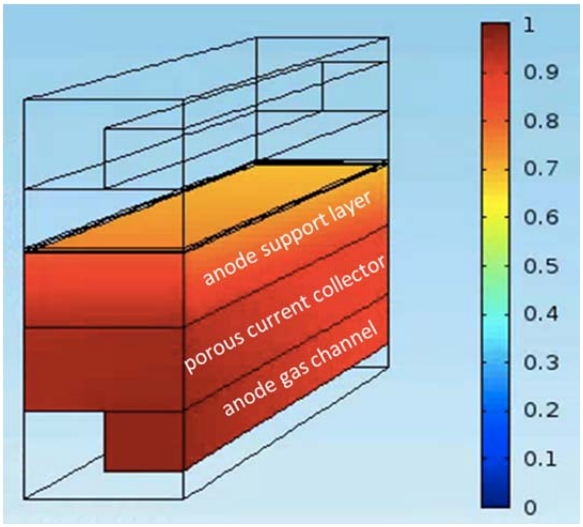

Figure 5.9. 3-D plot of H_2 molar fraction distribution in the stack anode at OCV, T_{in} = 600 °C in the non-isothermal condition.

Figure 5.10 shows the polarization curve of the modeled stack in non-isothermal conditions with cathode and anode inlet flows at 600 °C. Average electronic leakage current density (i_e) at OCV condition (i_{ext} = 0 A/cm^2) is close to 0.6 A/cm^2, twice the value at isothermal condition due to rise in temperature across the cell from heat release, which gives higher electronic conductivity of the GDC. The heat release is due to exothermic H_2 oxidation with the OCV oxide ion flux to the anode. Figure 5.10 shows that increasing i_{ext} leads to lower leakage current densities i_e. When i_{ext} is 1.0 A/cm^2, i_e drops to 0 A/cm^2. The decrease of leakage current is due to the vacancy decrease in the GDC electrolyte with the more rapid oxide ion flux across the cell as i_{ext} increases. This increases the effective P_{O2} in the GDC electrolyte resulting in lower electronic mobility.

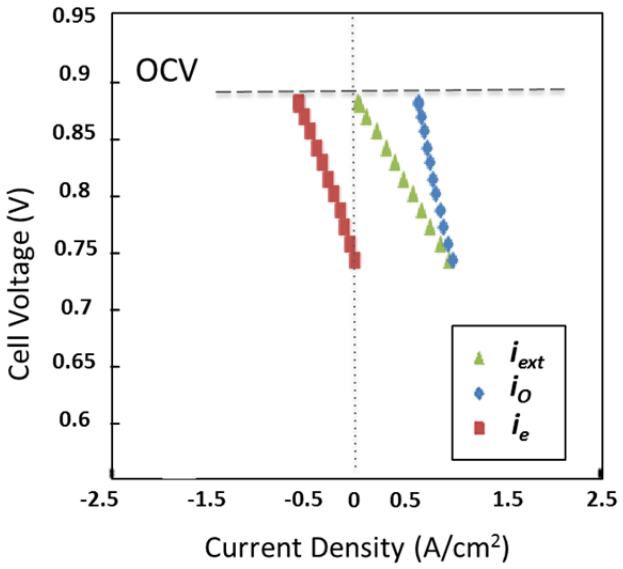

Figure 5.10. External current density, ionic current density and electronic current density plotted in *V-i* curves for GDC stack with 20-µm-thickness electrolyte at T_{in} = 600 °C.

H_2 and temperature distributions at 1 A/cm^2 are plotted in Figure 5.11a and Figure 5.11b, respectively. At anode/electrode interface, H_2 is almost depleted. Large H_2 concentration gradient is shown transverse the anode. This may be due to low porosity and high tortuosity values used in this study as suggested DeCaluwe and coworker in their modeling work [73].

Temperatures rise ~65 °C down the channel is shown in Figure 5.11b. Even though increasing temperature promote gas transport and electrochemical reaction rate, thus the cell performance, large temperature gradients can increase thermo-mechanical stresses on the cell layers and lead to delamination of interfaces or

cracking. CTE mismatches between the cathode and the electrolyte can leads to cathode degradation [161].

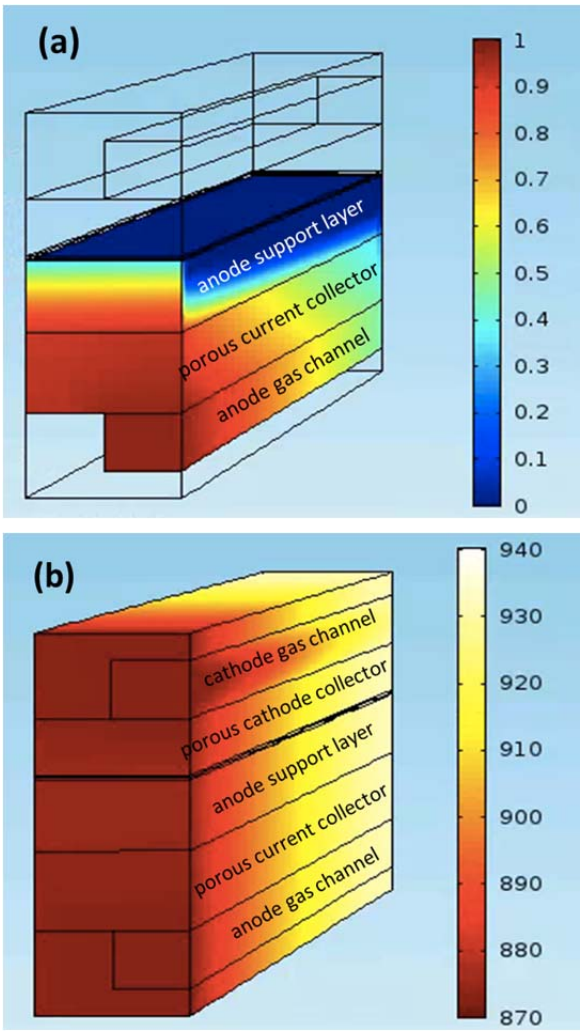

Figure 5.11. 3-D plots of (a) H_2 molar fraction distribution in anode and (b) temperature distribution (in K) in the stack, at i_{ext} = 1 A/cm^2, T_{in} = 600 °C in the non-isothermal model.

5.2.2 Inlet Temperature and Electrolyte Thickness on OCV and Performance

For SOFCs with GDC electrolytes, the OCV depends strongly on both the

operation temperature and the electrolyte thickness. Thus, the model is used to study the effects of inlet temperature T_{in} on electrochemical performance, as shown in the model *V-i* curves plotted in Figure 5.12. This figure shows the OCV drops to 0.86 V when T_{in} rises to 650 °C. However, area specific resistance (ASR) is only 0.116 $\Omega \cdot cm^2$ at 650 °C, which is 1/3 of the ASR = 0.35 at 550 °C.

Also it is clear from the figure that the ASR at 650 °C is lower than 600 °C, and the current density outperforms that at lower temperatures. Therefore, despite the higher leakage current at higher temperature that lowers the OCV, reducing Ohmic resistance by increasing temperature may deliver better performance at the high current density range. There is a trade-off between reducing Ohmic resistance and decreasing in lower OCV.

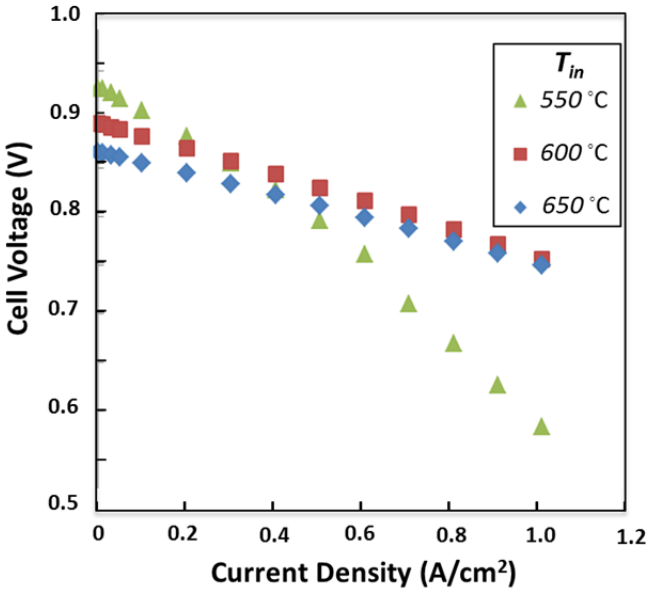

Figure 5.12. Model prediction on electrochemical performance as *V-i* curves of the SOFC stack with 20 μm-thickness electrolyte, at T_{in} = 550, 600 and 650 °C.

The trade-off between reducing Ohmic resistance and decreasing OCV with reducing electrolyte thickness is shown in Figure 5.13. Reducing electrolyte from 20 to 10 μm significantly lowers the OCV, but only slightly the ASR. The reason for the small ASR improvement is that leakage current density i_e increases significantly as shown in Figure 5.14. Even though the leakage current shrinks with increasing external current density, the leakage current is still approximately 0.5 A/cm^2 at i_{ext} = 1.0 A/cm^2.

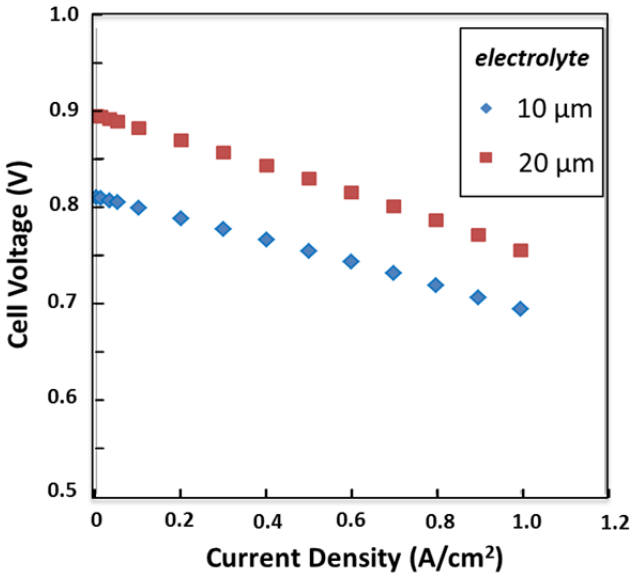

Figure 5.13. Model prediction on electrochemical performance of different electrolyte thickness as plotted in *V-i* curves, at T_{in} = 600 °C.

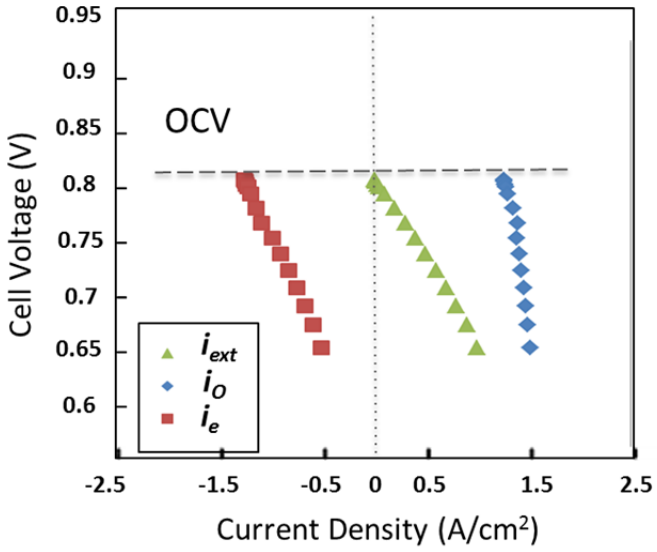

Figure 5.14. External current density, ionic current density and electronic current density plotted in *V-i* curves for GDC stack with 10-μm-thickness electrolyte at T_{in} = 600 °C.

5.3 Model Result on Methane-derived Fuels with Internal Reforming

The stack model is also used to evaluate CH_4 reformate (46.1% H_2, 35.2% H_2O, 4.4% CO, 8.3% CO_2, 6% CH_4) performance and compares it with 10 × 10 cm^2 GDC-based SOFC test results [160] as shown in Figure 5.15. Slightly lower OCVs are observed when compared to the H_2 simulation with 20-μm-thickness electrolyte in Figure 5.12. The drop in OCVs may be due to either thinner electrolyte of the cell or slight leakage in this test. In order to capture the OCVs in the reformate tests, thinner electrolyte (12 μm) is used in the model simulation. Despite thinner electrolyte, the ASR is greater than that of H_2 at the same temperature, possibly because the CO content in the anode functional layer, which lowers the activity of the anode catalyst as discussed in Chapter 4. Using surface coverage expression in Eq. 5.18 allows the

model to capture the effect of CO in the reformate stream on the electrochemical performance.

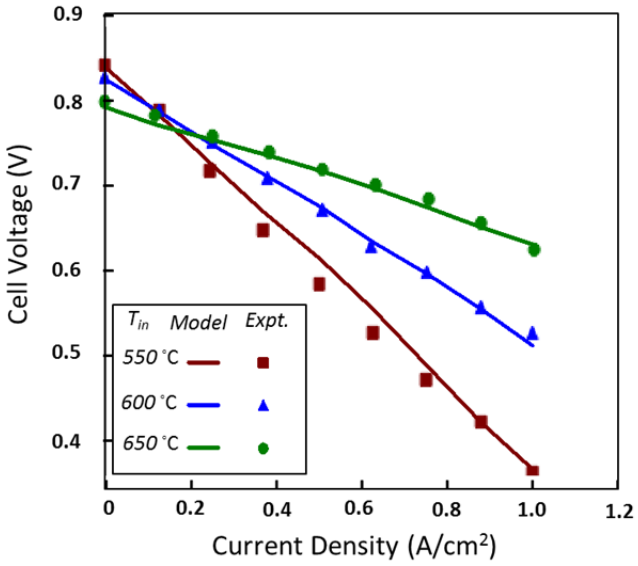

Figure 5.15. Comparison of model prediction on electrochemical performance with experimental result of the 10 x 10 cm^2 GDC-based cell using CH_4 reformate feed at 1 LPM fuel flow rate.

The model is also used to predict the species distribution in the anode, as shown in Figure 5.16a and 5.16b for H_2 and CH_4 respectively, at T_{in} = 600 °C, i_{ext} = 0.125 A/cm^2. The H_2 content decreases along the channel while the concentration gradient transverse the channel is relatively small. This is caused by constantly converting CH_4 and CO into H_2 by the internal reforming and WGS reactions in the anode support layer and function layer. Figure 5.16b shows that CH_4 is almost depleted close to the electrolyte.

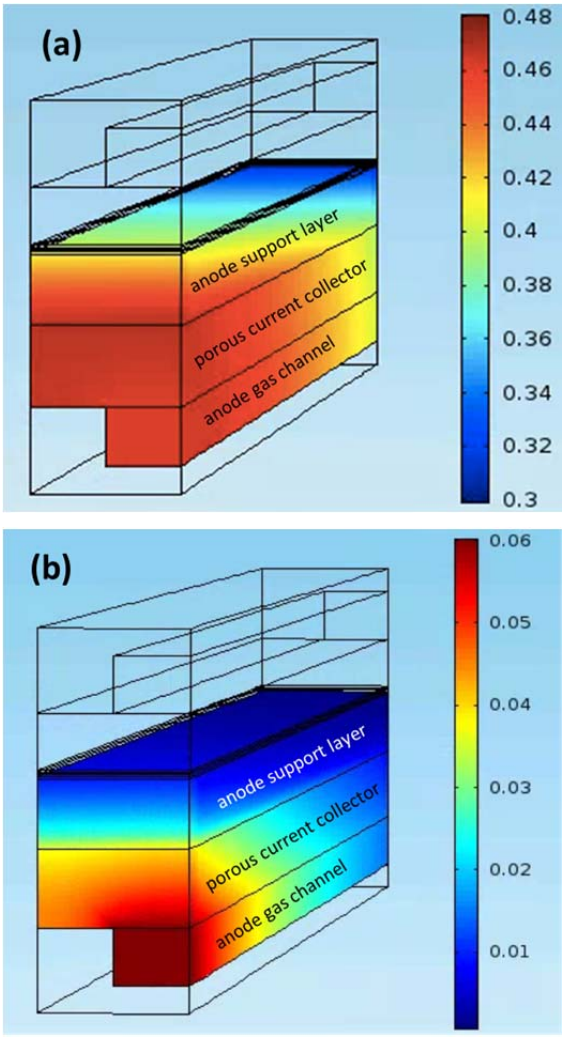

Figure 5.16. H_2 and CH_4 molar fraction distribution within the anode, at T_{in} = 600 °C and external current density i_{ext} = 0.125 A/cm^2.

With the leakage current increasing the fuel oxidation, fuel consumption is higher than the calculation from i_{ext}. Figure 5.17 shows model prediction on exhaust composition compared with experimental measurement at i_{ext} = 0.125 A/cm^2. Measured H_2 mole fraction in exhaust is lower than model prediction without considering fuel oxidation due to leakage current as suggested in (a) for H_2 and (c) for

CH_4. Such discrepancies are enlarged at higher temperature because leakage current increases at higher temperature which increases fuel consumption. Including the fuel oxidation due to leakage current in the model provides much improved prediction of exhaust H_2 and CH_4 mole fractions as shown in (b) and (d). This further confirms the conclusion that charge-transfer reactions take place at OCV condition and the overpotentials associated with the reactions contribute to the OCV drop in addition to Ohmic losses.

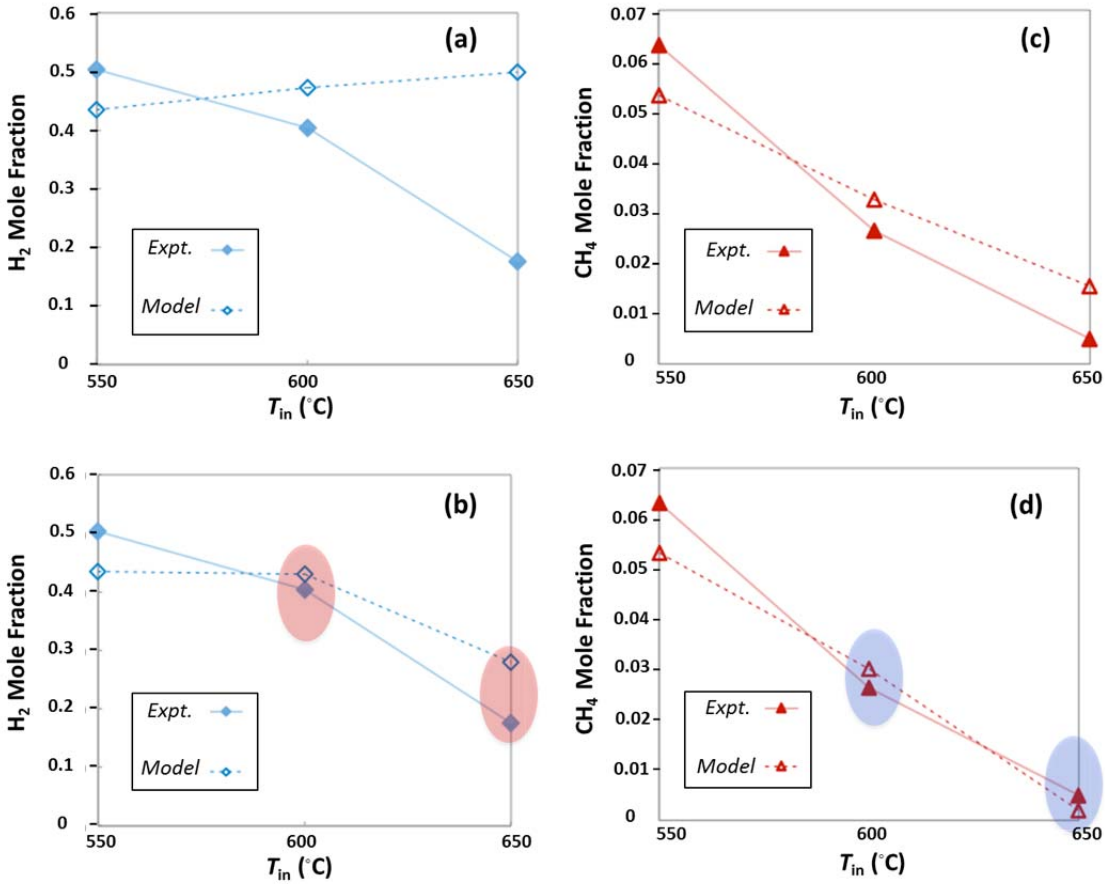

Figure 5.17. Comparison measured H_2 and CH_4 mole fractions in stack exhaust with model prediction. (a) and (c) without considering fuel oxidation due to leakage current. (b) and (d) considering fuel oxidation due to leakage current.

Temperature profiles for the entire cells operating with an anode inlet of reformate are shown for 600°C inlet flows. The results in Figure 5.18 show that temperature increase is small. Despite of lowering electrochemical performance using CH_4 reformate, internal reforming alleviates the large temperature gradient as observed in H_2 feed. The temperature slightly decreases and distributes evenly over the whole channel.

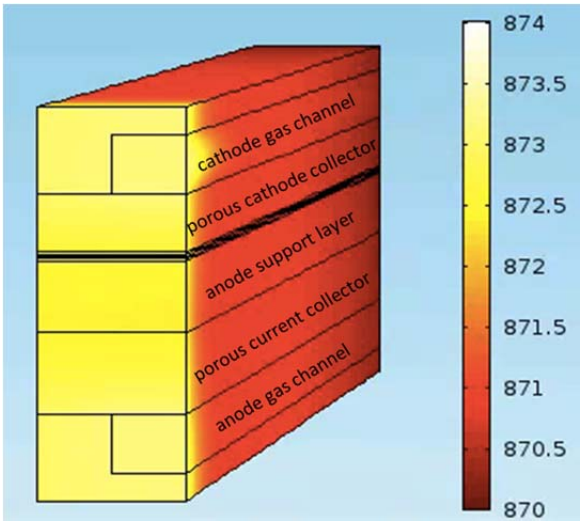

Figure 5.18. Temperature (in K) distribution along the channel at T_{in} = 600 °C, i_{ext} = 0.125 A/cm^2 for CH_4 reformate feed.

5.4 Conclusions

This chapter presents a 3-D IT-SOFC simulation with detailed physical and chemical processes for gas-transport, charge transport, interfacial reactions and other phenomena. The model also incorporates variation of leakage current in electrolyte to predict GDC-based stack performance with H_2 and reformate feeds. Initial results of the 3-D stack model show great consistency with experimental data and that the

leakage current modeling is able to capture the OCV drop from the theoretical value duel to the electronic flux across electrolyte membrane as well as fuel consumption due to the electronic current. The 3-D stack model can be used to investigate the species and temperature profile down the channel at different operation conditions from a cell and stack design point-of-view.

The model results indicate the importance of operating conditions on the stack performance. Exploring temperature distribution in non-isothermal stack models helps to identify thermal management strategies to maintain good GDC electrolyte performance and to lower risk to thermo-mechanical degradation. The study also explores using reformate with internal reforming for maintaining relatively uniform temperatures across the length of the cell in order to achieve reduced temperature gradients and increased durability of IT-SOFCs long-term operations. The modeling framework provides a strong tool for exploring the potential of intermediate-temperature SOFCs for operation on H_2 and partially reformed CH_4 through internal reforming. The model presented here establishes the basis for further detailed modeling studies on GDC-based SOFCs operating with a range of fuel composition and with various cell designs for stack performance assessment and eventually system design.

Chapter 6: Conclusions and Outlook

In this study, kinetics of H_2 oxidation and CO oxidation on Ni/GDC composites as IT-SOFC anodes are investigated and applied in 3-D SOFC stack level modeling. The study provides a framework for continued study and design of GDC-based anodes for IT-SOFC application. To this end, the study incorporates the following:

- fabrication of thin-film GDC electrochemical cells and study electrochemical performances on H_2/CO oxidation and H_2O/CO_2 electrolysis;
- *in operando* AP-XPS to investigate change of surface potential and surface species concentration related to operation environments and working conditions;
- development of a 1-D isothermal model to study kinetics of thin-film GDC electrode and comparison of model results with the experimental results to obtain thermodynamic and kinetic parameters for H_2 oxidation on the GDC electrode;
- implementation of a 3-D non-isothermal SOFC model to provide a framework for stack performance evaluation and design optimization.

From these efforts, the role of GDC on fuel oxidation in Ni/GDC composite SOFC anodes is elucidated. The GDC surface catalytic activity largely depends on the polaron mobility on the GDC surface. With high polaron mobility, the GDC anode can extend fuel electro-oxidation to the surface region away from the Ni/GDC

interface. While for low mobility, the electrochemistry relies on synergic role of Ni surface which is limited close to Ni/GDC interface.

6.1 Summary of Results

6.1.1 Experimental Studies of Thin-film GDC Electrochemical Cells

Chapter 2 describes the fabrication and electrochemical characterization of the thin-film GDC electrochemical cell at a range of P_{H2}/P_{H2O} and temperatures. The results from experimental studies suggest that catalytic performance of GDC surface is much enhanced at lower $P_{O2,}$ higher temperature, and cathodic current respectively due to increased surface vacancy concentrations. Comparison of polarization curves (IR_{bulk} corrected *V-I* curves) between Ni/GDC and Au/GDC electrodes reveals that role of Ni on H_2 spillover and charge-transfer reaction between Ni/GDC interface becomes more important when the GDC surface doesn't have sufficient ionic and electronic motilities at T = 600 °C.

Experimental study of the GDC electrode on CO/CO_2 electrochemistry shows that CO/CO_2 mixture delivers much lower performance, despite lower P_{O2} than H_2/H_2O mixtures with the same partial pressure ratio. This draws a conclusion that CO oxidation and CO_2 reduction on GDC are much slower. Additional tests on CO/H_2O mixture suggest water-gas shift reaction can quickly convert CO to H_2 and enhance cell performance. However, presence of CO and CO_2 still lowers rates of H_2 oxidation and H_2O electrolysis.

Further studies are taken using ambient pressure X-ray photoelectron spectroscopy (AP-XPS) for simultaneous surface analysis and electrochemical characterization. The AP-XPS is a valuable technique for analyzing the GDC electrode surface during the electrochemical cell operation. Analysis of measurement provides qualitative and quantitative information on H_2 oxidation and H_2O reduction mechanisms of the thin-film GDC electrode. By analyzing the O1s spectra scanning across the Ni/GDC interface, GDC surface, and GDC/YSZ interface, changes of local surface potential associated with the reaction rate are acquired. The measurement of surface potential and interface overpotential relates charge-transfer reactions rate in term of current. Such a relation provides fundamental kinetic information on the H_2/H_2O reaction mechanism development.

Plots of overpotential as measured by O1s peak shifts vs. current provide a basis for determining the nature of the H_2 oxidation or H_2O electrolysis. From these analyses, it is concluded that higher OH^- concentration together with higher current on Ni/GDC interface than on Au/GDC at the same potential bias. This confirms that H_2 dissociate adsorption on the Ni surface promotes the charge-transfer reaction.

AP-XPS also initially characterizes CO/CO_2 reactions on the Ni/GDC electrode. Analysis of the O1s spectra reveals much of CO_3^{2-} concentration locates at Ni/GDC interface while the amount at GDC surface is small. The CO_3^{2-} concentration at the interface suggests that charge-transfer reaction mainly occurs at Ni/GDC interface and CO_3^{2-} is an intermediate species associated with the reactions.

6.1.2 Modeling Efforts in Assessing GDC Electrode in IT-SOFC Application

Chapter 4 focuses on using simulation methods to develop a 1-D isothermal kinetic model for thin-film GDC electrode. Important kinetic parameters are estimated for H_2 oxidation and H_2O electrolysis on GDC electrode between 570 and 620 °C. The results qualitatively agree with the experimental polarization curve. Reaction pathways and associated parameters are identified on the Ni/GDC interface and GDC surface.

The kinetic model correctly predicts changes in electrochemical performance and surface OH^- concentrations with varying P_{O2} and temperatures, which are consistent with those observed in XPS measurements. Consistent results verify the effectiveness of current kinetic model in describing H_2/H_2O reaction on Ni/GDC composite electrode. Furthermore, the model also predicts higher vacancy concentration at lower P_{O2} or higher T and increasing vacancy concentration with a positive voltage bias when H_2O electrolysis occurs on the GDC electrode.

Even though a more in depth understanding kinetics of the GDC interacting with CO/CO_2 is not fully achieved in this study due to lack of quantitative XPS characterization, relation between surface coverage carbon-based species and exchange current density is proposed in this study. This relation is further formulized into an empirical expression that is used in 3-D stack modeling on CH_4 reformate.

Chapter 5 extends this electrode kinetic study into SOFC anode application. Due to higher doping concentration ($Ce_{0.8}Gd_{0.2}O_{1.9}$) in the kinetic study, the 3-D stack model employs more widely used GDC material ($Ce_{0.9}Gd_{0.1}O_{1.95}$) with related kinetic parameters to perform stack simulation. The stack model provides a framework that is readily to input any kinetic parameter depending on component materials.

The 3-D stack model with consideration of leakage current of the GDC electrolyte studies GDC-based stack performance with H_2 and CH_4 reformate feeds. Great consistency of model predictions with experimental data on OCV, *V-i* curves and exhaust compositions demonstrates effectiveness of the model. The model is able to investigate the species concentration and temperature profile down the channel at different operation conditions of the stack, rendering it a tool to evaluate the stack performance from a design's perspective.

6.2 Future Work

A better understanding of effect of vacancy concentration change on electrode performance would further extend the scope of this study. AP-XPS has been proven to be a valuable technique for analyzing spectra of core-level elements. Thus, further studies are needed to develop a more quantitative AP-XPS measurement of surface reduction state of the GDC electrode.

Furthermore, a good extension of current study involves the testing of a broader range of P_{CO}/P_{CO2} and temperatures. The challenge faced in this study is

limited access to AP-XPS facilities. Data derived from these tests could be valuable to further study CO/CO_2 and also expand the XPS studies to $H_2/H_2O/CO/CO_2$ mixtures to assess the impact of carbonaceous fuels on the behavior of GDC electrode in active electrochemical cells. Also, using higher beam energy to look at Ce3d and Gd3d spectra can obtain better quantitative information on the surface reduction state.

EIS results on H_2/H_2O reaction at 600 °C suggest large impedance associated with low frequency, especially at lower temperature, high P_{O2} and H_2 oxidation conditions. However, analysis of impedance spectra in current study is only limited to pull out R_{bulk} from the intercept of high frequency. Future study may use equivalent circuit model fitting to the impedance data to study kinetics of the thin-film GDC electrode.

Other improvements to these experiments involve refining fabrication of the electrochemical cell. For example, XPS measurements indicate significant Si, likely coming from heating filament of MIT furnace or RF sputtering chamber, preventing the XPS measurement from obtaining high-resolution Ce4d spectra. Another improvement to these experiments is the Pt CE because Pt/YSZ interface in current study contributes a substantial overpotential portion of the total V_{cell}.

While 1-D kinetic model predictions agree with experimental results to some extent, additional validation on simulated kinetic and thermodynamic parameters is needed to improve model accuracy. For example, the model results show high non-

stoichiometry of ceria on the GDC surface and oxygen vacancy decreases significantly on anodic polarization. The discrepancies between surface reduction and bulk reduction of GDC are significantly affected by thermodynamics. The current study could be expanded by further comparing Ce^{3+} species concentration at related conditions.

Moreover, one assumption made in the current kinetic model is that the only contribution of CO-related species is to cover active reaction site besides constantly converting to H_2 and CO_2 through WGS reactions. The CO oxidation/CO_2 reduction is not well described in the model. Investigating CO/CO_2 reaction kinetics is needed in the future. The combination of the H_2 and CO mechanisms will represent an important milestone in developing hydrocarbons oxidation mechanisms in GDC anode of IT-SOFCs.

As for the 3-D stack model, it provides detailed information on the local state variable during its operation. Parametric studies on the geometry (flow channel width and height), flow arrangement (counter flow or cross flow), flux rate (excess cooling air), etc. will provide more information on optimizing stack performance and operation stability. The stack information can be further used for component design in the power system.

Glossary of Symbols Used

		Unit
A	Forward reaction rate coefficient parameter in Arrhenius form	(mol,cm,s)
a_k	Activity coefficients for species k	
a_k^0	Standard-state activity coefficient for species k	
a_m	Surface areas of the catalyst	m^2/m^3
B_g	Permeability	m^2
C_i	Concentration of charge species	mol/m^3
C_p	Specific heat	J/kg/K
Ce_{Ce}^X	Cerium on cerium lattice sites	
Ce_{Ce}'	One negative charge compared to normal cerium lattice	
D_i	Charge diffusion coefficient	m^2/s
D_{kj}	Binary diffusion coefficients	m^2/s
e^-	Electron	
E_{H2}	Exchange current density activation energy	eV
F	Faraday constant	C/mol
$\Delta\bar{G}^0$	Standard-state Gibbs free energy of reaction	kJ/mol
$\Delta\bar{G}_O$	Partial free energy of formation (per mol oxygen atom)	kJ/mol
$\bar{G}_{Ce_{Ce}'}$	Gibbs free energy of reduced ceria	kJ/mol
$\bar{G}_{Ce_{Ce}^X}$	Gibbs free energy of oxidized ceria	kJ/mol
$\bar{G}_{excess}$	Excess free energy	kJ/mol
$\bar{G}_{O_2@P^0}$	Standard Gibbs free energy of oxygen	kJ/mol
H_{surf}	Heat exchange coefficient	$W/m^2/K$
$H_{2(g),a}$	Hydrogen gas on anode	
$H_2O_{(g),a}$	Water in gas phase on anode	
i_0	Exchange current density	A/m^2
i_{ext}	External current density	A/m^2
i_{Far}	Faradaic current density	A/m^2
l_{TPB}	Length of three phase boundary	m/m^3
n_e	Charge number association with charge-transfer reaction	
$J_{k,g}$	Gas-phase mass flux	
k	Thermal conductivity	W/m/K
k_0	Exchange current density coefficient	A/m^2
k_b	Backward reaction rate coefficient	(mol,cm,s)
k_f	Forward reaction rate coefficient	(mol,cm,s)
$O_{2(g),c}$	Oxygen gas on cathode	
O_O^X	Oxygen atoms on oxygen lattice sites	
$O_{YSZ,a}^{2-}$	Oxide ion in YSZ electrolyte on anode side	
$O_{YSZ,c}^{2-}$	Oxide ion in YSZ electrolyte on anode side	

p	Pressure	Pa
P_{H2}	Partial pressure of hydrogen	Torr
P_{H2O}	Partial pressure of water	Torr
P_{tot}	Total pressure in the XPS chamber	Torr
P^0	Standard state pressure	bar
P_{O2}	Effective partial pressure of oxygen	bar
Q	Heat source	W/m^3
q_i	Rate-of-progress of reaction i	(mol,cm,s)
$\bar{R}$	Gas constant	kJ/kmol/K
R_{bulk}	Bulk resistance	ohm
$\dot{s}_{k,g,m}$	Gas-phase molar production rates per unit area	$mol/m^2/s$
T	Temperature	K
T_{cell}	Stack operating temperature	°C
T_{in}	Inlet temperature	°C
T_{ext}	Front and back surface temperature	°C
u	Velocity	m/s
u_k	Mobility of charge species	$m^2/V/s$
V_{cell}	Cell voltage	V
V_{OCV}	Open circuit voltage	V
V_{rev}	Theoretical open circuit voltage	V
$V_{\ddot{O}}$	Oxygen vacancies	
$[V_{\ddot{O}}]$	Oxygen vacancies concentration	$kmol/m^3$
X_k	Malar fraction of gaseous species	
$[X_k]$	Activity of species in the reaction	
Y_k	Mass fraction of gaseous species	
z_k	Charge number	
α_{fwd}	Symmetric parameter of forward reaction	
α_{bwd}	Symmetric parameter of reverse reaction	
α	Symmetric parameter	
$\theta_{k,\mathrm{surf}}$	Surface species molar fractions	
$\theta_{k,\mathrm{bulk}}$	Bulk species molar fractions	
η	Overpotential associated with charge-transfer reaction	V
φ	Phase-shift angle	
σ^0_{elec}	Fitting parameter of electronic conductivity	S/m
$\sigma_{elec,a}$	Electronic conductivity on anode side of electrolyte	S/m
$\sigma_{elec,c}$	Electronic conductivity on cathode side of electrolyte	S/m
σ_{ion}	Ionic conductivity of electrolyte membrane	S/m
ρ	Gas density	kg/m^3
v	Net stoichiometric coefficient of the reaction	
v_b	Stoichiometric coefficient in backward reaction	
v_f	Stoichiometric coefficient in forward reaction	

ω	Frequency	Hz
μ	Viscosity of gaseous species	Pa-s
K	Permeability of electrode	m^2
ϕ_g	Porosity of electrode	
τ_g	Tortuosity of electrode	
Φ_m	Electrical potential of phase m	V
$\Gamma_{bulk,m}$	Bulk density of solid phase (m)	$kmol/m^3$
$\Gamma_{surf,m}$	Surface density of solid phase (m)	$kmol/m^3$
γ_0	Sticking coefficient	

Bibliography

[1] Singhal, S. C., 2000, "Advances in solid oxide fuel cell technology," Solid State Ionics, 135(1-4), pp. 305-313.
[2] Steele, B. C. H., and Heinzel, A., 2001, "Materials for fuel-cell technologies," Nature, 414(6861), pp. 345-352.
[3] Ormerod, R. M., 2003, "Solid oxide fuel cells," Chemical Society Reviews, 32(1), pp. 17-28.
[4] Acres, G. J. K., 2001, "Recent advances in fuel cell technology and its applications," Journal of Power Sources, 100(1-2), pp. 60-66.
[5] de Bruijn, F., 2005, "The current status of fuel cell technology for mobile and stationary applications," Green Chemistry, 7(3), pp. 132-150.
[6] Wachsman, E. D., Marlowe, C. A., and Lee, K. T., 2012, "Role of solid oxide fuel cells in a balanced energy strategy," Energy & Environmental Science, 5(2), pp. 5498-5509.
[7] Kee, R. J., Zhu, H. Y., Sukeshini, A. M., and Jackson, G. S., 2008, "Solid oxide fuel cells: Operating principles, current challenges, and the role of syngas," Combustion Science and Technology, 180(6), pp. 1207-1244.
[8] Jiang, Y., and Virkar, A. V., 2003, "Fuel composition and diluent effect on gas transport and performance of anode-supported SOFCs," Journal of the Electrochemical Society, 150(7), pp. A942-A951.
[9] Zhu, H. Y., Kee, R. J., Janardhanan, V. M., Deutschmann, O., and Goodwin, D. G., 2005, "Modeling elementary heterogeneous chemistry and electrochemistry in solid-oxide fuel cells," Journal of the Electrochemical Society, 152(12), pp. A2427-A2440.
[10] Singhal, S. C., and Kendall, K., 2003, High Temperature Solid Oxide Fuel Cell: Fundamentals, Design and Applications, Elsevier, Oxford, UK.
[11] Zhu, W. Z., and Deevi, S. C., 2003, "A review on the status of anode materials for solid oxide fuel cells," Materials Science and Engineering a-Structural Materials Properties Microstructure and Processing, 362(1-2), pp. 228-239.
[12] Atkinson, A., Barnett, S., Gorte, R. J., Irvine, J. T. S., McEvoy, A. J., Mogensen, M., Singhal, S. C., and Vohs, J., 2004, "Advanced anodes for high-temperature fuel cells," Nature Materials, 3(1), pp. 17-27.
[13] Fleig, J., 2003, "Solid oxide fuel cell cathodes: Polarization mechanisms and modeling of the electrochemical performance," Annual Review of Materials Research, 33, pp. 361-382.
[14] Jiang, S. P., 2008, "Development of lanthanum strontium manganite perovskite cathode materials of solid oxide fuel cells: a review," Journal of Materials Science, 43(21), pp. 6799-6833.
[15] Wachsman, E. D., and Lee, K. T., 2011, "Lowering the Temperature of Solid Oxide Fuel Cells," Science, 334(6058), pp. 935-939.
[16] Sun, C. W., and Stimming, U., 2007, "Recent anode advances in solid oxide fuel cells," Journal of Power Sources, 171(2), pp. 247-260.

[17] Matsuzaki, Y., and Yasuda, I., 2001, "Dependence of SOFC cathode degradation by chromium-containing alloy on compositions of electrodes and electrolytes," Journal of the Electrochemical Society, 148(2), pp. A126-A131.
[18] Beckel, D., Bieberle-Hutter, A., Harvey, A., Infortuna, A., Muecke, U. P., Prestat, M., Rupp, J. L. M., and Gauckler, L. J., 2007, "Thin films for micro solid oxide fuel cells," Journal of Power Sources, 173(1), pp. 325-345.
[19] Rose, L., Menon, M., Kammer, K., Kesler, O., and Larsen, P. H., 2007, "Processing of Ce(1-x)Gd(x)O(2-delta) (GDC) thin films from precursors for application in solid oxide fuel cells," Thermec 2006 Supplement: 5th International Conference on Processing and Manufacturing of Advanced Materials, 15-17, pp. 293-298.
[20] Brett, D. J. L., Atkinson, A., Brandon, N. P., and Skinner, S. J., 2008, "Intermediate temperature solid oxide fuel cells," Chemical Society Reviews, 37(8), pp. 1568-1578.
[21] Dalslet, B., Blennow, P., Hendriksen, P. V., Bonanos, N., Lybye, D., and Mogensen, M., 2006, "Assessment of doped ceria as electrolyte," Journal of Solid State Electrochemistry, 10(8), pp. 547-561.
[22] Steele, B. C. H., 2000, "Appraisal of Ce1-yGdyO2-y/2 electrolytes for IT-SOFC operation at 500 degrees C," Solid State Ionics, 129(1-4), pp. 95-110.
[23] Fergus, J. W., 2006, "Electrolytes for solid oxide fuel cells," Journal of Power Sources, 162(1), pp. 30-40.
[24] Hui, S. Q., Roller, J., Yick, S., Zhang, X., Deces-Petit, C., Xie, Y. S., Maric, R., and Ghosh, D., 2007, "A brief review of the ionic conductivity enhancement for selected oxide electrolytes," Journal of Power Sources, 172(2), pp. 493-502.
[25] Murray, E. P., Tsai, T., and Barnett, S. A., 1999, "A direct-methane fuel cell with a ceria-based anode," Nature, 400(6745), pp. 649-651.
[26] Kharton, V. V., Marques, F. M. B., and Atkinson, A., 2004, "Transport properties of solid oxide electrolyte ceramics: a brief review," Solid State Ionics, 174(1-4), pp. 135-149.
[27] Omar, S., Wachsman, E. D., and Nino, J. C., 2007, "Higher ionic conductive ceria-based electrolytes for solid oxide fuel cells," Applied Physics Letters, 91(14), p. 3.
[28] Lim, H. T., and Virkar, A. V., 2009, "Measurement of oxygen chemical potential in Gd2O3-doped ceria-Y2O3-stabilized zirconia bi-layer electrolyte, anode-supported solid oxide fuel cells," Journal of Power Sources, 192(2), pp. 267-278.
[29] Shen, S. L., Guo, L. J., and Liu, H. T., 2013, "An analytical model for solid oxide fuel cells with bi-layer electrolyte," International Journal of Hydrogen Energy, 38(4), pp. 1967-1975.
[30] Ahn, J. S., Pergolesi, D., Camaratta, M. A., Yoon, H., Lee, B. W., Lee, K. T., Jung, D. W., Traversa, E., and Wachsman, E. D., 2009, "High-performance bilayered electrolyte intermediate temperature solid oxide fuel cells," Electrochemistry Communications, 11(7), pp. 1504-1507.
[31] Ahn, J. S., Camaratta, M. A., Pergolesi, D., Lee, K. T., Yoon, H., Lee, B. W., Jung, D. W., Traversa, E., and Wachsman, E. D., 2010, "Development of High Performance Ceria/Bismuth Oxide Bilayered Electrolyte SOFCs for Lower

Temperature Operation," Journal of the Electrochemical Society, 157(3), pp. B376-B382.
[32] Goodenough, J. B., and Huang, Y. H., 2007, "Alternative anode materials for solid oxide fuel cells," Journal of Power Sources, 173(1), pp. 1-10.
[33] Kharton, V. V., Figueiredo, F. M., Navarro, L., Naumovich, E. N., Kovalevsky, A. V., Yaremchenko, A. A., Viskup, A. P., Carneiro, A., Marques, F. M. B., and Frade, J. R., 2001, "Ceria-based materials for solid oxide fuel cells," Journal of Materials Science, 36(5), pp. 1105-1117.
[34] Werhahn, M. G., Schneider, O., and Stimming, U., 2013, "Thin Film Gadolinia Doped Ceria (GDC) Anode For Direct Conversion Of Carbon Black Particles In A Single Planar SOFC," Solid State Ionic Devices 9 - Ion Conducting Thin Films and Multilayers, 50(27), pp. 73-87.
[35] Gorte, R. J., and Vohs, J. M., 2003, "Novel SOFC anodes for the direct electrochemical oxidation of hydrocarbons," Journal of Catalysis, 216(1-2), pp. 477-486.
[36] Jung, S. W., Lu, C., He, H. P., Ahn, K. Y., Gorte, R. J., and Vohs, J. M., 2006, "Influence of composition and Cu impregnation method on the performance of Cu/CeO2/YSZ SOFC anodes," Journal of Power Sources, 154(1), pp. 42-50.
[37] Endler-Schuck, C., Leonide, A., Weber, A., Uhlenbruck, S., Tietz, F., and Ivers-Tiffee, E., 2011, "Performance analysis of mixed ionic-electronic conducting cathodes in anode supported cells," Journal of Power Sources, 196(17), pp. 7257-7262.
[38] Choi, M. B., Singh, B., Wachsman, E. D., and Song, S. J., 2013, "Performance of La0.1Sr0.9Co0.8Fe0.2O3-delta and La0.1Sr0.9Co0.8Fe0.2O3-delta-Ce0.9Gd0.1O2 oxygen electrodes with Ce0.9Gd0.1O2 barrier layer in reversible solid oxide fuel cells," Journal of Power Sources, 239, pp. 361-373.
[39] Wang, W. G., and Mogensen, M., 2005, "High-performance lanthanum-ferrite-based cathode for SOFC," Solid State Ionics, 176(5-6), pp. 457-462.
[40] Park, H. J., and Park, J. Y., 2013, "A promising high-performance lanthanum ferrite-based composite cathode for intermediate temperature solid oxide fuel cells," Solid State Ionics, 244, pp. 30-34.
[41] Kim, J. H., Park, Y. M., Kim, T., and Kim, H., 2012, "Characterizations of composite cathodes with La0.6Sr0.4Co0.2Fe0.8O3-delta and Ce0.9Gd0.1O1.95 for solid oxide fuel cells," Korean Journal of Chemical Engineering, 29(3), pp. 349-355.
[42] Leng, Y. J., Chan, S. H., and Liu, Q. L., 2008, "Development of LSCF-GDC composite cathodes for low-temperature solid oxide fuel cells with thin film GDC electrolyte," International Journal of Hydrogen Energy, 33(14), pp. 3808-3817.
[43] Liu, Z., Liu, M. F., Yang, L., and Liu, M. L., 2013, "LSM-infiltrated LSCF cathodes for solid oxide fuel cells," Journal of Energy Chemistry, 22(4), pp. 555-559.
[44] Trovarelli, A., 2002, Catalysis by Ceria and Related Materials, Imperial College Press.
[45] Fleig, J., 2002, "On the width of the electrochemically active region in mixed conducting solid oxide fuel cell cathodes," Journal of Power Sources, 105(2), pp. 228-238.
[46] Steele, B. C. H., 1995, "INTERFACIAL REACTIONS ASSOCIATED WITH CERAMIC ION-TRANSPORT MEMBRANES," Solid State Ionics, 75, pp. 157-165.

[47] Joo, J. H., and Choi, G. M., 2007, "Electrical conductivity of thin film ceria grown by pulsed laser deposition," Journal of the European Ceramic Society, 27(13-15), pp. 4273-4277.
[48] Jiang, S. P., Zhang, S., Zhen, Y. D., and Koh, A. P., 2004, "Performance of GDC-impregnated Ni anodes of SOFCs," Electrochemical and Solid State Letters, 7(9), pp. A282-A285.
[49] Chen, F., and Xiao, G., 2014, "Redox stable anodes for solid oxide fuel cells," Front. Energy Res., 00018.
[50] Zha, S. W., Moore, A., Abernathy, H., and Liu, M. L., 2004, "GDC-based low-temperature SOFCs powered by hydrocarbon fuels," Journal of the Electrochemical Society, 151(8), pp. A1128-A1133.
[51] Lee, K. T., Gore, C. M., and Wachsman, E. D., 2012, "Feasibility of low temperature solid oxide fuel cells operating on reformed hydrocarbon fuels," Journal of Materials Chemistry, 22(42), pp. 22405-22408.
[52] Wang, S. R., Inaba, H., Tagawa, H., Dokiya, M., and Hashimoto, T., 1998, "Nonstoichiometry of Ce0.9Gd0.1O1.95-x," Solid State Ionics, 107(1-2), pp. 73-79.
[53] Wang, S. R., Kobayashi, T., Dokiya, M., and Hashimoto, T., 2000, "Electrical and ionic conductivity of Gd-doped ceria," Journal of the Electrochemical Society, 147(10), pp. 3606-3609.
[54] Bishop, S. R., Duncan, K. L., and Wachsman, E. D., 2009, "Defect equilibria and chemical expansion in non-stoichiometric undoped and gadolinium-doped cerium oxide," Electrochimica Acta, 54(5), pp. 1436-1443.
[55] Bishop, S. R., Duncan, K. L., and Wachsman, E. D., 2009, "Surface and bulk oxygen non-stoichiometry and bulk chemical expansion in gadolinium-doped cerium oxide," Acta Materialia, 57(12), pp. 3596-3605.
[56] Virkar, A. V., and Wright, J., 2012, "Transport Properties of Mixed Ionic Electronic Conductors under Thermodynamically Equilibrated Conditions: Measurements on Porous Bodies," Ionic and Mixed Conducting Ceramics 8, 45(1), pp. 33-44.
[57] Green, R. D., Liu, C. C., and Adler, S. B., 2008, "Carbon dioxide reduction on gadolinia-doped ceria cathodes," Solid State Ionics, 179(17-18), pp. 647-660.
[58] Huang, T. J., and Yu, T. C., 2005, "Effect of steam and carbon dioxide pretreatments on methane decomposition and carbon gasification over doped-ceria supported nickel catalyst," Catalysis Letters, 102(3-4), pp. 175-181.
[59] Costa-Nunes, O., Vohs, J. M., and Gorte, R. J., 2003, "A study of direct-conversion SOFC with n-butane at higher fuel utilization," Journal of the Electrochemical Society, 150(7), pp. A858-A863.
[60] DeCaluwe, S. C., Grass, M. E., Zhang, C. J., El Gabaly, F., Bluhm, H., Liu, Z., Jackson, G. S., McDaniel, A. H., McCarty, K. F., Farrow, R. L., Linne, M. A., Hussain, Z., and Eichhorn, B. W., 2010, "In Situ Characterization of Ceria Oxidation States in High-Temperature Electrochemical Cells with Ambient Pressure XPS," Journal of Physical Chemistry C, 114(46), pp. 19853-19861.
[61] Zhang, C. J., Grass, M. E., McDaniel, A. H., DeCaluwe, S. C., El Gabaly, F., Liu, Z., McCarty, K. F., Farrow, R. L., Linne, M. A., Hussain, Z., Jackson, G. S., Bluhm, H., and Eichhorn, B. W., 2010, "Measuring fundamental properties in

operating solid oxide electrochemical cells by using in situ X-ray photoelectron spectroscopy," Nature Materials, 9(11), pp. 944-949.
[62] Chueh, W. C., McDaniel, A. H., Grass, M. E., Hao, Y., Jabeen, N., Liu, Z., Haile, S. M., McCarty, K. F., Bluhm, H., and El Gabaly, F., 2012, "Highly Enhanced Concentration and Stability of Reactive Ce3+ on Doped CeO2 Surface Revealed In Operando," Chemistry of Materials, 24(10), pp. 1876-1882.
[63] Zhang, C. J., Yu, Y., Grass, M. E., Dejoie, C., Ding, W. C., Gaskell, K., Jabeen, N., Hong, Y. P., Shayorskiy, A., Bluhrn, H., Li, W. X., Jackson, G. S., Hussain, Z., Liu, Z., and Eichhorn, B. W., 2013, "Mechanistic Studies of Water Electrolysis and Hydrogen Electro-Oxidation on High Temperature Ceria-Based Solid Oxide Electrochemical Cells," Journal of the American Chemical Society, 135(31), pp. 11572-11579.
[64] Yu, Y., Mao, B., Geller, A., Chang, R., Gaskell, K., Liu, Z., and Eichhorn, B. W., 2014, "CO2 activation and carbonate intermediates: an operando AP-XPS study of CO2 electrolysis reactions on solid oxide electrochemical cells," Physical Chemistry Chemical Physics, 16(23), pp. 11633-11639.
[65] Mizusaki, J., Tagawa, H., Isobe, K., Tajika, M., Koshiro, I., Maruyama, H., and Hirano, K., 1994, "KINETICS OF THE ELECTRODE-REACTION AT THE H2-H2O POROUS PT STABILIZED ZIRCONIA INTERFACE," Journal of the Electrochemical Society, 141(6), pp. 1674-1683.
[66] Goodwin, D. G., Zhu, H. Y., Colclasure, A. M., and Kee, R. J., 2009, "Modeling Electrochemical Oxidation of Hydrogen on Ni-YSZ Pattern Anodes," Journal of the Electrochemical Society, 156(9), pp. B1004-B1021.
[67] Chueh, W. C., Hao, Y., Jung, W., and Haile, S. M., 2012, "High electrochemical activity of the oxide phase in model ceria-Pt and ceria-Ni composite anodes," Nature Materials, 11(2), pp. 155-161.
[68] Mogensen, M., Sammes, N. M., and Tompsett, G. A., 2000, "Physical, chemical and electrochemical properties of pure and doped ceria," Solid State Ionics, 129(1-4), pp. 63-94.
[69] Adler, S. B., Chen, X. Y., and Wilson, J. R., 2007, "Mechanisms and rate laws for oxygen exchange on mixed-conducting oxide surfaces," Journal of Catalysis, 245(1), pp. 91-109.
[70] Yakabe, H., and Sakurai, I., 2004, "3D simulation on the current path in planar SOFCs," Solid State Ionics, 174(1-4), pp. 295-302.
[71] Ackmann, T., de Haart, L. G. J., Lehnert, W., and Stolten, D., 2003, "Modeling of mass and heat transport in planar substrate type SOFCs," Journal of the Electrochemical Society, 150(6), pp. A783-A789.
[72] Campanari, S., and Iora, P., 2004, "Definition and sensitivity analysis of a finite volume SOFC model for a tubular cell geometry," Journal of Power Sources, 132(1-2), pp. 113-126.
[73] DeCaluwe, S. C., Zhu, H., Kee, R. J., and Jackson, G. S., 2008, "Importance of anode microstructure in modeling solid oxide fuel cells," Journal of the Electrochemical Society, 155(6), pp. B538-B546.
[74] Jeon, D. H., 2009, "A comprehensive CFD model of anode-supported solid oxide fuel cells," Electrochimica Acta, 54(10), pp. 2727-2736.

[75] Qu, Z. P., Aravind, P. V., Boksteen, S. Z., Dekker, N. J. J., Janssen, A. H. H., Woudstra, N., and Verkooijen, A. H. M., 2011, "Three-dimensional computational fluid dynamics modeling of anode-supported planar SOFC," International Journal of Hydrogen Energy, 36(16), pp. 10209-10220.
[76] Andersson, M., Paradis, H., Yuan, J. L., and Sunden, B., 2013, "Three dimensional modeling of an solid oxide fuel cell coupling charge transfer phenomena with transport processes and heat generation," Electrochimica Acta, 109, pp. 881-893.
[77] Serincan, M. F., Pasaogullari, U., and Sammes, N. M., 2009, "Effects of operating conditions on the performance of a micro-tubular solid oxide fuel cell (SOFC)," Journal of Power Sources, 192(2), pp. 414-422.
[78] Serincan, M. F., Pasaogullari, U., and Sammes, N. M., 2008, "Computational thermal-fluid analysis of a microtubular solid oxide fuel cell," Journal of the Electrochemical Society, 155(11), pp. B1117-B1127.
[79] Fleig, J., Baumann, F. S., Brichzin, V., Kim, H. R., Jamnik, J., Cristiani, G., Habermeier, H. U., and Maier, J., 2006, "Thin film microelectrodes in SOFC electrode research," Fuel Cells, 6(3-4), pp. 284-292.
[80] Nakamura, T., Yashiro, K., Kaimai, A., Otake, T., Sato, K., Kawada, T., and Mizusaki, J., 2008, "Determination of the Reaction Zone in Gadolinia-Doped Ceria Anode for Solid Oxide Fuel Cell," Journal of the Electrochemical Society, 155(12), pp. B1244-B1250.
[81] Zha, S. W., Rauch, W., and Liu, M. L., 2004, "Ni-Ce0.9Gd0.1O1.95 anode for GDC electrolyte-based low-temperature SOFCs," Solid State Ionics, 166(3-4), pp. 241-250.
[82] Aravind, P. V., Ouweltjes, J. P., and Schoonman, J., 2009, "Diffusion Impedance on Nickel/Gadolinia-Doped Ceria Anodes for Solid Oxide Fuel Cells," Journal of the Electrochemical Society, 156(12), pp. B1417-B1422.
[83] Baumann, F. S., Fleig, J., Habermeier, H. U., and Maier, J., 2006, "Ba0.5Sr0.5Co0.8Fe0.2O3-delta thin film microelectrodes investigated by impedance spectroscopy," Solid State Ionics, 177(35-36), pp. 3187-3191.
[84] Ia O, G. J., and Shao-Horn, Y., 2009, "Oxygen Surface Exchange Kinetics on Sr-Substituted Lanthanum Manganite and Ferrite Thin-Film Microelectrodes," Journal of the Electrochemical Society, 156(7), pp. B816-B824.
[85] Baumann, F. S., Maier, J., and Fleig, J., 2008, "The polarization resistance of mixed conducting SOFC cathodes: A comparative study using thin film model electrodes," Solid State Ionics, 179(21-26), pp. 1198-1204.
[86] Huang, H., Gur, T. M., Saito, Y., and Prinz, F., 2006, "High ionic conductivity in ultrathin nanocrystalline gadolinia-doped ceria films," Applied Physics Letters, 89(14), p. 3.
[87] Mebane, D. S., Liu, Y. J., and Liu, M. L., 2007, "A two-dimensional model and numerical treatment for mixed conducting thin films," Journal of the Electrochemical Society, 154(5), pp. A421-A426.
[88] Brosha, E. L., Mukundan, R., Brown, D. R., Jia, Q. X., Lujan, R., and Garzon, F. H., 2004, "Techniques for the thin film growth of La1-xSrxCrO3 for solid state ionic devices," Solid State Ionics, 166(3-4), pp. 425-440.

[89] Kuo, Y. L., Lee, C., Chen, Y. S., and Liang, H., 2009, "Gadolinia-doped ceria films deposited by RF reactive magnetron sputtering," Solid State Ionics, 180(26-27), pp. 1421-1428.
[90] Lin, S. E., Kuo, Y. L., Chou, C. H., and Wei, W. C. J., 2010, "Characterization of electrolyte films deposited by using RF magnetron sputtering a 20 mol% gadolinia-doped ceria target," Thin Solid Films, 518(24), pp. 7229-7232.
[91] Goodwin, D. G., (2001-2012), "Cantera,"http://code.google.com/p/cantera/.
[92] Matsui, T., Minoru, I., Mineshige, A., and Ogumi, Z., 2005, "Electrochemical properties of ceria-based oxides for use in intermediate-temperature SOFCs," Solid State Ionics, 176(7-8), pp. 647-654.
[93] Kek, D., Mogensen, M., and Pejovnik, S., 2001, "A study of metal (Ni, Pt, Au)/yttria-stabilized zirconia interface in hydrogen atmosphere at elevated temperature," Journal of the Electrochemical Society, 148(8), pp. A878-A886.
[94] El Gabaly, F., Grass, M., McDaniel, A. H., Farrow, R. L., Linne, M. A., Hussain, Z., Bluhm, H., Liu, Z., and McCarty, K. F., 2010, "Measuring individual overpotentials in an operating solid-oxide electrochemical cell," Physical Chemistry Chemical Physics, 12(38), pp. 12138-12145.
[95] Kim-Lohsoontorn, P., and Bae, J., 2011, "Electrochemical performance of solid oxide electrolysis cell electrodes under high-temperature coelectrolysis of steam and carbon dioxide," Journal of Power Sources, 196(17), pp. 7161-7168.
[96] Zhang, C. J., Grass, M. E., Yu, Y., Gaskell, K. J., DeCaluwe, S. C., Chang, R., Jackson, G. S., Hussain, Z., Bluhm, H., Eichhorn, B. W., and Liu, Z., 2012, "Multielement Activity Mapping and Potential Mapping in Solid Oxide Electrochemical Cells through the use of operando XPS," Acs Catalysis, 2(11), pp. 2297-2304.
[97] Keiser, J. T., Hoffbauer, M. A., and Lin, M. C., 1985, "PRODUCTION OF OH ON POLYCRYSTALLINE NICKEL STUDIED BY THERMAL-DESORPTION LASER-INDUCED FLUORESCENCE," Journal of Physical Chemistry, 89(12), pp. 2635-2638.
[98] Mohsenzadeh, A., Bolton, K., and Richards, T., 2014, "DFT study of the adsorption and dissociation of water on Ni(111), Ni(110) and Ni(100) surfaces," Surface Science, 627, pp. 1-10.
[99] Shin, H. H., and McIntosh, S., 2013, "Insights into Hydrogen Oxidation on SOFC Anode Materials by Isotopic Exchange," Ecs Electrochemistry Letters, 2(11), pp. F88-F91.
[100] Matsuzaki, Y., and Yasuda, I., 2000, "Electrochemical oxidation of H-2 and CO in a H-2-H2O-CO-CO2 system at the interface of a Ni-YSZ cermet electrode and YSZ electrolyte," Journal of the Electrochemical Society, 147(5), pp. 1630-1635.
[101] Freund, H. J., and Roberts, M. W., 1996, "Surface chemistry of carbon dioxide," Surface Science Reports, 25(8), pp. 225-273.
[102] Liu, C., Cundari, T. R., and Wilson, A. K., 2012, "CO2 Reduction on Transition Metal (Fe, Co, Ni, and Cu) Surfaces: In Comparison with Homogeneous Catalysis," Journal of Physical Chemistry C, 116(9), pp. 5681-5688.
[103] Janardhanan, V. M., and Deutschmann, O., 2006, "CFD analysis of a solid oxide fuel cell with internal reforming: Coupled interactions of transport,

heterogeneous catalysis and electrochemical processes," Journal of Power Sources, 162(2), pp. 1192-1202.
[104] Staudt, T., Lykhach, Y., Tsud, N., Skala, T., Prince, K. C., Matolin, V., and Libuda, J., 2011, "Electronic Structure of Magnesia-Ceria Model Catalysts, CO2 Adsorption, and CO2 Activation: A Synchrotron Radiation Photoelectron Spectroscopy Study," Journal of Physical Chemistry C, 115(17), pp. 8716-8724.
[105] Wagner, C. D., Riggs, W. M., Davis, L. E., and Moulder, J. F., 1979, Handbook of X-ray Photoelectron Spectroscopy, Perkin-Elmer Corporation Physical Electronics Division.
[106] Crumlin, E. J., Mutoro, E., Hong, W. T., Biegalski, M. D., Christen, H. M., Liu, Z., Bluhm, H., and Shao-Horn, Y., 2013, "In Situ Ambient Pressure X-ray Photoelectron Spectroscopy of Cobalt Perovskite Surfaces under Cathodic Polarization at High Temperatures," Journal of Physical Chemistry C, 117(31), pp. 16087-16094.
[107] Grass, M. E., Karlsson, P. G., Zhang, C. J., El Gabaly, F., McDaniel, A. H., DeCaluwe, S. H., Aksoy, F., Mun, B. S., Jackson, G. S., Hussain, Z., Bluhm, H., McCarty, K. F., Eichorn, B., and Liu, Z., 2010, "Ambient pressure XPS for spatial and angular resolution of operational heterogeneous catalysts and electrochemical systems," Abstracts of Papers of the American Chemical Society, 240, p. 1.
[108] Crumlin, E. J., Bluhm, H., and Liu, Z., 2013, "In situ investigation of electrochemical devices using ambient pressure photoelectron spectroscopy," Journal of Electron Spectroscopy and Related Phenomena, 190, pp. 84-92.
[109] Salmeron, M., and Schlogl, R., 2008, "Ambient pressure photoelectron spectroscopy: A new tool for surface science and nanotechnology," Surface Science Reports, 63(4), pp. 169-199.
[110] Ladas, S., Kennou, S., Bebelis, S., and Vayenas, C. G., 1993, "ORIGIN OF NON-FARADAIC ELECTROCHEMICAL MODIFICATION OF CATALYTIC ACTIVITY," Journal of Physical Chemistry, 97(35), pp. 8845-8848.
[111] Doron-Mor, H., Hatzor, A., Vaskevich, A., van der Boom-Moav, T., Shanzer, A., Rubinstein, I., and Cohen, H., 2000, "Controlled surface charging as a depth-profiling probe for mesoscopic layers," Nature, 406(6794), pp. 382-385.
[112] Bard, A. J., and L.R.Faulkner, 2001, "Electrochemical Methods, Fundamentals and Applications ", John Wiley.
[113] Whaley, J. A., McDaniel, A. H., El Gabaly, F., Farrow, R. L., Grass, M. E., Hussain, Z., Liu, Z., Linne, M. A., Bluhm, H., and McCarty, K. F., 2010, "Note: Fixture for characterizing electrochemical devices in-operando in traditional vacuum systems," Review of Scientific Instruments, 81(8), p. 3.
[114] Watkins, M. B., Foster, A. S., and Shluger, A. L., 2007, "Hydrogen cycle on CeO(2) (111) surfaces: Density functional theory calculations," Journal of Physical Chemistry C, 111(42), pp. 15337-15341.
[115] Bluhm, H., 2010, "Photoelectron spectroscopy of surfaces under humid conditions," Journal of Electron Spectroscopy and Related Phenomena, 177(2-3), pp. 71-84.
[116] Mullins, D. R., Overbury, S. H., and Huntley, D. R., 1998, "Electron spectroscopy of single crystal and polycrystalline cerium oxide surfaces," Surface Science, 409(2), pp. 307-319.

[117] Kundakovic, L., Mullins, D. R., and Overbury, S. H., 2000, "Adsorption and reaction of H2O and CO on oxidized and reduced Rh/CeOx(111) surfaces," Surface Science, 457(1-2), pp. 51-62.
[118] Yamamoto, S., Andersson, K., Bluhm, H., Ketteler, G., Starr, D. E., Schiros, T., Ogasawara, H., Pettersson, L. G. M., Salmeron, M., and Nilsson, A., 2007, "Hydroxyl-induced wetting of metals by water at near-ambient conditions," Journal of Physical Chemistry C, 111(22), pp. 7848-7850.
[119] Li, J. T., Swiatowska, J., Seyeux, A., Huang, L., Maurice, V., Sun, S. G., and Marcus, P., 2010, "XPS and ToF-SIMS study of Sn-Co alloy thin films as anode for lithium ion battery," Journal of Power Sources, 195(24), pp. 8251-8257.
[120] Nilsson, A., 2002, "Applications of core level spectroscopy to adsorbates," Journal of Electron Spectroscopy and Related Phenomena, 126(1-3), pp. 3-42.
[121] Mudiyanselage, K., Senanayake, S. D., Feria, L., Kundu, S., Baber, A. E., Graciani, J., Vidal, A. B., Agnoli, S., Evans, J., Chang, R., Axnanda, S., Liu, Z., Sanz, J. F., Liu, P., Rodriguez, J. A., and Stacchiola, D. J., 2013, "Importance of the Metal-Oxide Interface in Catalysis: In Situ Studies of the Water-Gas Shift Reaction by Ambient-Pressure X-ray Photoelectron Spectroscopy," Angewandte Chemie-International Edition, 52(19), pp. 5101-5105.
[122] Nolan, M., and Watson, G. W., 2006, "The surface dependence of CO adsorption on ceria," Journal of Physical Chemistry B, 110(33), pp. 16600-16606.
[123] Xu, F., Mudiyanselage, K., Baber, A. E., Soldemo, M., Weissenrieder, J., White, M. G., and Stacchiola, D. J., 2014, "Redox-Mediated Reconstruction of Copper during Carbon Monoxide Oxidation," Journal of Physical Chemistry C, 118(29), pp. 15902-15909.
[124] Nolan, M., 2009, "Molecular Adsorption on the Doped (110) Ceria Surface," Journal of Physical Chemistry C, 113(6), pp. 2425-2432.
[125] Deseure, J., Bultel, Y., Dessemond, L., and Siebert, E., 2005, "Modelling of do and ac responses of a planar mixed conducting oxygen electrode," Solid State Ionics, 176(3-4), pp. 235-244.
[126] Fleig, J., and Maier, J., 2004, "The polarization of mixed conducting SOFC cathodes: Effects of surface reaction coefficient, ionic conductivity and geometry," Journal of the European Ceramic Society, 24(6), pp. 1343-1347.
[127] Ruger, B., Weber, A., and Ivers-Tiffee, E., 2007, "3D-Modelling and Performance Evaluation of Mixed Conducting (MIEC) Cathodes," Solid Oxide Fuel Cells 10 (Sofc-X), Pts 1 and 2, 7(1), pp. 2065-2074.
[128] Adler, S. B., Lane, J. A., and Steele, B. C. H., 1996, "Electrode kinetics of porous mixed-conducting oxygen electrodes," Journal of the Electrochemical Society, 143(11), pp. 3554-3564.
[129] Riess, I., 1981, "THEORETICAL TREATMENT OF THE TRANSPORT-EQUATIONS FOR ELECTRONS AND IONS IN A MIXED CONDUCTOR," Journal of the Electrochemical Society, 128(10), pp. 2077-2081.
[130] Riess, I., 1992, "POTENTIAL MEASUREMENTS USING MIXED IONIC ELECTRONIC CONDUCTORS AS PROBES," Journal of the Electrochemical Society, 139(8), pp. 2250-2252.
[131] Riess, I., 2003, "Mixed ionic-electronic conductors - material properties and applications," Solid State Ionics, 157(1-4), pp. 1-17.

[132] Chan, S. H., Chen, X. J., and Khor, K. A., 2002, "An electrolyte model for ceramic oxygen generator and solid oxide fuel cell," Journal of Power Sources, 111(2), pp. 320-328.
[133] Duncan, K. L., Wang, Y. L., Bishop, S. R., Ebrahimi, F., and Wachsman, E. D., 2006, "Role of point defects in the physical properties of fluorite oxides," Journal of the American Ceramic Society, 89(10), pp. 3162-3166.
[134] Duncan, K. L., and Wachsman, E. D., 2009, "Continuum-Level Analytical Model for Solid Oxide Fuel Cells with Mixed Conducting Electrolytes," Journal of the Electrochemical Society, 156(9), pp. B1030-B1038.
[135] Duncan, K. L., Lee, K. T., and Wachsman, E. D., 2011, "Dependence of open-circuit potential and power density on electrolyte thickness in solid oxide fuel cells with mixed conducting electrolytes," Journal of Power Sources, 196(5), pp. 2445-2451.
[136] Bessler, W. G., Warnatz, J., and Goodwin, D. G., 2007, "The influence of equilibrium potential on the hydrogen oxidation kinetics of SOFC anodes," Solid State Ionics, 177(39-40), pp. 3371-3383.
[137] Yun, J. W., Han, J., Yoon, S. P., Park, S., Kim, H. S., and Nam, S. W., 2011, "Ce0.8Gd0.2O2 modification on La0.6Sr0.4Co0.2Fe0.8O3 cathode for improving a cell performance in intermediate temperature solid oxide fuel cells," Journal of Industrial and Engineering Chemistry, 17(3), pp. 439-444.
[138] Esch, F., Fabris, S., Zhou, L., Montini, T., Africh, C., Fornasiero, P., Comelli, G., and Rosei, R., 2005, "Electron localization determines defect formation on ceria substrates," Science, 309(5735), pp. 752-755.
[139] Nolan, M., Fearon, J. E., and Watson, G. W., 2006, "Oxygen vacancy formation and migration in ceria," Solid State Ionics, 177(35-36), pp. 3069-3074.
[140] Mhadeshwar, A. B., and Vlachos, D. G., 2004, "Microkinetic modeling for water-promoted CO oxidation, water-gas shift, and preferential oxidation of CO on pt," Journal of Physical Chemistry B, 108(39), pp. 15246-15258.
[141] Graves, C., Ebbesen, S. D., and Mogensen, M., 2009, "Aspects of Metal-YSZ Electrode Kinetics Studied Using Model Electrodes," Solid Oxide Fuel Cells 11 (Sofc-Xi), 25(2), pp. 1945-1955.
[142] Kazempoor, P., Dorer, V., and Ommi, F., 2009, "Evaluation of hydrogen and methane-fuelled solid oxide fuel cell systems for residential applications: System design alternative and parameter study," International Journal of Hydrogen Energy, 34(20), pp. 8630-8644.
[143] Janardhanan, V. M., Heuveline, V., and Deutschmann, O., 2007, "Performance analysis of a SOFC under direct internal reforming conditions," Journal of Power Sources, 172(1), pp. 296-307.
[144] Bessler, W. G., Gewies, S., Willich, C., Schiller, G., and Friedrich, K. A., 2010, "Spatial Distribution of Electrochemical Performance in a Segmented SOFC: A Combined Modeling and Experimental Study," Fuel Cells, 10(3), pp. 411-418.
[145] DiGiuseppe, G., Gowda, Y. J., and Honnagondanahalli, N. K., 2012, "A Two-Dimensional Modeling Study of a Planar SOFC Using Actual Cell Testing Geometry and Operating Conditions," Journal of Fuel Cell Science and Technology, 9(1), p. 12.

[146] Andersson, M., Paradis, H., Yuan, J., and Sunden, B., 2011, "Modeling Analysis of Different Renewable Fuels in an Anode Supported SOFC," Journal of Fuel Cell Science and Technology, 8(3).
[147] Akhtar, N., Decent, S. P., Loghin, D., and Kendall, K., 2009, "A three-dimensional numerical model of a single-chamber solid oxide fuel cell," International Journal of Hydrogen Energy, 34(20), pp. 8645-8663.
[148] Fuller E.N., S. P. D., and Giddings J.C, 1966, "A new methode for prediction of binary gas-phase diffusion coefficients."
[149] Zhu, H. Y., and Kee, R. J., 2003, "A general mathematical model for analyzing the performance of fuel-cell membrane-electrode assemblies," Journal of Power Sources, 117(1-2), pp. 61-74.
[150] Zeng, M., Yuan, J. L., Zhang, J., Sunden, B., and Wang, Q. W., 2012, "Investigation of thermal radiation effects on solid oxide fuel cell performance by a comprehensive model," Journal of Power Sources, 206, pp. 185-196.
[151] Gil, V., Larrea, A., Merino, R. I., and Orera, V. M., 2009, "Redox behaviour of Gd-doped ceria-nickel oxide composites," Journal Of Power Sources, 192(1), pp. 180-184.
[152] Lin, Y. B., Zhan, Z. L., Liu, J., and Barnett, S. A., 2005, "Direct operation of solid oxide fuel cells with methane fuel," Solid State Ionics, 176(23-24), pp. 1827-1835.
[153] Haberman, B. A., and Young, J. B., 2004, "Three-dimensional simulation of chemically reacting gas flows in the porous support structure of an integrated-planar solid oxide fuel cell," International Journal of Heat and Mass Transfer, 47(17-18), pp. 3617-3629.
[154] He, H. P., and Hill, J. M., 2007, "Carbon deposition on Ni/YSZ composites exposed to humidified methane," Applied Catalysis a-General, 317(2), pp. 284-292.
[155] Patel, S., Jawlik, P. F., Wang, L., Jackson, G. S., and Almansoori, A., 2012, "Impact of Cofiring Ceria in Ni/YSZ SOFC Anodes for Operation With Syngas and n-Butane," Journal of Fuel Cell Science and Technology, 9(4), p. 7.
[156] Xu, J. H., Yeung, C. M. Y., Ni, J., Meunier, F., Acerbi, N., Fowles, M., and Tsang, S. C., 2008, "Methane steam reforming for hydrogen production using low water-ratios without carbon formation over ceria coated Ni catalysts," Applied Catalysis a-General, 345(2), pp. 119-127.
[157] Godickemeier, M., and Gauckler, L. J., 1998, "Engineering of solid oxide fuel cells with ceria-based electrolytes," Journal of the Electrochemical Society, 145(2), pp. 414-421.
[158] Milliken, C., Guruswamy, S., and Khandkar, A., 1999, "Evaluation of ceria electrolytes in solid oxide fuel cells electric power generation," Journal of the Electrochemical Society, 146(3), pp. 872-882.
[159] Matsui, T., Kosaka, T., Inaba, M., Mineshige, A., and Ogumi, Z., 2005, "Effects of mixed conduction on the open-circuit voltage of intermediate-temperature SOFCs based on Sm-doped ceria electrolytes," Solid State Ionics, 176(7-8), pp. 663-668.
[160] Blackburn, B. M., Yoon, H. S., Gore, C. M., and Wachsman, E. D., 2014, "Testing of Large Format Lower Temperature SOFCs and Stacks with Hydrocarbon Fuels," ECS Abstract.

[161] Nakajo, A., Mueller, F., Brouwer, J., Van Herle, J., and Favrat, D., 2012, "Mechanical reliability and durability of SOFC stacks. Part I: Modelling of the effect of operating conditions and design alternatives on the reliability," International Journal of Hydrogen Energy, 37(11), pp. 9249-9268.